2021

Mri Assessment Of Maternal Uteroplacental Circulation In Pregnancy

Eileen Hwuang
University of Pennsylvania

Mri Assessment Of Maternal Uteroplacental Circulation In Pregnancy

Abstract

Hypertensive pregnancy disorders (HPD) such as preeclampsia are highly associated with maternal vascular malperfusion of the placenta, an organ that exchanges nutrients and oxygen between the maternal circulation and the growing fetus. Adverse pregnancy outcomes are difficult to predict because there is insufficient understanding of how poor maternal arterial remodeling leads to disease. There is also a lack of reliable tools to evaluate these changes in early gestation.

The hypothesis of this dissertation was that magnetic resonance imaging (MRI) could noninvasively evaluate uteroplacental function in vivo through a combination of arterial spin labeling (ASL), 4D flow, and time-of-flight (TOF) techniques which were already effective in the evalution of other cardiovascular diseases. These flow and perfusion imaging studies were conducted on human pregnant volunteers in their second and third trimesters at 1.5T. Many of them were also examined by conventional Doppler ultrasound (US) and followed through delivery.

Flow-sensitive Alternating Inversion Recovery (FAIR) ASL MRI with background suppression was found to be feasible in detecting placental perfusion signal despite the presence of motion artifacts. An important consideration when studying placental ASL was the slow movement of maternal arterial blood in a large cavity called the intervillous space. This was a unique feature of placental anatomy which distinguished it from other organs containing capillaries. It became apparent that traditional models to estimate perfusion from MRI were no longer applicable. In this work, a statistical approach was first developed to filter out motion artifacts, followed by a coordinate transformation to better represent the lobular distribution of blood flow in the intervillous space of the placenta. The uterine arteries (UtAs) are the main maternal blood supply of the placenta and have also long been suspected to be involved in HPD, though US-based measurements have not yet been found to be highly predictive for widespread clinical use. In this work, 4D flow MRI enabled visualization of the tortuous UtAs while measuring volumetric flow rate. Its performance in predicting incidence of preeclampsia and small-for-gestational age births was comparable to Doppler US. When considering the innovative potential of 4D flow MRI to capture complex flow dynamics, this validation demonstrated the value of continuing technical development for improving HPD risk assessment. Furthermore, centerline extraction of the maternal pelvic arteries in TOF MRI, from the descending aorta to the UtAs and external iliac arteries, provided quantitative metrics to characterize the geometry including path length and curvature. Pulse wave velocity (PWV) was estimated using path length by TOF MRI and velocimetry by 2D phase contrast and 4D flow MRI with results showing sensitivity to differences between UtAs and external iliac arteries. These approaches provided physiological metrics to explore and characterize the remodeling process of the uteroplacental arteries. This dissertation demonstrates the feasibility of measuring structure and hemodynamics of the maternal vascular blood supply using non-contrast MRI that can lead to the more reliable biomarkers of adverse pregnancy outcomes needed to diagnose and treat HPD.

Degree Type

Dissertation

Degree Name

Doctor of Philosophy (PhD)

Graduate Group

Bioengineering

MRI ASSESSMENT OF MATERNAL UTEROPLACENTAL CIRCULATION IN PREGNANCY

Eileen Hwuang

A DISSERTATION

in

Bioengineering

Presented to the Faculties of the University of Pennsylvania

in

Partial Fulfillment of the Requirements for the

Degree of Doctor of Philosophy

2021

Co-Supervisor of Dissertation

_____

Walter R. Witschey, Ph.D.

Associate Professor of Radiology

Co-Supervisor of Dissertation

_____

John A. Detre, M.D.

Professor of Neurology and Radiology

Graduate Group Chairperson

_____

Yale Cohen, Ph.D.

Professor of Bioengineering

Dissertation Committee

David Issadore, Ph.D., Associate Professor of Bioengineering

Nadav Schwartz, M.D., Associate Professor of Obstetrics and Gynecology

Paulo Arratia, Ph.D., Professor of Mechanical Engineering and Applied Mechanics and Chemical and Biomolecular Engineering

DEDICATION

To my parents Steve and Sharon, my brother Jerry, and all mothers and children who have suffered from pregnancy complications.

ACKNOWLEDGEMENTS

I am grateful for all the faculty, colleagues and classmates who have supported in my PhD training. My thesis advisors Drs. Walter Witschey and John Detre have been wonderful mentors guiding me through creative experimental design, data analysis, countless writing and presentation revisions, and instilling confidence when work feels overwhelming. I thank my thesis committee professors Nadav Schwartz, Paulo Arratia, and David Issadore for always being available to offer their valuable perspectives to this dissertation work.

I especially want to thank Nadav Schwartz for his dedicated leadership and the entire U01 **EX**amining **PL**acenta **O**xygenation pe**R**fusion and siz**E** (EXPLORE) placenta research team. Without them, this thesis would not exist. Postdoctoral researchers Marta Vidorretta, Ana Rodriguez-Soto, and Pei-Hsin Wu have been wonderful MRI scanning “partners” and helped me grow as a scientist in training. I am indebted to the research coordinators especially Julia Siegal, Alexandra Acker, and Keri Simonette for their patience and meticulous organization to arrange for hundreds of patient visits to the MRI and ultrasound suite. Nathanael Koelper has generously shared his statistical expertise and time to help with data analysis amidst his busy schedule. I thank the amazing MRI technicians especially Patricia O’Donnell, Doris Cain, and Jacqui Meeks who have not only helped keep patients comfortable and troubleshoot problems, but also have become friendly companions during long scans.

I would also like to thank Dylan Tisdall, my informal mentor, whose endless creativity has made MRI physics and mathematics a joyful, curious experience for me. I thank Michael Langham for many helpful discussions about flow MRI. Paris Perdikaris and his student George Kissas have been great collaborators in offering their expertise in computational fluid dynamics to help me study hypertensive pregnancy disorders in a new way.

I am blessed to be a part of the HHMI Interfaces Program and have the support of its leadership, who designed the innovative curriculum that gave me the foundation to pursue this dissertation research. I am grateful for my academic friends and colleagues especially past and present members of Walter Witschey's lab (Brianna Moon, Srikant Iyer, Tracy Jenkins), Shobhana Parameshwaran, Lauren Beck, Varsha Viswanath, Megan Sperry, and Preya Shah.

Finally, I would like to acknowledge the support of my parents Steve and Sharon Hwuang for being my anchor throughout the ups and downs of PhD training. My brothers and sisters at Tenth Presbyterian Church in Philadelphia, especially Sabita Balgobin, Sarah Park, Bruce and Janet Chambers, Rebecca Marcos, Gloria Shen, and my boyfriend Vinh Hoang for their fervent prayers, sweet fellowship, and encouragement to trust in God throughout the long journey. May this dissertation bring honor and glory to God.

ABSTRACT

MRI ASSESSMENT OF MATERNAL UTEROPLACENTAL CIRCULATION IN PREGNANCY

Eileen Hwuang

Walter R. Witschey

John A. Detre

Hypertensive pregnancy disorders (HPD) such as preeclampsia are highly associated with maternal vascular malperfusion of the placenta, an organ that exchanges nutrients and oxygen between the maternal circulation and the growing fetus. Adverse pregnancy outcomes are difficult to predict because there is insufficient understanding of how poor maternal arterial remodeling leads to disease. There is also a lack of reliable tools to evaluate these changes in early gestation.

The hypothesis of this dissertation was that magnetic resonance imaging (MRI) could noninvasively evaluate uteroplacental function in vivo through a combination of arterial spin labeling (ASL), 4D flow, and time-of-flight (TOF) techniques which were already effective in the evalution of other cardiovascular diseases. These flow and perfusion imaging studies were conducted on human pregnant volunteers in their second and third trimesters at 1.5T. Many of them were also examined by conventional Doppler ultrasound (US) and followed through delivery.

Flow-sensitive Alternating Inversion Recovery (FAIR) ASL MRI with background suppression was found to be feasible in detecting placental perfusion signal despite the presence of motion artifacts. An important consideration when studying placental ASL was the slow movement of maternal arterial blood in a large cavity called the intervillous space. This was a unique feature of placental anatomy which distinguished it from other organs containing capillaries. It became

apparent that traditional models to estimate perfusion from MRI were no longer applicable. In this work, a statistical approach was first developed to filter out motion artifacts, followed by a coordinate transformation to better represent the lobular distribution of blood flow in the intervillous space of the placenta.

The uterine arteries (UtAs) are the main maternal blood supply of the placenta and have also long been suspected to be involved in HPD, though US-based measurements have not yet been found to be highly predictive for widespread clinical use. In this work, 4D flow MRI enabled visualization of the tortuous UtAs while measuring volumetric flow rate. Its performance in predicting incidence of preeclampsia and small-for-gestational age births was comparable to Doppler US. When considering the innovative potential of 4D flow MRI to capture complex flow dynamics, this validation demonstrated the value of continuing technical development for improving HPD risk assessment.

Furthermore, centerline extraction of the maternal pelvic arteries in TOF MRI, from the descending aorta to the UtAs and external iliac arteries, provided quantitative metrics to characterize the geometry including path length and curvature. Pulse wave velocity (PWV) was estimated using path length by TOF MRI and velocimetry by 2D phase contrast and 4D flow MRI with results showing sensitivity to differences between UtAs and external iliac arteries. These approaches provided physiological metrics to explore and characterize the remodeling process of the uteroplacental arteries.

This dissertation demonstrates the feasibility of measuring structure and hemodynamics of the maternal vascular blood supply using non-contrast MRI that can lead to the more reliable biomarkers of adverse pregnancy outcomes needed to diagnose and treat HPD.

TABLE OF CONTENTS

LIST OF TABLES

LIST OF FIGURES

PREFACE

Chapter 4 has been presented as *Background-suppressed pulsed arterial spin labeling of placental perfusion at 1.5T* at the 2018 ISMRM 26th Annual Meeting in Paris, France and as *Pattern Analysis of Placental Blood Flow Distribution using ASL MRI* at the 2019 ISMRM 27th Annual Meeting in Montreal, Canada.

Chapter 5 has been published as: Hwuang, E., M. Vidorreta, N. Schwartz, B. Moon, K. Kochar, D. Tisdall, J. Detre, W. Witschey, (2018). *Assessment of uterine artery geometry and hemodynamics in human pregnancy with 4D flow MRI and its correlation with Doppler US.* Journal of Magnetic Resonance Imaging, https://doi.org/10.1002/jmri.26229. It was also presented as *Assessment of uterine artery hemodynamics in normal pregnancy with 4D Flow MRI* at the 2017 ISMRM 25th Annual Meeting in Honolulu, Hawaii.

Chapter 6 has been published as: Hwuang, E., P. Wu, A. Rodríguez-Soto, M. Langham, F. Wehrli, M. Vidorreta, B. Moon, K. Kochar, S. Parameshwaran, N. Koelper, D. Tisdall, J. Detre, W. Witschey, N. Schwartz. (2020). *Cross-modality and in-vivo validation of 4D flow MRI evaluation of uterine artery blood flow in human pregnancy,* https://doi.org/10.1002/uog.23112.

Chapter 7 has been presented as *Characterization of uterine artery geometry in normal pregnancy with time-of-flight angiography* at the 2018 ISMRM 26th Annual Meeting in Paris, France and as *Measurement of Uterine Artery and External Iliac Artery Pulse Wave Velocity using 4D Flow MRI* at the 2019 ISMRM 27th Annual Meeting in Montreal, Canada.

CHAPTER 1: OVERVIEW OF THE DISSERTATION

1.1 Clinical Relevance and Motivation to Address Hypertensive Pregnancy Disorders

Despite advances in obstetric care, preeclampsia remains one of the leading pregnancy complications in the world. Preeclampsia is a common type of hypertensive pregnancy disorder (HPD), a syndrome surrounding high blood pressure during gestation. More severe cases may present as a multi-system disorder including pulmonary edema, cerebral disturbances, and thrombocytopenia [1]. Rates of preeclampsia in the United States have been on the rise, with those delivering in 2003 at 6.7-fold increased risk compared to those delivering in 1980 [2]. Among inpatient deliveries in the United States, preeclampsia/eclampsia cases have risen 21% from 2005 to 2014 [3] (Figure 1). It is estimated that 3.4% of pregnancies involve preeclampsia [2]. HPD may occur in conjunction with intrauterine growth restriction (IUGR), defined as a fetus that has not fully attained its growth potential. HPD is known to have critical long-term effects not only in terms of fetal morbidity and mortality (accounting for 4-9% of stillbirths worldwide [4]) but also increased risk of maternal death (accounting for 15.9% of maternal deaths in the United States [5]) and maternal chronic illness, especially cardiovascular disease [6].

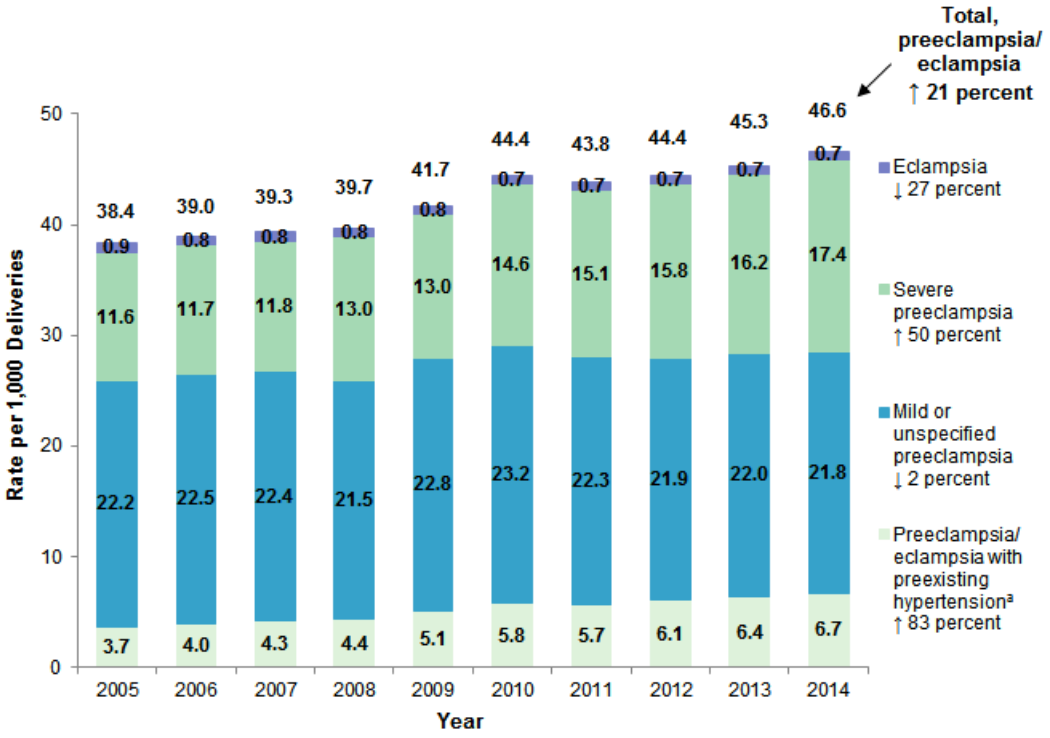

Figure 1 Rates of preeclampsia/eclampsia from 2005-2014 among inpatient deliveries in the United States [3]

Currently, the most effective way to stop the damaging effects of preeclampsia is to deliver the baby [7], but this has to be balanced with maximizing the gestational time for fetal development as there are also risks of preterm birth. Therefore, anti-hypertensive medications are often administered to protect the mother from hypertensive complication during or immediately after pregnancy. For example, aspirin is known to decrease blood pressure by inhibiting platelet activation and to improve endothelial dysfunction by allowing for increased vasodilation [8, 9]. Another example is calcium supplementation, which can relax vascular smooth muscle and inhibit vasoconstriction [10, 11]. Additionally, magnesium sulfate can be prescribed to prevent eclamptic seizures.

More research is needed to better understand molecular targets for treating adverse pregnancy outcomes. Fetal safety and medication use during pregnancy is understudied as most clinical

trials have been conducted at the exclusion of pregnant women [12, 13]. However, more and more women are on medications for chronic conditions during the period when they do not know that they are pregnant [13]. There are too few studies on the pharmacokinetic patterns of drug delivery and absorption in pregnant women. Therefore, there is a need for new technologies to assess the in vivo efficacy of drugs in real-time and better understand physiological changes in pregnancy that would have a critical effect on dosing [13].

Much research has gone into developing and testing screening methods for preeclampsia to identify patients who would benefit the most from treatment such as early delivery [7, 14] and anti-hypertensive therapy [9]. When screening with maternal factors and biochemical factors alone, only 40% of preeclamptic women were identified [15]. One of the most recent and promising first-trimester screening studies for preeclampsia consisted of a combination of maternal history, mean arterial pressure, uterine artery pulsatility index, and placental growth factor. It reported a detection rate for preterm preeclampsia of 67% with a screen-positive rate of 10% [16, 17]. However, multivariate models such as these are too complex for widespread clinical adoption so far [18].

These gaps in obstetric treatment and screening tools were brought to the forefront in 2014 when the National Institutes of Health identified the placenta as “the least understood human organ” [19]. This sparked a collective initiative to investigate the development, structure, and function of the placenta.

The goal of the Human Placenta Project is to develop technologies that would be able to evaluate the placenta safely, non-invasively, and in real-time. Given the growing body of evidence that placental abnormalities contribute to adverse pregnancy outcomes including HPD, the hope is to provide new avenues of patient care and improve the lifelong health of both mother and baby. A multidisciplinary team at the University of Pennsylvania responded to this call and was awarded a grant from the Human Placenta Project to investigate placental development by harnessing

existing multi-modality imaging tools. This consisted of: 1) ultrasound of structure and blood flow, 2) MRI of placental oxygenation, flow, and perfusion, and 3) near-infrared spectroscopy of pregnant women.

1.2 Current Technological Limitations in Uteroplacental Flow and Perfusion

The limited understanding of the pathophysiology of HPD is largely attributed to the lack of suitable technologies to investigate human uteroplacental hemodynamics. The current primary method for measuring uterine artery and placental blood flow is Doppler ultrasound (US) (Figure 2). While it does provide a real-time reading of velocity and is a portable and safe technology for obstetrics, it has a limited field of view and spatial resolution, making it difficult to reliably measure the cross-sectional area for volumetric flow in the tortuous uterine arteries and spiral arteries.

An alternative method for non-invasively measuring blood flow is MRI, which allows for multiple contrast mechanisms. Time-of-flight (TOF) angiography provides a large field-of-view and sufficient spatial resolution to visualize both uterine arteries, allowing quantification of vessel morphometry and cross-sectional areas. Phase contrast MRI has been used to measure blood flow in the uterine arteries, but 2-dimensional (2D) methods [20, 21] are limited because they require the imaging plane be oriented perpendicular to the vessel, a difficult task in the small and tortuous uterine arteries. 4D flow methods can potentially address this limitation by measuring flow dynamics in 3-dimensional space [22]. Arterial spin labeling (ASL) MRI has been used to measure placental perfusion at the microvascular level [23, 24] though the technique is vulnerable to motion artifacts and traditional signal models may not be accurate for the unique arteriovenous structure of the placenta.

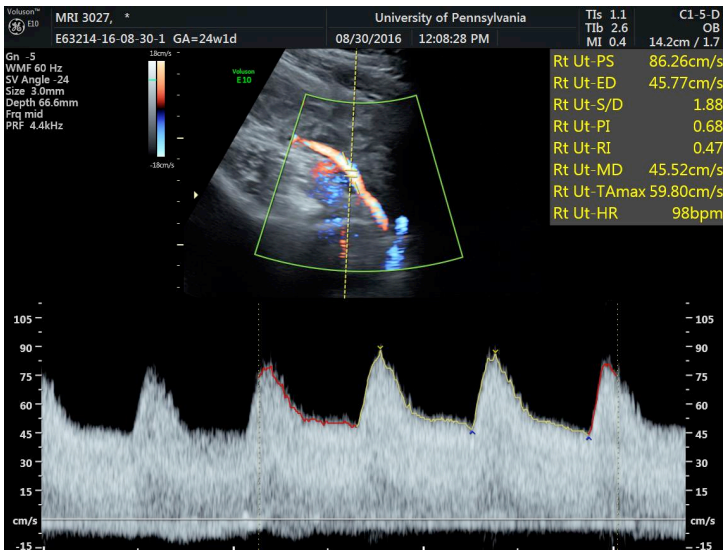

Figure 2 Example Doppler US of the right uterine artery in a representative subject

1.3 Research Objectives

The research described in this dissertation aims to address the need for better understanding of the pathophysiology of HPD by developing imaging and computational technologies for investigating the hemodynamics of pregnancy. The long-term vision is that improved knowledge about the maternal cardiovascular system can lead to better clinical management and a reduction in adverse pregnancy outcomes worldwide.

In support of this endeavor, this dissertation presents the following contributions:

- Development of ASL MRI acquisition and processing strategies for measuring placental perfusion
- Application of 4D flow MRI and TOF MRI for measuring uterine artery flow and pulse wave velocity in 2nd and 3rd trimester human pregnancy
- Validation of 4D flow MRI and its association with pregnancy outcomes

- Exploration of potential physiological biomarkers of HPD by estimating uterine artery path length, curvature, and pulse wave velocity from MRI data.

1.4 Dissertation Overview

This dissertation is organized as follows.

Chapter 2 begins with a description of the normal cardiovascular system followed by an explanation of the anatomical and functional changes that occur during pregnancy and HPD.

Chapter 3 provides a background on existing non-invasive technologies to assess cardiovascular disease.

In Chapter 4, an arterial spin labeling (ASL) MRI approach to measuring spiral artery function is described. Challenges to measurement accuracy by motion artifacts and the unique vascular structure of the placenta are addressed.

Chapter 5 presents non-invasive imaging of the uterine artery using ultrasound, 4D flow MRI, and TOF MRI.

Chapter 6 describes the assessment of HPD with non-invasive imaging and presents results from the association between 4D flow MRI and pregnancy outcomes.

In Chapter 7, feasibility of estimating path length and curvature from centerline extraction of TOF MRI of the maternal pelvic arteries is demonstrated. Also, feasibility of estimating pulse wave velocity from TOF and 4D flow MRI is shown. The potential utility of these parameters to test hypotheses about HPD physiology and pathophysiology is discussed.

Chapter 8 summarizes the dissertation with concluding remarks about MRI in pregnancy, limitations, and future directions.

CHAPTER 2: CARDIOVASCULAR SYSTEM AND PREGNANCY

2.1 Overview of the normal function of the cardiovascular system

The cardiovascular system is important for bringing oxygen and nutrients to tissues throughout the body and clearing metabolic waste. It also plays a critical role in regulating body temperature, endocrine function, and compensating for various physiologic conditions. It is comprised of a pump and a network of vessels to carry blood throughout the system [25]. The heart generates a pumping force on the blood with four chambers: left atrium, left ventricle, right atrium, and right ventricle. Oxygenated blood from the lungs enters the left atrium, then enters the left ventricle. The thick, muscular walls of the left ventricle allow it to pump blood into the aorta and on to the rest of the body. As peripheral tissues absorb and metabolize the oxygen delivered, the blood returning to the heart has reduced oxygen when it enters the right atrium and right ventricle. The right ventricle is also surrounded by muscle and generates enough force to deliver blood through the lungs to be reoxygenated before going back to the left atrium to continue the cardiac cycle. The peripheral vasculature is a network of arteries and veins to circulate blood throughout the body. The diameter of the vessels decreases from aorta to arteriole to capillary, and progressively increases again from venule to vein to vena cava. All vessels are internally lined with a thin layer of endothelial cells. In capillaries, this layer allows for transport of molecules between the vessels and the interstitium through diffusion, pore filtration, and pinocytosis [25]. Venules have an endothelial layer surrounded by fibrous tissue. The vessel walls of the aorta, arteries, arterioles, veins, and vena cava have layers of elastin, smooth muscle, and fibrous tissue surrounding the endothelial layer. However, the arterial vessels (aorta, arteries, arterioles) tend to have thicker walls compared to the venous vessels (venules, veins, vena cava) in order to sustain higher blood pressures and velocities (Fig. 3).

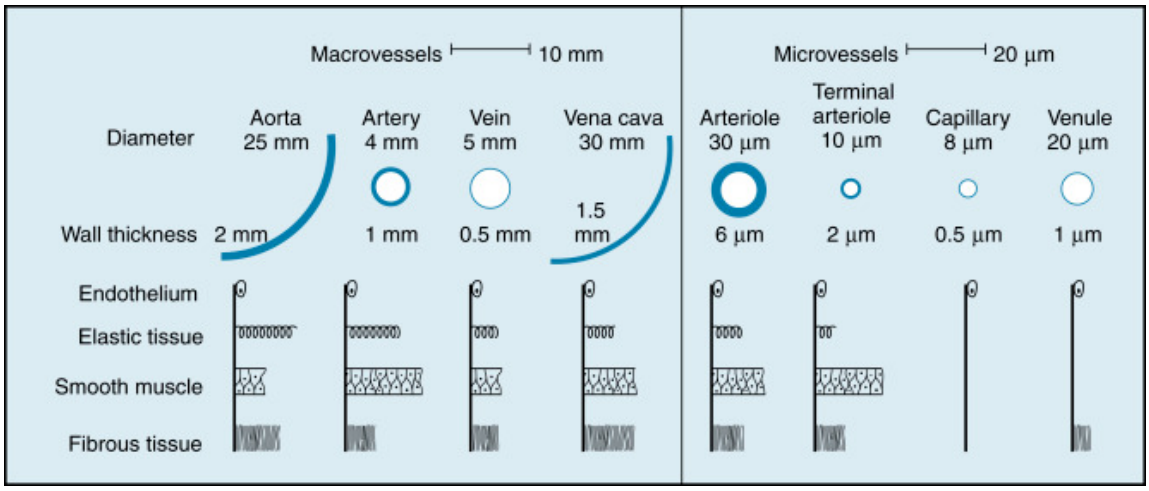

Figure 3 Description of vessel geometrical properties and tissue components in various blood vessel segments [25]. Note: Cross-sectional areas are not drawn to scale.

2.1.1 Hemodynamics of the arterial system

Hemodynamics is the study of the fluid properties of blood, the manner in which it moves through blood vessels, and how external pressures affect its movement. The rate at which blood is propelled from the left ventricle to the rest of the body is called the **cardiac output**. It is reported in mL/min and is calculated as a product of **stroke volume** (volume of blood ejected in one left ventricular contraction, mL) and **heart rate** (number of beats per minute, min^{-1}). The human body has mechanisms in place to adapt to the body's demands. For example, at rest skeletal muscle receives about 20% of the cardiac output but during exercise it can receive up to 80% [26].

The typical pressure of outflowing blood from the left ventricle, called **mean arterial pressure**, is about 100 mmHg and by the time blood returns to the right atrium, its pressure, referred to as **right atrial pressure**, is 2-6 mmHg [27]. This positive pressure difference is the primary driving factor of blood along blood vessels throughout the system. The **systemic vascular resistance**, reported in mmHg/mL/min, determines how much pressure is required to produce a given cardiac output. According to Darcy's law, cardiac output is directly proportional to this pressure difference

by a factor of 1/systemic vascular resistance, i.e. cardiac output = (aortic pressure – right atrial pressure)/systemic vascular resistance.

Besides pressure, there are other sources of fluid energy driving blood flow. Bernoulli's equation states that the mechanical energy of a unit volume of blood is additionally driven by potential/gravitational energy and kinetic energy:

$$\text{constant} = P_a + \rho g h + \rho v^2,$$

where P_a=aortic pressure, ρ=density of blood, g=gravitational acceleration, h=height, and v=velocity.

In the human circulatory system, the terminal arteries and arterioles are known to have the highest resistance because the pressure drop is the largest across those segments compared to other parts of the vascular network. This phenomenon can also be understood at the level of a single vessel; when blood is flowing through a cylindrical pipe, narrowing the lumen (at the same pressure and height) would decrease the flow (Darcy's Law) but increase the velocity (Bernoulli's equation). The Hagen-Poiseulle equation states that the resistance $R=8\mu L/(\pi r^4)$, where μ = fluid viscosity, L = length of pipe, and r = radius of pipe, which means that reducing the radius by a factor of 2 increases the resistance to flow by a factor of 16!

The shape of the velocity profile of blood flow in a vessel is a strong reflection of its underlying hemodynamics. Most blood flow in vessels is laminar, meaning that the velocity profile is parabolic, i.e. $v(r) = v_{max}*(1-r^2)/R^2$, where r = radial position and R = pipe radius. Velocity at the vessel wall is zero because of the molecular cohesive forces that restrict movement. This is often called the zero-slip condition. Velocity is the highest at the center of the vessel because of greatest distance from the molecular cohesive forces at the vessel wall. In locations such as the ventricles and near stenoses, the velocity profile is not laminar but turbulent. This means that the

flow pattern is more chaotic, the degree of which is described by the Reynolds number: Re = $vD\rho/\eta$, where v = velocity, D = vessel diameter, ρ = fluid density, and η = fluid viscosity. For different combinations of vessel geometry and flow conditions, there is a corresponding critical Reynolds number that serves as a threshold value beyond which turbulent flow occurs. For example, for uniform steady flow in a straight pipe the critical Re is approximately 2000. In blood vessels, flow is often laminar as Re is often below 2000 and can even reach as low as ~0.5.

Even though there is typically no velocity at the wall, the moving blood still exerts shear stress by tugging on the glycocalyx, a layer of polymers coating the endothelium. Wall shear stress functions as a signal to the endothelium to secrete molecules such as nitric oxide to vasodilate the vessel and reduce the wall shear stress. However, it is frequently the case especially in clinical settings that wall shear stress is ignored when calculating velocity. This is called “plug flow,” where the velocity profile is approximated as an average single value throughout the vessel and flow rate is computed multiplying the average velocity by cross-sectional area.

The hemodynamic concepts described thus far consider blood flow, pressure, and resistance at steady state. In actuality, the cyclical manner in which the heart contracts and relaxes produces pulsatile aortic pressure and cardiac output. The degree to which the pulsatile nature of pressure and flow is dampened in the rest of the body is based on the interaction between resistance and compliance of the arteries [28]. The Windkessel model [29, 30] has often been used to describe how pulsatile flow from the heart is dampened by the time it reaches the end organs. It states that blood pressure in the cardiovascular system is dependent on two parameters, resistance and compliance. The resistance is largely based on the radii of small arteries and arterioles. The compliance is largely based on the elasticity of large arteries. Arterial stiffness is often observed in hypertensive patients in whom the vessel compliance is very low and/or resistance is very high [31-34].

Research has shown that measuring pulse wave velocity, the speed at which a pressure wave generated by a heartbeat is transmitted throughout the cardiovascular system, can be useful for identifying high-risk patients for various cardiovascular diseases [35-39]. This is because a consequence of rigid arterial walls is that pulse wave velocity increases compared to less rigid arterial walls. This is approximated by the Moens-Korteweg equation

$$PWV = \sqrt{\frac{hE}{2r\rho}},$$

where h=wall thickness, E=elastic modulus, r=radius, and ρ=density of blood. Fig. 4 shows how PWV increases with age with one of the contributing factors being increasing elastic modulus.

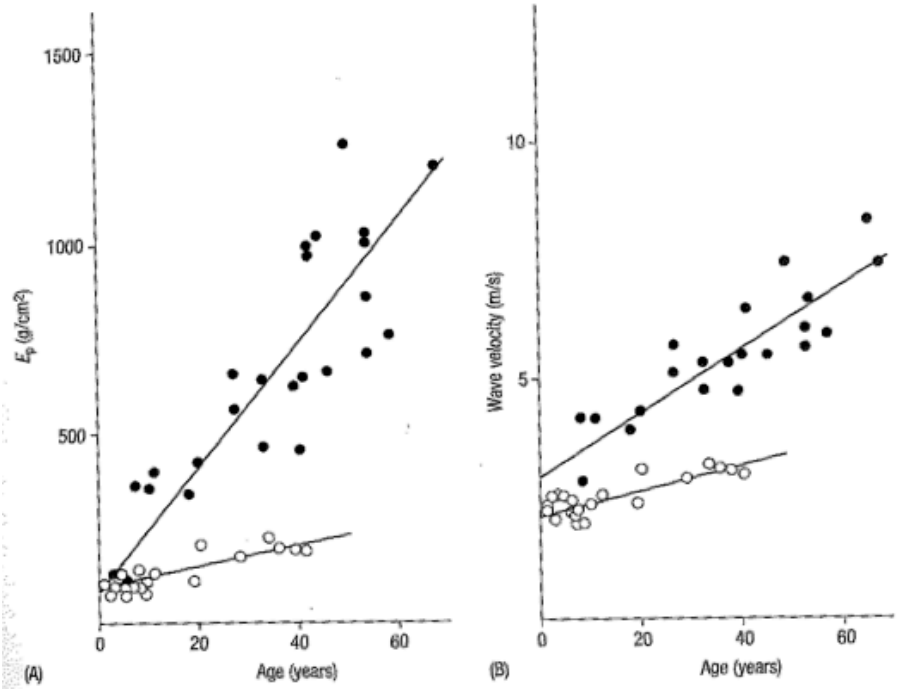

Figure 4 A) Plot of elastic modulus (Ep) as age increases and B) plot of PWV as age increases. Solid circles (•) denote proximal thoracic aorta and open circles (○) denote proximal pulmonary artery [28, 40]

2.1.2 Hemodynamics of the venous system

After oxygenated arterial blood is metabolized by end organs, deoxygenated blood is returned back to the heart via the venous system. Veins and venules are notable for their thin, distensible walls and are able to contain a large volume of blood with a small increase in pressure. In fact, they can be up to 50x more compliant than arteries and arterioles [26]. Venous pressure tends to be negative above heart level. Central venous pressure, an estimate of right atrial pressure, is typically measured noninvasively by having the patient lie semirecumbent supine and locating the point of collapse of the jugular vein. This is roughly the location where the transmural pressure is nearly 0, i.e. the blood pressure matches atmospheric pressure. The distance between the collapse of the jugular vein and the manubriosternal angle plus the distance between the manubriosternal angle and the right atrium (estimated to be 5 cm) is the central venous pressure in cm blood or converted to cmH_2O [26].

While venous blood flows continuously, the effect of gravity does increase pressure in the lower part of the body below the heart and decrease central venous pressure, a phenomenon called orthostasis. To counterbalance this effect, skeletal muscle acts as a pump to contract and compress veins, which contain valves that close and prevent retrograde flow of blood away from the heart. When the muscle relaxes, the valves open and venous blood flows toward the heart. During aging, malfunctioning valves can cause varicose veins and leg ulcers from abnormally high venous pressure in the lower extremities. Respiration also encourages venous return during inspiration, when intrathoracic pressure decreases and intraabdominal pressure increases. Expiration creates the opposite effect and reduces intrathoracic venous blood flow [26].

2.1.3 Fluid properties of blood

Blood is made up of red blood cells, white blood cells, platelets, plasma, and nutritional macromolecules. The bone marrow houses pluripotent stem cells that self-replicate to form

specialized cells that enter the circulating blood. These specialized cells include erythrocytes, leukocytes, and megakaryocytes [25].

Erythrocytes are commonly known as red blood cells. They contain hemogloblin protein molecules that bind reversibly to oxygen molecules based on pH, temperature, and concentration of 2.3-diphosphoglycerate. This is important for transporting oxygen from the lungs to other organs. Aberrations in the protein structure of hemoglobin and in the concentration of erythropoietin (erythrocyte-producing hormone) in the human body can affect the availability of oxygen for metabolism.

Leukocytes are commonly known as white blood cells. They are primarily responsible for helping the body fight against infection through the removal of foreign material and cellular debris. Megakaryocytes in the bone marrow divide into small fragments called platelets that enter circulating blood. Platelets play an important role in coagulation and cell repair when there is bleeding. Blood also contains macromolecules such as proteins, carbohydrates, and fatty acids suspended in a solution called plasma. These nutrients are transported through the circulation to various parts of the body for metabolism or storage.

The constituents of blood also have an effect on hemodynamics. Most discussions of hemodynamics in cardiovascular physiology approximate blood as a homogeneous, incompressible, Newtonian fluid. This simplifies the equations used to describe hemodynamics and renders them practical for clinical and research purposes. However, blood is actually non-homogeneous, compressible, and non-Newtonian because approximating the fluid properties of blood can sometimes lead to non-negligible errors.

For reference, the viscosity of pure water remains constant with changes in shear rate (i.e. a Newtonian fluid) and is therefore classically determined by Poiseulle's Law. In contrast, blood is a suspension of various cells, molecules, and other biological constituents and its viscosity changes

with shear rate (i.e. a non-Newtonian fluid). For this reason, Poiseulle's Law is not accurate in characterizing blood. Specifically, blood is a shear-thinning fluid because viscosity decreases with increasing shear rate. The Fåhræus-Lindqvist phenomenon describes how blood viscosity is lower in vessels with diameters <0.3 mm (size of small arterioles, venules, and capillaries) [41]. In these small vessels, high flow rate is associated with red blood cells tending to flow in the axial part of the velocity profile while the rest of the blood such as plasma have lower flow rates near the vessel wall. This effect is modulated by the concentration of fibrinogen and the flexibility of red blood cells [25].

2.2 Systemic regulation of blood flow and normal pregnancy physiology

The cardiovascular changes that occur in normal human pregnancy are significant and comprehensive. It has been observed that the heart displaces superiorly and leftward with the expanding uterus [42]. The ventricular wall undergoes eccentric hypertrophy primarily in the first trimester and later accommodates increased end-diastolic blood volume in the second and third trimesters [43]. The ventricular muscle has also been found to be more compliant, believed also to support vasodilation and larger blood volume.

2.2.1 Hemodynamics of the arterial system in pregnancy

These anatomical changes to the heart allow for an increased cardiac output by 30-50% compared to a non-pregnant woman [43]. The cardiac output increases most rapidly in the first trimester and plateaus by the third trimester. One study found the average cardiac output to be 4.88 L/min pre-pregnancy and 7.34 L/min by delivery [44]. The cardiac output also redistributes in pregnancy with a larger percentage of blood going to the uterus and breasts compared to pre-pregnancy (Fig. 5).

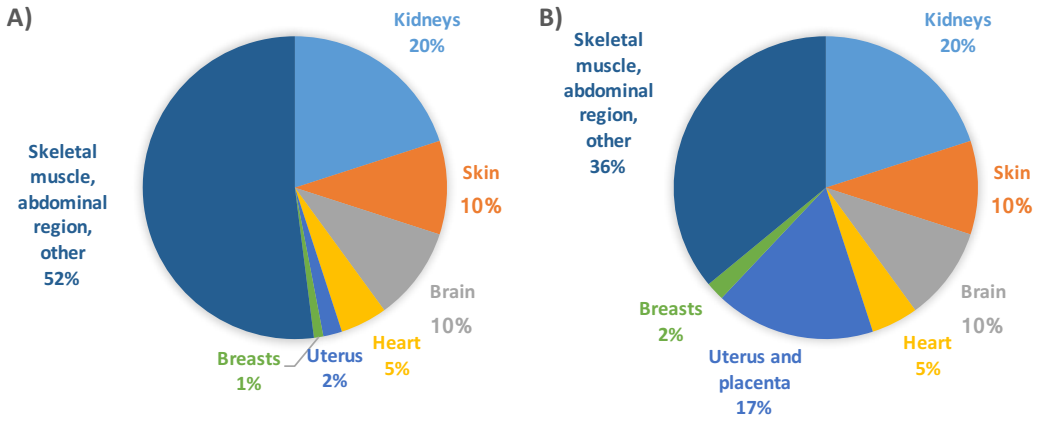

Figure 5 Pre-pregnancy (A) and pregnancy (B) distribution of cardiac output to end organs

As mentioned previously, cardiac output is the product of stroke volume and heart rate. In pregnancy, cardiac output increases because both stroke volume and heart rate increase. Typically, the stroke volume increases rapidly in the first trimester, reaches its peak in mid-gestation and falls slightly by term, whereas the heart rate increases steadily until late third trimester when it plateaus until term.

Darcy's Law states that the product of cardiac output and systemic vascular resistance are about equal to the difference between mean arterial pressure and right atrial pressure (or central venous pressure). The increase in cardiac output during pregnancy is counterbalanced by a drop in systemic vascular resistance, which reaches its lowest point mid-gestation and rises slightly by delivery. The decrease in systemic vascular resistance causes both mean arterial pressure and the difference between mean arterial pressure and right atrial pressure to decrease while the right atrial pressure stays the same [43]. Decreasing systemic vascular resistance is believed to prevent the heart from needing to work too hard to pump a larger blood volume throughout the body. This is believed to be mediated through the nitric oxide pathway resulting in vasodilation and increased vascular compliance [25, 43]. Fig. 6 shows the trajectory of cardiac output, mean arterial pressure, and systemic vascular resistance during gestation [45].

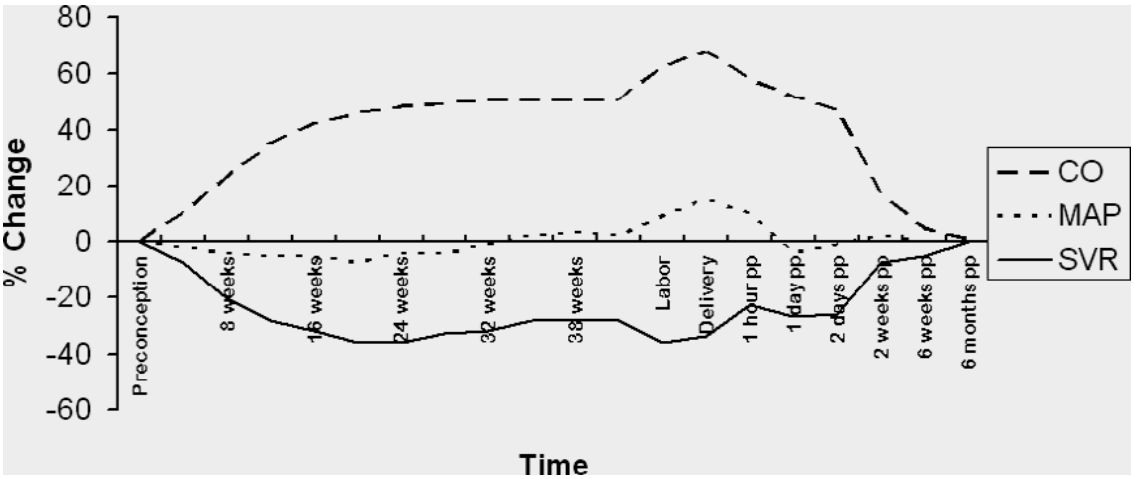

Figure 6 Time-resolved graph of cardiac output (CO), mean arterial pressure (MAP), and systemic vascular resistance (SVR) changes throughout the course of pregnancy [45]. These hemodynamic alterations typically resolve 6 months after delivery.

Although most women are able to lie supine while pregnant without experiencing hypotensive symptoms, up to 8% of women do experience supine hypotensive syndrome, which includes low blood pressure and low heart rate [43]. This is explained by compression of the inferior vena cava by the uterus, which decreases venous return, stroke volume, and cardiac output. In symptomatic women, lateral decubitus positioning is recommended to minimize the reduction in cardiac output [42].

2.2.2 Hemodynamics of the venous system in pregnancy

Venous blood pressure in the upper extremities does not generally change with pregnancy but tends to rise in the lower extremities. Venous blood vessels also increase in compliance which leads to low flow rate and stasis. These conditions explain why pregnant women are known to develop or be at risk of developing thrombosis, edema, and varicose veins in the lower extremities. Another area where women are at risk of developing edema is in the lungs. As the blood volume in pregnancy increases, the colloid oncotic pressure can decrease while the pulmonary capillary wedge pressure (estimate of left atrial pressure) can increase. When it is

difficult for fluid to be reabsorbed or retained in the capillaries, fluid can potentially enter the alveoli and cause pulmonary edema with signs of dyspnea and reduced exercise tolerance [25].

2.2.3 Fluid properties of blood in pregnancy

In pregnancy, the overall blood volume increases 40% [46]. The two main contributing factors are: 1) a 20-30% increase in red blood cell mass and 2) a 45% increase in plasma volume. Red blood cell expansion is mediated by increased production rather than the extension of cell life in the circulation. In pregnancy there is a higher concentration of 2,3-diphosphoglycerate (2,3-BPG) which encourages oxygen to dissociate from maternal hemoglobin and bind to fetal hemoglobin. It has been postulated that NO-mediated vasodilation of vasculature and retention of water and sodium cause plasma volume to increase from 3.1-4 L (middle of first trimester) to 4.7-5.2 L (middle of third trimester). The increase in plasma volume is generally higher than the increase in red blood cell mass so often hematocrit is lower in pregnant mothers than in non-pregnant women.

There is a significant increase in the number of leukocytes in pregnancy with a white blood cell count of ~8000/mm^3 in the first trimester and up to 30,000/mm^3 during labor and delivery [51]. This is believed to result from the general stress of pregnancy rather than infection; the white blood cell count typically resolves post-partum [51, 57]. The increase in neutrophils accounts for most of this expansion. The number of lymphocytes first decreases from the first to second trimester, and then increases in the third trimester. The increase in monocytes has been interpreted as playing a role in preventing fetal allograft rejection by the maternal immune system [57].

Pregnancy is often described as a hypercoagulable state, which is believed to protect the mother from severe peripartum hemorrhage. However, this does put her at risk of thromboembolic disease considering the presence of three main contributing factors: vascular damage, venous

stasis, and a pro-coagulation circulatory milieu. The vascular damage comes from general venodilation and venous stasis from compression of the inferior vena cava as well as major pelvic veins [53]. Features of hypercoagulability in pregnancy include increased Protein S activity, increased resistance to activated Protein C (despite relatively unchanged levels of Protein C), and increased fibrinogen and other factors that promote thrombin production.

The platelet count decreases in pregnancy and can be as low as 70,000-150,000/mm^3 (for comparison, non-pregnant platelet count range is 150,000-400,000/mm^3) probably because of increased plasma volume and increased clearance of platelets [51, 57]. This condition is called gestational thrombocytopenia, resolves a couple weeks after delivery, and has not been found to have negative effects on the pregnancy [51]. It is believed that gestational thrombocytopenia is balanced by increased platelet aggregability to prevent excessive bleeding.

The composition and transport efficiency of nutrients in the circulatory system are not only important in pregnancy for supporting maternal health but also determine healthy fetal development. In pregnancy, the body's need for iron significantly increases probably because of the demands of erythropoiesis, the process of generation of new red blood cells [47]. In fact, normal pregnant women can become slightly anemic and are encouraged to take iron supplements. Two other important nutrients are folate and vitamin B12, which are believed to be important for healthy neural tube development in the fetus as well as the prevention of anemia.

In pregnancy, whole blood viscosity decreases as gestation progresses. This primarily results from the increase in plasma volume outpacing the increase in red blood cell mass, sometimes termed "hemodilution," a phenomenon reflected by clinically decreased hematocrit [48]. Since blood is a non-Newtonian, shear-thinning fluid, its viscosity is higher at low shear rates than at high shear rates. At low shear rates, such as in small veins and in the intervillous space of the placenta, the viscosity is high. High viscosity enhances red cell aggregation and impedes flow but the lower hematocrit of maternal blood counterbalances this effect by lowering viscosity. In

general, it is believed that low viscosity of blood plays a role in low resistance blood flow in pregnancy to ensure efficient transfer of nutrients in the placenta [43].

2.3 Normal physiology of placental development, function, and remodeling of uteroplacental circulation

2.3.1 Stages of placental development

The multi-functional nature of the placenta as the “fetal renal, respiratory, hepatic, gastrointestinal, endocrine, and immune systems” [19] makes it a profoundly unique organ of the human body with significant consequences of long-term health of mother and child. Figure 7 outlines the stages of placental development in each trimester, the details of which will be explained in the ensuing paragraphs. For the purpose of understanding the stages of placental development it is helpful to summarize the key components of a mature placenta. The placenta is a disc-shaped organ attached to the inner uterine wall near the anterior or posterior side of the maternal pelvis. The placenta itself is divided into the maternal side and the fetal side. On the maternal side is the uteroplacental interface, which is also called the basal plate. At this junction is where maternal blood enters the central cavity of the placenta, called the intervillous space (IVS). The fetal side is also called the chorionic plate, from which the umbilical cord extends outward and attaches to the umbilicus of the fetus. Within the chorionic surface the umbilical cord is connected to a network of vessels arranged in a tree-like structure called villi. The terminal branches of the fetal villi project into the intervillous space and are therefore bathed by maternal blood. In this configuration, the fetal circulation and maternal circulation never mix but oxygen, metabolites, and waste are transferable in a regulated manner across a thin layer of cells on the surface of the fetal villi [49]. In this way, the placenta temporarily performs the functions of various organs for the fetus while the fetus’s own organs are in development.

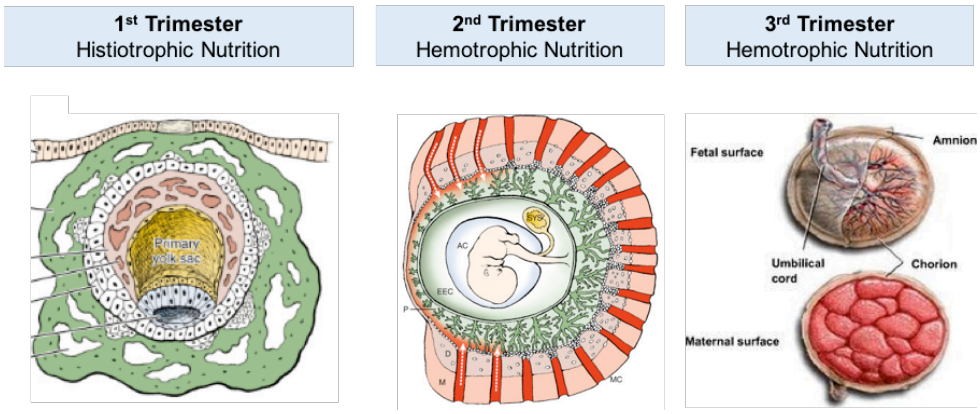

Figure 7 Stages of placental development from first to third trimester (adapted from [42] and [50]). In the first trimester, histiotrophic nutrition provided by endometrial glands supports cell differentiation in the blastocyst to form the primitive structures of the placenta. In the second trimester, the remodeled maternal spiral arteries become patent and deliver blood to the intervillous space. Nutrients and waste pass between the maternal blood pool in the intervillous space and the fetal circulation through the membrane of the fetal villi. By the third trimester, the mature placenta has formed lobular structures on the maternal surface and the umbilical cord attaches near the center of the placenta on the fetal surface.

Placental development in the first trimester consists of a series of cellular changes that occur during fertilization and implantation. In humans, fertilization occurs in the fallopian tubes of the mother, after which the zygote differentiates into a blastocyst as it travels into the uterine cavity. The blastocyst orients such that the inner cell mass and the trophectoderm are near the uterine wall. Then, the trophectoderm is expelled from the blastocyst. The expelled trophectoderm is called extravillous trophoblast (EVT), meaning that it will not be directly part of the placenta, but it plays the key role of invading the inner third of the myometrium for secure anchorage of the placenta. Furthermore, the EVTs differentiate into endovascular EVTs and interstitial EVTs. The endovascular EVTs migrate into the lumens of the maternal spiral arteries and partially replace the smooth muscle layer and endothelium of the terminal segments with fibrinoid tissue [42, 51]. The interstitial EVTs facilitate this process in the stroma surrounding the spiral arteries.

For the first 9 weeks or so of pregnancy (most of the first trimester), the growing placenta, umbilical cord, and embryo are supported by **histiotrophic nutrition** [52]. At this stage, the

endovascular EVTs occlude the spiral arteries while remodeling occurs such that only small amounts of blood plasma can enter through. Nutrients from this plasma and surrounding endometrial glands nourish the young placenta and fetus in early development. The placenta begins to form as syncytiotrophoblast cells surround the blastocyst, lacunar spaces enlarge to form the IVS, hemangioblasts differentiate to form the fetal villi, and part of the yolk sac becomes umbilical cord.

By the end of the first trimester, the plugs formed by endovascular EVTs occluding the spiral arteries disintegrate and maternal blood carrying oxygen and nutrients enter the IVS. This marks the beginning of placental development supported by **hemotrophic nutrition** [52], which lasts throughout the second and third trimesters. The quality of hemotrophic nutrition hinges on the terminal ends of the spiral arteries to properly convert from narrow vessels (0.4-0.5 mm diameter) into wide, trumpet-like conduits (2-3 mm diameter) opening into the IVS. Mathematical modeling has demonstrated that there are essential hemodynamic consequences in the IVS from EVT-mediated remodeling of the spiral arteries [53]. First, the wide terminal vessels help slow down the speed of inflowing blood to prevent damage to fragile villi based on a modified version of Poiseulle's equation (Fig. 8a). Second, slow blood flow maintains a circulation duration of approximately 25 seconds in the IVS to allow time for transport of oxygen and nutrients. Third, maintaining lower pressure in the IVS compared to fetal villi ensures that the fetal villi are able to dilate, thereby maintaining a thin barrier for oxygen and nutrients to cross (Fig. 8b). Fourth, loss of vasoactive smooth muscle cells allows the constancy of flow to be maintained to prevent a situation where intermittent delivery of oxygen would lead to placental oxidative stress.

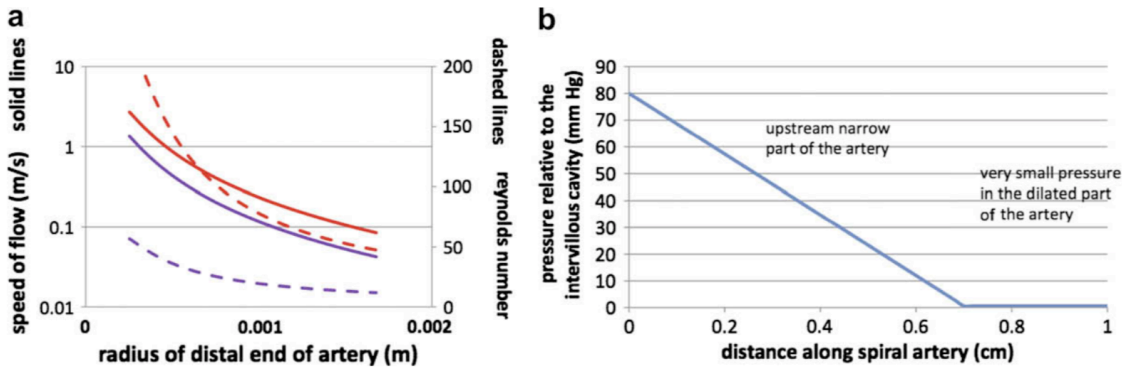

Figure 8 Results from mathematical model of spiral artery remodeling presented in Burton et al. [53]; a) graph showing dramatic decrease in speed of blood flow when the radius of the spiral artery increases, b) graph showing decrease in pressure along the unremodeled proximal end of the spiral artery until it matches the pressure of the IVS in the wide, trumpet-like terminal end of the spiral artery after remodeling.

Although blood is able to percolate freely throughout most of the IVS, the placenta is partially divided into 10-40 lobules by septae [42, 54]. Each lobule consists of one spiral artery ejecting blood toward two or three fetal stem villi. The syncytiotrophoblast cells comprising the thin membrane on the fetal villi mediate regulated transport of substances such as water, oxygen/carbon dioxide, proteins, steroid hormones, inflammatory factors, and waste into and out of the fetal circulation. Oxygen and other gases cross by diffusion whereas larger substances cross by channels, transporters, vesicles, receptor-mediated processes, and other mechanisms [42]. In fact, researchers have found evidence that the placenta is a metabolically active organ with oxygen consumption matching that of the fetus [55]. It also has high expression of enzymes for glucose metabolism [56].

Hemotrophic nutrition of the fetus and placenta continues in the third trimester until term. The thickness of the placenta stops increasing at about 2.3-3 cm in the mid-second trimester but the circumference continuously increases until term [42, 57]. The mature placenta is measured at 15-20 cm in diameter [42, 57] and weighs 450-508 g. The fetal villous surface amounts to about 10-14 m^2 in surface area available for exchange [42]. Placental biologists have observed similarities

between third trimester placental tissue and the aging of other organs [58]. The underlying process is called cellular senescence, when irreversible cell cycle arrest causes the cell to cease dividing. It has many characteristic biomolecular features including unrepaired DNA damage. The fusion of cytotrophoblasts to form multi-nuclear syncytiotrophoblasts is an important process in pregnancy. This process begins in early pregnancy and continues as syncytiotrophoblasts at the end of terminal villi often break off, enter maternal blood, and must be constantly regenerated until term. Research has shown that syncytiotrophoblast cells inherently present with characteristic features of senescent cells, such as the inability to divide and minimal DNA synthesis. Senescent cells in the maternal stroma and fetal membranes have also been observed to play an important role in concluding pregnancy. It is believed that one of the early processes of labor is the release of sterile inflammatory signals from these cells. This is followed by remodeling of the uterus and cervix to prepare for birth.

2.3.2 Anatomical and physiological remodeling of maternal pelvic vasculature

The surrounding maternal vasculature also undergoes remodeling during placental development as the placenta receives its blood supply from a network of vessels in the female pelvis. Anatomically, the left and right common iliac arteries branch off of the aorta and divide into the left and right internal and external iliac arteries. On each side, the internal iliac artery divides into several branches providing oxygenated blood to organs and tissues in the gluteal and pelvic region. One of these branches is the uterine artery, a tortuous vessel that eventually attaches to the uterine wall. It is believed that the tortuosity of the uterine arteries helps accommodate enlargement of the uterus by extending its undulations, potentially preventing rupture during pregnancy [49] (Fig. 9a,b). There may be some natural anatomical variation in the origin of the uterine artery in some women. The uterus is supplied by two arterial systems (uterine and ovarian arteries) and drained by two venous plexuses (uterine and ovarian veins).

The uterus receives oxygenated blood primarily from the uterine arteries and ovarian arteries joined by the utero-ovarian communicating arteries. There is also a small contribution from the blood vessels contained within the broad ligament, a sheet of tissue draped over the ovaries, ovarian arteries, uterine arteries, and other tissues supporting the uterus [49]. Studies have shown that occluding the internal iliac arteries lead to recruitment of collateral flow from branches of the aorta, external iliac artery, and femoral artery [59]. The redundancy in blood supply appears to play a protective role in maintaining blood flow to the uterus [49].

The uterine arteries ascend the two sides of the uterine wall within the broad ligament. When they penetrate the myometrium, they divide into smaller branches called the arcuate arteries which course in a semicircular pattern in the outer third of the myometrium. There are anastomoses that form between the left and right arcuate arteries and between arteries and veins. The arcuate arteries branch into the radial arteries which head towards the endometrium and terminate as spiral arteries to supply blood flow to the endometrium [59] (Fig. 9c).

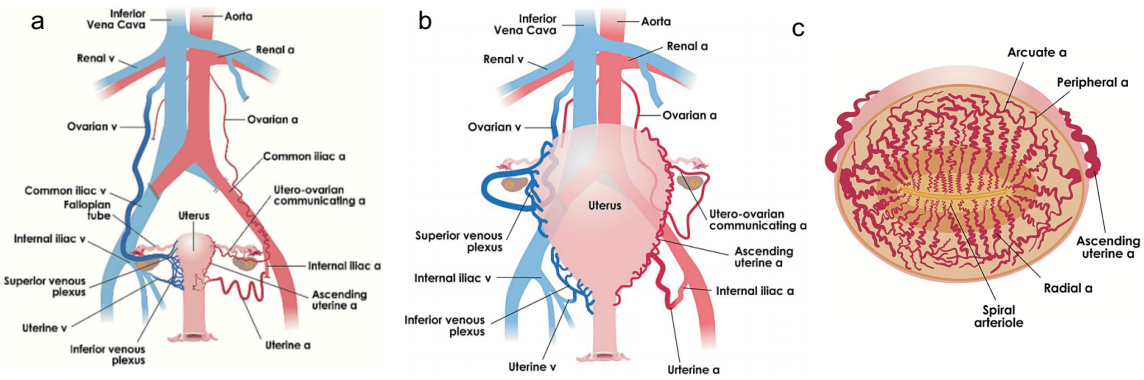

Figure 9 Vascular anatomy of a) non-pregnant female and b) pregnant female. Panel c shows a cross section of the uterus showing the smaller branches of the myometrial arteries feeding the placenta in pregnancy [49]

As gestation progresses, it has been observed that uterine arteries carry 20-50 mL/min of blood in the non-pregnant state but this increases up to 800 mL/min of blood in the pregnant state [60, 61]. This 10-fold increase is mediated by a decrease in uterine artery resistance since the pressure=flow*resistance (Darcy's Law) and pressure is generally maintained constant. Recall that the Hagen-Poiseulle equation states that the resistance ($R=8\mu L/(\pi r^4)$), where μ = fluid viscosity, L = length of pipe, and r = radius of pipe. Although elongation of the uterine artery alone would increase R, it is overcompensated by circumferential remodeling (increased r). As the fourth power in the denominator indicates, an increase in the uterine artery radius contributes significantly to the decrease in R. Specifically, this vasodilation has been described as "outward hypertrophic" meaning an enlargement of lumen area without much wall thickening. Based on animal studies, both smooth muscle cell hypertrophy and hyperplasia contribute to this luminal enlargement [60, 62].

Interestingly, the uterine artery diameter increases weeks before the 10^{th} week when trophoblasts invade the spiral arteries. This appears to be anticipatory in order to provide enough influx of blood flow at the start of hemotrophic nutrition around the 13^{th} week. The blood flow increase begins to plateau by the third trimester [57, 63], while the fetal weight begins to increase in the second trimester with fastest growth in the late third trimester [49, 64]. Finally, there is a decrease in uterine artery flow, which is consistent with observed increase in myogenic tone at the end of the pregnancy to reduce hemorrhage [46, 62, 65]. The time course of all these hemodynamic changes in the female pelvis demonstrates how the blood supply is prepared and maintained to support the pregnancy yet without too much blood loss by term.

2.4 Pathophysiology of hypertensive pregnancy disorders

2.4.1 Historical progression in the understanding of HPD

The current clinical understanding of hypertensive pregnancy disorders traces back to 3000 B.C., which is estimated to mark the earliest written reports of eclampsia from nearly every continent [66]. Prior to the era of scientific inquiry, various theories proposed included possession by evil spirits in biblical times and imbalance of “humours” by Hippocrates [67]. The earliest risk factor of pregnancy-associated convulsions was primiparity reported in 1694. In the 1840s, proteinuria was discovered as an early manifestation of eclampsia, leading to the term “preeclampsia.” At this time, however, toxemia was believed to be the culprit, leading to the practice of blood-letting in attempt to temper the disease. Following the invention of the blood pressure cuff in 1897, hypertension was discovered in some pregnant women with and without edema, proteinuria, and convulsions. In 1976, the phrase “hypertensive disorders of pregnancy” was coined to convey the spectrum of this disease encompassing gestational hypertension, preeclampsia, eclampsia and their subtypes [68]. Starting in the 1960s, placental examinations and placental bed biopsies revealed evidence of shallow implantation in cases of HPD. Specifically, it appeared that the trophoblasts failed to fully invade the spiral arteries at the inner third of the uterine myometrium, resulting in persistence of narrow, muscular vessel walls rather than fully converting to the necessary wide, flaccid conduits needed for adequate delivery of blood flow to the placenta and fetus (Fig. 10).

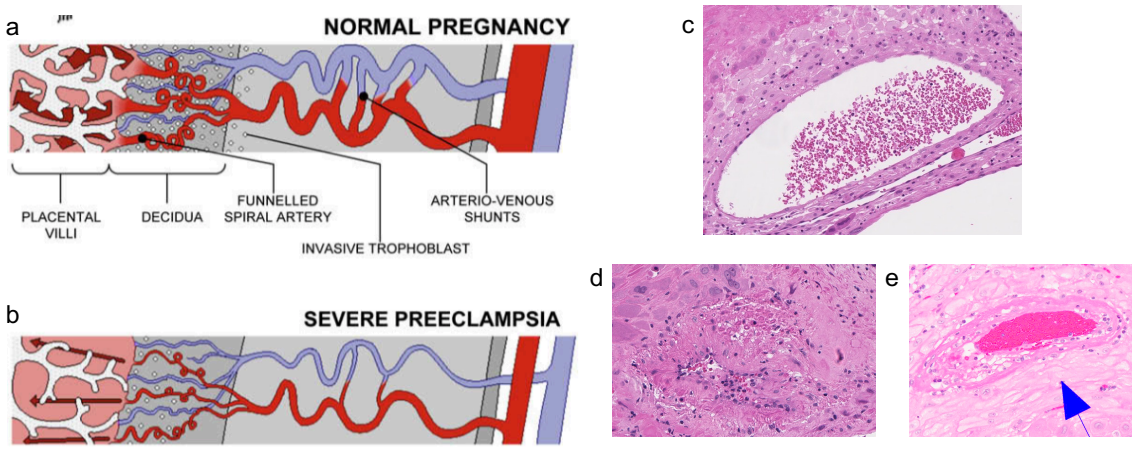

Figure 10 Comparison of normal and abnormal spiral artery morphology commonly observed in preeclampsia: a) diagram of physiologic terminal spiral artery conversion to large funnel-like vessels, b) diagram of narrow spiral arteries restricting blood flow into the placenta, c) normal basal plate vessel from normal uterine remodeling, d) basal plate vessel with visible thick, smooth muscle layer of vessel wall because of incompletely remodeled spiral artery, e) basal plate vessel with acute atherosis and fibrinoid necrosis possibly because of poor spiral artery remodeling. Panels a,b were adapted from [53] and pathology images in panels c,d,e were provided by Rebecca Linn, MD at Children's Hospital of Philadelphia.

However, the view that defective trophoblast invasion of the spiral arteries was the primary cause of HPD was later challenged with the observation that some women with preeclampsia do not have placental disease while placental disease can be present in other women who do not have preeclampsia yet have small-for-gestational age fetuses [69].

In the 1980s, attention began to shift toward endothelial dysfunction as the phenomenon explaining the multi-organ involvement in HPD as more clinical features were described. These included glomerular endotheliosis, liver disease, and eclamptic convulsions. Serological analysis of pregnant women with and without preeclampsia showed similar biochemical profiles as those with hemolytic uremic syndrome, pointing to possible endothelial injury activating the coagulation cascade and a maternal circulatory environment that is hypersensitive to vasopressors [70]. Some explanations for endothelial dysfunction in pregnancy are pre-existing chronic hypertension, type II diabetes, and generalized maternal inflammatory response [69, 71].

2.4.2 Overview of current theories regarding placental and cardiovascular origins of HPD

Today, HPD, particularly preeclampsia, continues to be referred to as “a disease of theories” [66]. The unifying theme in all these theories appears to be the debate over how placental disease is connected with the maternal systemic manifestations, given that both do not always occur in HPD-related adverse pregnancy outcomes. Roberts et al. suggest that shallow implantation of the placenta with poorly remodeled spiral arteries leads to release of biochemical factors that injure the endothelial cells of the rest of the circulation [70]. This appears to be consistent with glomerular endotheliosis and other signs of organ damage. This could also explain why HPD is cured by delivery of the placenta [67, 70]. On the other hand, Kalafat et al. argue that placental malperfusion is secondary to cardiovascular impairment because endothelial dysfunction can impair the response of uteroplacental arteries to vasodilators and other remodeling factors [72] (Fig. 11).

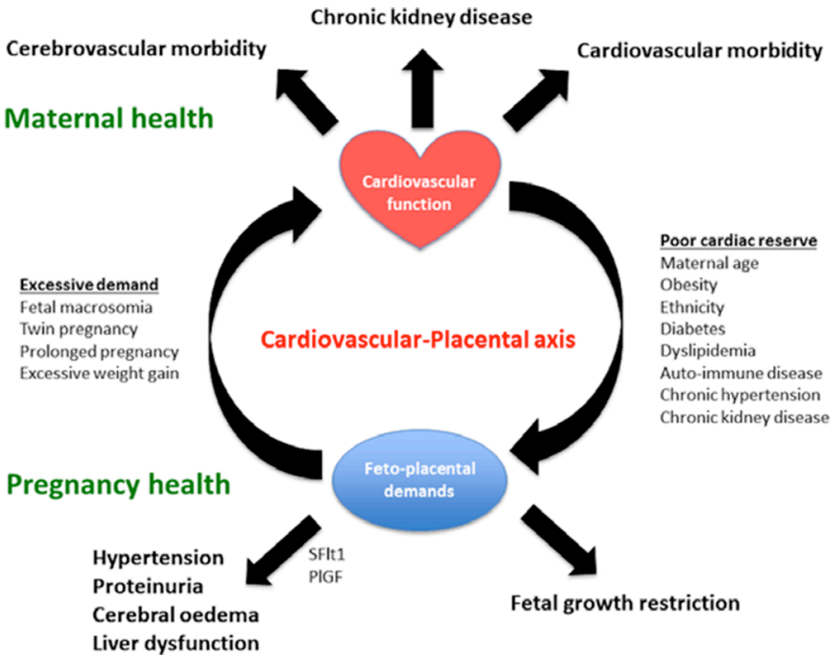

Figure 11 One theory proposed to explain the mechanism of preeclampsia states that initial poor cardiac reserve makes the maternal cardiovascular system susceptible to disease because of poor adaptation to the demanding physiological changes of pregnancy [73]. This positive feedback loop puts mother and fetus at further risk over time. This leads to the final common pathway of signs and symptoms commonly observed in patients include hypertension and proteinuria.

A convincing perspective held by many today takes into account the two subtypes of preeclampsia: **early-onset preeclampsia** is defined as disease detected prior to 34 weeks gestation and **late-onset preeclampsia** as disease detected after 34 weeks gestation. Studies have shown that early-onset preeclampsia is more strongly associated with fetal growth restriction, placental lesions related to maternal underperfusion, and lower placental weight compared to late-onset preeclampsia [74, 75]. Late-onset preeclampsia is more associated with maternal obesity and large-for-gestational age fetuses [76, 77]. As a result, some have suggested viewing early-onset and late-onset preeclampsia as having two separate etiologies, placental or maternal, respectively [74].

2.4.3 Clinical perspective of hypertensive pregnancy disorders

2.4.3.1 Categorization of HPD

HPD is a broad term encompassing various forms of hypertension during pregnancy, including chronic hypertension, gestational hypertension, preeclampsia, and eclampsia. Chronic hypertension refers to preexisting hypertension prior to 20 weeks gestation while gestational hypertension is new onset of hypertension after 20 weeks of gestation. Preeclampsia is defined as new onset of hypertension after 20 weeks of gestation *and* proteinuria or, in the absence of proteinuria, with the presence of thrombocytopenia, renal dysfunction, liver dysfunction, or pulmonary edema [78]. Figure 12 is a diagram illustrating the various types of HPD. Preeclampsia is the primary focus in the following sections, although there may be overlap with other forms of HPD in terms of risk factors, screening, and treatment.

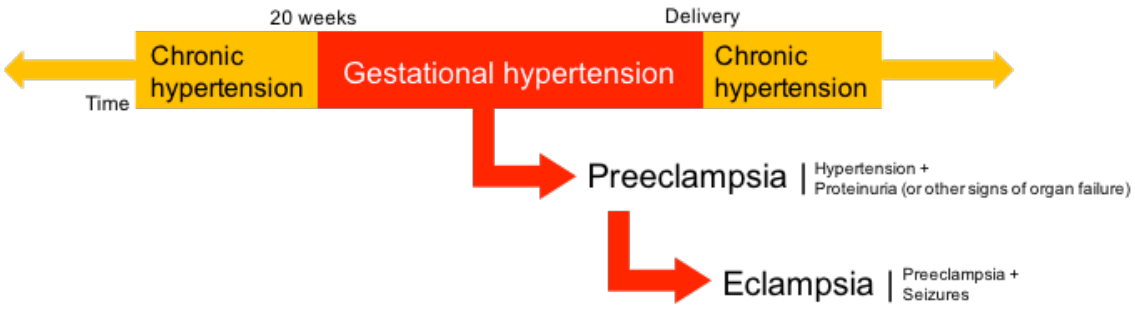

Figure 12 Types of HPD arranged by timing of occurrence during gestation, signs, and symptoms

2.4.3.2 Risk Factors of HPD

The risk factors for HPD can generally be divided into two categories [78]. First, the majority of the risk factors relate to *maternal predisposition to develop cardiovascular disease*, including elevated body mass index (BMI), caloric excess, smoking, African American ancestry, high blood pressure, older age, and diabetes. These characteristics warrant close monitoring during pregnancy for development of preeclampsia. Secondly, *pregnancy-specific characteristics* such as nulliparity, excessive placental size, barrier contraception, and multiple gestations are

placental or pregnancy-specific risks of preeclampsia [12]. This framework is closely connected to current theories about the mechanism of preeclampsia. Some argue that the mother's predisposition to cardiovascular disease entails subclinical endothelial dysfunction [72] that can lead to the development of placental lesions and a deficit of angiogenesis during pregnancy. Others identify insufficient trophoblast invasion as inciting reduced placental perfusion that affects maternal cardiovascular health [53]. There may also be a genetic component of preeclampsia risk that is still being investigated [79]. The connection between risk factors and the cause of preeclampsia is still an active area of research. In this thesis specifically, MRI techniques are developed to assess endothelial dysfunction by estimating pulse wave velocity in the maternal arteries and to assess spiral artery function by characterizing placental perfusion distribution.

2.4.3.3 Signs and Symptoms of HPD

Patients with preeclampsia can present with concerning symptoms such as swelling, headaches, right upper abdominal or shoulder pain, and shortness of breath [80]. Physicians typically follow up with blood pressure monitoring and urine analysis. A systolic blood pressure of >140 mmHg (or diastolic blood pressure of 90 mmHg) on two separate occasions at least 4 hours apart after 20 weeks gestation is cause for concern [78]. Elevated protein in the urine that meets a clinical threshold, such as a dipstick reading of 2+, could also meet the criteria for preeclampsia [78].

2.4.3.4 Treatment Options for HPD

As a preventative measure, United States guidelines recommend prescribing low-dose aspirin (81 mg/day) to asymptomatic patients with two or more risk factors for preeclampsia [78, 81]. This was based on clinical studies that showed that 60-150 mg/day of aspirin led to a decrease in preeclampsia risk by 24% [81]. For preeclamptic women who have already become symptomatic after 20 weeks, physicians have to make the complex decision of whether to induce preterm labor to control the disease or proceed with expectant management. More advanced tests to aid in this

decision include uric acid testing, fetal ultrasound, and fetal antepartum testing [78]. The specific resources available at the healthcare facility for maternal and neonatal care are also taken into consideration. A gestational hypertensive pregnancy or preeclamptic pregnancy without severe features such as thrombocytopenia, impaired liver function, and pulmonary edema are generally monitored until 37 weeks gestation, after which delivery is recommended. Continued observation can involve weekly laboratory testing and serial ultrasonography. However, if the pregnancy is complicated by severe features or dire events such as placental abruption, then induction of labor is more heavily considered [78].

2.4.3.5 Intrapartum Care of HPD Patients

The two main goals of managing women with preeclampsia during labor and delivery aside from routine prenatal care, are the prevention of seizures and the control of hypertension [78]. For women with preeclampsia and severe features, it is recommended to administer magnesium sulfate to prevent seizures. In addition, these patients should also be prescribed antihypertensive medication—most commonly labetalol, hydralazine, or nifedipine—to prevent congestive heart failure, myocardial ischemia, renal injury or failure, and ischemic or hemorrhagic stroke. Antihypertensive therapy should begin immediately as soon as persistent severe hypertension >160/110 mmHg is detected. Milder cases such as those with gestational hypertension or preeclampsia without severe features should be monitored in case of developing severe features. The mode of delivery should be considered on an individual basis. Induction of labor with vaginal delivery is still possible at later gestational ages. Vaginal delivery is less safe for preeclampsia with severe features which tend to involve low-birth-weight infants. Records show that the rate of cesarean section is 97% at <28 weeks gestation and 65% at 28-32 weeks gestation. Epidural or spinal anesthesia is safe for pain management as long as the patient is hematologically stable [78].

2.4.3.6 Postpartum Care of HPD Patients

After delivery, women with preeclampsia should be continually monitored for symptoms that can be indicative of eclampsia, pulmonary edema, or stroke. Non-steroidal anti-inflammatory drugs (NSAIDs) that are used for pain management can exacerbate vasoconstriction, swelling, and sympathetic nervous system activation, although multiple studies have not shown an increase in blood pressure with NSAID use in patients with preeclampsia [82, 83]. Women with preeclampsia are at double the risk of CVD and five times the risk of hypertension in later years [84]. This can probably be explained by the shared mechanism of endothelial dysfunction in both atherosclerosis and preeclampsia [78]. It is still unclear if preeclampsia leads to cardiovascular disease or rather that pregnancy uncovers underlying preexisting risk of cardiovascular disease that manifests as preeclampsia. Whatever the case may be, women are advised to make lifestyle modifications (diet, exercise, weight management) to control risk factors for cardiovascular disease and to obtain routine primary care examinations. They should also be made aware that they are at an increased risk of developing preeclampsia again in a future pregnancy.

There may also be life-long consequences of preeclampsia for the infant. Studies have shown that infants born from hypertensive pregnancies have a higher risk of low birth weight compared to normotensive pregnancies [76, 85]. The risk of perinatal mortality is also higher for preeclamptic pregnancies compared to normotensive pregnancies with largest causes being placental insufficiency, placental abruption, and prematurity [12]. A meta-analysis on cardiovascular risk factors of children born from preeclampsia report that they have 0.6 kg/m^2 higher BMI, 2.5 mmHg higher systolic and 1.4 mmHg higher diastolic blood pressures [86].

2.4.4 Ongoing investigations in basic science, treatment, and technological assessment of HPD

Investigations using molecular assays [87] and animal models [88] continue to mine for the cause of HPD. However, identifying the mechanism of this disease is not only important for driving clinical trials exploring a wide array of pharmacological treatments [13, 89, 90], but is also critical to improving tools used by obstetrician-gynecologists for efficiently identifying patients who are at highest risk and would benefit from those treatments. The next section introduces the non-invasive technologies (ultrasound and magnetic resonance imaging) that were investigated in this dissertation for potential in improving the understanding of HPD pathophysiology and clinical risk stratification.

CHAPTER 3: NON-INVASIVE TECHNOLOGIES TO ASSESS CARDIOVASCULAR DISEASE

In this chapter, an overview of Doppler ultrasound, flow and perfusion magnetic resonance imaging (MRI) is presented. These technologies have been well-explored in various cardiovascular disease and continue to be of interest in clinical obstetrics and obstetrics research. This summary is designed to provide the foundational physical and engineering principles of the research presented in Chapters 4-7.

3.1 Principles of Doppler ultrasound

3.1.1 Signal generation

Ultrasonography operates based on the principle that high frequency (2-15 MHz) sound waves travel through the human body as mechanical vibrations. These sound waves are generated by piezoelectric crystals in the ultrasound probe, also called a transducer. The speed of sound, *c*, varies based on the type of medium it travels in. It is about 1.45 mm/μs in fat, 1.58 mm/μs in muscle, and 1.57 mm/μs in blood. The average *c* is said to be 1.54 mm/μs [91]. The wavelength, λ, of the sound wave travelling through tissue depends on the frequency, *f*, of the sound pulses generated by the transducer according to the relationship $\lambda = c/f$. The longer the wavelength, the greater the penetration into the body but the lower the spatial resolution of the image. Conversely, shorter wavelengths help produce high resolution images but with shallower penetration.

The energy delivered to the tissue by ultrasound imaging can be described by amplitude, power, and intensity. Amplitude (P) is the amount of increase and decrease in mechanical vibration pressure, described in units of Pa. Intensity (I) describes the amount of energy per unit area, expressed in units of mW/cm^2. Power is the overall energy transfer and is measured in W. Power

and intensity decrease as sound waves travel deeper into tissue. The amount of energy delivered is important in obstetric US safety considerations. Some of the ultrasound energy can be absorbed by the tissue which results in heating so the instrument display also includes a thermal index (TI) estimating the rise in temperature based on time-averaged acoustic power/intensity, sound beam properties, and tissue properties. Obstetric guidelines state that temperature rise of less than 1.5 degrees Celsius is unlikely to harm the mother and fetus [92, 93]. However, pulsed Doppler ultrasound does deposit more power than standard B-mode scanning so it is typically reserved for second and third trimester exams (see Section 3.1.6). Another concern of ultrasound is that high amplitude pressure waves can potentially cause *cavitation*, the collapse of nearby gas bubbles, instrument manufacturers include a mechanical index (MI) to alert the sonographer to the amount of cavitation risk. However, in obstetrics cavitation is rarely a concern because the pregnant uterus does not contain significant gas bodies [92, 93]. The American Institute of Ultrasound in Medicine (AIUM) recommends that sonographers use energy levels that are “as low as reasonably achievable” (ALARA principle) to minimize risk of tissue damage [94].

US intensity decreases as the waves travel deeper into tissue. Some of the energy becomes absorbed as previously described, and the rest can become reflected or scattered. Different tissues have different acoustic properties, called acoustic impedances. Tissues of different acoustic impedances positioned next to each other form an interface off of which US waves reflect. The echo that forms at the interface is based on the acoustic impedances of the tissues. This is quantified by the amplitude reflection coefficient $R=(Z_2-Z_1)/(Z_2+Z_1)$, where Z_1 and Z_2 are the acoustic impedances of tissues 1 and 2, respectively. A common example is the visibility of the smooth blood vessel wall seen in US imaging because of the reflection of US waves at the interface between the vessel wall and the blood pool separating two distinct acoustic impedances (high R). Some tissues have rough surfaces or many small interfaces compared to the US wavelength. These tissues tend to form scattered echoes which propagate in various different directions with relatively homogeneous amplitude. Doppler US, a type of US which measures

blood flow, uses the principle of scattering by transmitting and receiving waves which scatter from the moving red blood cells. The red blood cells have scattering properties because they are very small compared to the Doppler US wavelength [91].

3.1.2 Image formation

The level of detail visible in an image depends on the lateral resolution, axial resolution, and slice thickness. A high frequency ultrasound probe enables high lateral resolution, which requires a small beam in the focal region so that two reflecting objects (artery and tissue, for example) positioned close together can be distinguished on the screen. High frequency ultrasound is also advantageous for improving axial resolution by shortening pulse durations to distinguish between reflectors that are placed closely along the ultrasound beam. Slice thickness, or elevational resolution, describes how well the US instrument can focus on objects perpendicular to the imaging plane. This is typically the worst dimension of resolution in US so it is rarely considered when optimizing obstetric US [91].

The temporal resolution of US determines how quickly changes in moving objects of the body are reflected in the real-time image as the sonographer moves the probe or keeps it stationary. A single frame is composed of multiple beam lines, and each beam line is composed of an echo transmitted and received by a columnar element of the probe. The frame rate is how quickly a frame is formed. Since the time (T) to collect one beam line is T=2D/c, where D=maximum depth and c=speed of sound in tissue, then the time to collect one frame (Tf) is Tf=2DN/c, where N=number of beam lines. The maximum frame rate FR_{max}=1/Tf=c/(2DN). The sonographer can usually control FR_{max} by changing the depth or the number of beam lines. There are typically between 100 to 250 beam lines. The echoes from each element are stored as amplitude over depth (time of pulse arrival). After collection, the echoes undergo a series of signal processing steps. Most common US images are in B-mode format which encodes amplitude of the echoes in

gray scale brightness. The signals are arranged in matrix form for display (e.g. 500x500 pixels^2) [91].

3.1.3 Types of transducers

One of the ways to optimize image quality is the choice of the ultrasound transducer, of which there are several types used clinically. The first is a linear array transducer. It contains 200 or more separate elements arranged side-by-side. 15-20 elements are activated simultaneously to generate an ultrasound wave and receive an echo. After a small temporal delay, the subsequent group of elements is activated. This process is repeated from one end of the transducer to the other. The beam lines are arranged in straight lines, and the resulting image is rectangular. The linear array is often used for peripheral vascular applications, such as imaging vessels of the arm or the neck.

The second type of ultrasound transducer is a curvilinear array. The shape of the curvilinear transducer is convex at the front. The elements inside are arranged similarly to the linear array and each group of elements is activated one at a time, extending from one end to the other. Due to the convex shape the beam lines are arranged in a fanlike fashion and the resulting image is a sector shape. The curvilinear array is useful for imaging deep structures such as in obstetrics looking at the fetus and placenta in the abdominopelvic region.

The third type of ultrasound transducer is a phased array transducer. The distinguishing feature of the phased array transducer is that it contains about 120 rectangular elements side-by-side but all of them are activated at once. The ultrasound beam changes directionality by activating small time delays between the elements; this allows for scanning a large field of view. The phased array transducer is useful for imaging the heart by scanning between the ribs or looking at vessels of the brain through the temporal bone [91].

In obstetrics the transabdominal probe and transvaginal probe are commonly used. The transabdominal probe is a typical example of a curvilinear array which is favored because it has a large penetration depth. This is enabled by a frequency range of 3-5 MHz, but the low frequency generates low spatial resolution. However, in obese pregnant women and in general early pregnancy, the transvaginal probe which is designed to contain a curvilinear array or phased array is more favorable because it can image tissue closer to the surface even with lower penetration depth using higher frequency (5-7.5 MHz) which maintains high spatial resolution [42, 95]. Even though both types of transducers can be used to image the uterine artery and spiral artery, they have limited field of view so only 3-4 cm of the vessel is visible at a time. In fact, sonographers often identify vessels based on the velocity waveform shape while turning on color flow mode because vessel borders are not very clear [96].

3.1.4 Doppler ultrasound

Measurement of blood flow using Doppler US hinges on the *Doppler effect*, a phenomenon describing the relationship between the change in frequency of the optical or acoustic waves transferred from source to detector and the movement of the source or detector. The Doppler effect was first published by Austrian mathematician and physicist Christian Doppler in 1841 [57]. When applied to blood flow, the shift in frequency (f_D) between transmitted frequency (f_0) and reflected frequency (f_R) is defined as $f_D=f_R-f_0=(2\cdot f_0\cdot V\cdot\cos\theta)/c$, where V=blood flow velocity, θ=angle between US beam in the echo direction and flow direction, and c=speed of sound in tissue [91]. While technological advancement has led to several forms of Doppler US, the primary form used clinically is color pulsed wave Doppler in duplex imaging mode with spectral analysis.

In pulsed wave Doppler, the US probe transmits short bursts of signal into the tissue and receives scattered and reflected echoes. The echoes are amplified, divided into two channels,

demodulated, passed through a sample-and-hold circuit, and filtered. The two channels are separated by a 90-degree phase shift to enable detection of flow direction toward and away from the probe [91].

Blood flow is most easily quantified using spectral analysis. Recall that velocity is encoded by frequency shift (f_D). Practically, the received echo signal contains multiple frequencies combined in a complex signal because the typical blood vessel has a non-uniform distribution of velocities (e.g. laminar flow) within a cross section. This is graphically displayed with the y-axis in units of frequency, the x-axis in units of time, and the brightness of each pixel corresponding to the amplitude of the waves of each frequency bin.

Pulsed wave Doppler samples a volume for measurement at a certain depth of the beam, which helps with precision to measure flow in a single vessel when there are multiple vessels in the path of the beam. To find the location of blood flow measurement, the sonographer is typically guided by a combination of grayscale imaging and color flow imaging (duplex imaging). Grayscale imaging, also known as the B-mode, is conventional ultrasonography where the echoes forming the image are based on the acoustic properties of the tissue being captured. Superimposed on this image is a color flow Doppler image, generated by an average of the velocities measured. The brightness of the colors corresponds to velocity with the color blue meaning away from the probe and the color red meaning toward the probe.

A major concern with Doppler US is the potential of aliasing artifacts. Aliasing occurs when the measured velocity exceeds the upper limit set by the instrument. This is manifested by a wraparound of the measured velocity typically from the positive to negative polarity. Consider the time between pulses transmitted, T_d, c=speed of sound in tissue, d=depth, and the pulse repetition frequency, $PRF=1/T_d=c/(2d)$. To mitigate aliasing, it is recommended that the operator increase the PRF which increases the y-axis velocity range or lower the zero-velocity baseline which increases the y-axis limit in one direction. In order to prevent aliasing by modulating the

PRF, it must be set to at least twice the echo frequency shift (f_D). This is called the Nyquist criterion, which when applied to US is governed by the equation $V_{max}=(PRF \cdot c)/(4 \cdot f_0)=c^2/(8 \cdot f_0 \cdot d)$, where Vmax=maximum velocity measurable without aliasing, c=speed of sound in tissue, f0=transmitted frequency, and d=depth of vessel [91].

There are two other forms of Doppler US that, though not used in this study, do have advantages and are therefore included in many clinical instruments. *Continuous wave Doppler* is an operating mode in which the transmitted ultrasound beam is a continuous wave rather than a pulsed wave. It does not localize the measurement to a particular depth of the ultrasound beam to distinguish between multiple vessels in its path, so it is generally used for large vessels such as the aorta. Continuous wave Doppler is also simpler and therefore more available in inexpensive systems [92]. *Power Doppler* is another operating mode which processes the Doppler signal differently from pulsed wave Doppler by displaying the power of the Doppler signal rather than the velocity of moving blood. This means that the power Doppler signal is related to the concentration of red blood cells that are moving and their velocity. The advantage is that it is not susceptible to aliasing, less dependent on the beam angle, and more sensitive to low flow. However, the main limitation is that it does not display the direction of flow [91].

3.1.5 Echocardiography and peripheral vascular ultrasound in general cardiovascular medicine

Ultrasound of the heart, also known as echocardiography, became clinically useful in the 1970s. There were other procedures in place to examine the heart, but they had limitations. For example, physical examination and electrocardiography were not found to be very specific diagnostic tools for heart disease [97]. Also invasive cardiac catheterization, though specific, was dangerous due to its invasiveness. Currently, examining cardiovascular structure, function, and development involves three main modes of ultrasound. The first is M-mode, which displays a one-dimensional

projection of tissue to track its position over time. This allows the sonographer to assess the motion of the myocardial wall, heart valves, and aortic root. The second mode of ultrasound is two-dimensional (2D) imaging, which provides cross-sectional views of the heart to visualize anatomical detail. Echocardiographers developed ways to measure function based on these views, such as calculating ejection fraction and cardiac output based on tracings of the left ventricle in the images. The third type of ultrasound examination is Doppler ultrasound, which allows one to measure the velocity and direction of blood flow. Specifically, color flow mapping has been useful for assessing valvular regurgitation and intracardiac shunting. Also, using Bernoulli's equation, one can estimate pressure gradients across different chambers of the heart, which is related to some cardiac diseases. Doppler ultrasound can also be used to measure the velocity of movement of the tissue, not just blood, such as when looking for asynchrony of myocardial contraction after a heart attack. Echocardiography is usually done transthoracically, but sometimes it is done in transesophageally using an esophageal probe that places the transducer closer to the heart. The basic echocardiography exam involves looking at structures of the heart in four main locations. The first is the parasternal notch, which enables visualization of the long axis of the left atrium, left ventricle, and aorta. A slight tilt would allow one to look at the right atrium, tricuspid valve, right ventricle, and another slight shift would allow one to visualize the pulmonary valve and main pulmonary artery. The probe can be rotated to show the short axis views of some of these chambers. Second, the apical window shows the four chambers of the heart and five chambers when adding the left ventricular outflow tract. Third, the subcostal window is often used for patients who have lung disease or surgery, and provides a good view of the septum, four-chamber views, and vascular connections. Fourth, the suprasternal view shows the aorta and its branching vessels [97].

Vascular ultrasound uses ultrasound to measure the structure and function of arteries and veins. B-mode ultrasound can image the vessel wall of large vessels. Doppler ultrasound helps identify vessels by their characteristic velocity waveforms, and knowing the normal velocity waveform

pattern helps detect potential disease when the waveforms look abnormal [91]. For example, in vasculitis, B-mode ultrasound is useful for measuring the thickness of the vessel wall. The vessel wall typically has three layers, the intima, the media, and the adventitia; in vasculitis, intima-medial thickening is considered a cardiovascular risk factor. So, the ultrasound is able to quickly and non-invasively measure the thickness to assess cardiovascular risk in cases of vasculitis [98]. Another example is any location in the cardiovascular system that has vessel stenosis or occlusion. Spectral Doppler, for example, has been found to be useful for assessing and identifying the stenosis. At the prestenotic region, a key feature is high pulsatility of the velocity waveform. Pulsatility is essentially the amplitude of the velocity waveform. At the location of the stenosis, there is typically high velocity and low pressure in a narrow lumen based on Bernoulli's equation, which explains the conversion of potential energy to kinetic energy by conservation of energy [91]. After the stenosis, there is low flow or undetectable flow. All of these features can be detected with spectral Doppler. Another application of vascular ultrasound is assessing arteriovenous fistula (AVF) surgery maturation for hemodialysis patients. In this case, ultrasound in its various modes, B-mode or Doppler, can be used to measure flow rate, diameter, and depth of the new AVF to ensure that it has matured well enough to be a dialysis access site. Vascular ultrasound is also useful for aortic disease patients. One example is aortic dissection repair surgery, which can sometimes cause small leaks. In this case, contrast can be injected in conjunction with vascular ultrasound to increase sensitivity for detecting small leaks. After organ transplants, vascular ultrasound can be used to make sure that blood supply and drainage is adequate to the newly placed organ [98]. Vascular ultrasound can also be used to image venous vessels. One common form of venous disease is venous thromboembolism, in which patients with deep vein thrombosis can be at high risk of developing pulmonary embolism. Pregnant women are also at risk of deep vein thrombosis. A thrombus that has formed either in the arm or the leg can break off, or embolize, and clog the arteries leading to the lungs which can be fatal. A common diagnostic procedure is for the sonographer to apply pressure to the femoral vein using

the probe in B-mode ultrasound and measuring the diameter of the vessel to assess its compressibility [99]. In coronary artery disease, intravascular ultrasound has been found to be useful for evaluating atherosclerotic plaque development [100-102].

3.1.6 Basic ultrasound in obstetrics

The standard obstetrical ultrasound exam, according to clinical guidelines (ACR-ACOG-AIUM-SRU Practice Parameter for the Performance of Obstetrical Ultrasound), is divided into the first trimester examination and a second/third trimester examination [103].

In the first trimester, the sonographer looks for the presence of a gestational sac. It is a collection of amniotic fluid and should contain a yolk sac and embryo. This confirms the presence of an intrauterine pregnancy. If the embryo is present, the crown-rump length is measured using ultrasound calipers and is used to estimate the gestational age. The cardiac motion is evaluated using M-mode ultrasound or a 2D video clip, rather than using Doppler ultrasound, to minimize ultrasound exposure to the growing embryo. The number of fetuses is counted; if there are twins, amnionicity and chorionicity are determined. The fetal anatomy, if visible, is evaluated for presence of the bladder, the umbilical cord insertion, and the extremities. To test for possible aneuploidy in the fetus, nuchal translucency thickness is measured. Sometimes Doppler ultrasound may be used to measure ductus venosus velocity [104]. The presence of reversal of the A wave suggests possible cardiac compromise associated with aneuploidy. The sonographer also looks for uterine and ovarian lesions such as fibroids, and uterine anomalies that may impact the success of the pregnancy. To ensure fetal safety, sonographers are advised to monitor the thermal index of the ultrasound machine, which shows how much thermal energy is absorbed by the tissues. Since bone tends to absorb more thermal energy than soft tissue, soft tissue thermal index is used up to 10 weeks gestation and switched to bone thermal index after 10 weeks gestation when bone has started growing in the fetus [103, 104].

In the second and third trimester standard ultrasound exam, the amniotic fluid volume is measured for possible presence of oligohydramnios (low amniotic fluid), which can lead to fetal anomalies, or polyhydramnios (too much amniotic fluid), which can lead to placental abruption and premature birth. The placenta location is evaluated for possible placenta previa. Also, the umbilical vessel number is counted and assessed for location of insertion both in the placenta and the fetus. The gestational age of the fetus is best measured by crown-rump length in the first trimester, but if the crown-rump length was not found to be accurate, the gestational age can also be estimated by using measurements of fetal anatomy. This includes the biparietal diameter, head circumference, femoral length, and abdominal circumference. These measurements can also be used to estimate the fetal weight, which is important for evaluating the possibility of fetal growth restriction. Hadlock et al have published models that translate the anatomical measurements to fetal weight [64, 105].

In the second/third trimester, the umbilical artery pulsatility index can also be measured using Doppler ultrasound to assess for fetal growth restriction [104]. Like in the first trimester, the sonographer again examines uterine and ovarian anatomy to look for the progression of lesions, such as fibroids that could impact the health of the pregnancy [103]. The sonographer also assesses fetal anatomy, particularly the brain and the heart. In the brain, middle cerebral artery velocity is measured by Doppler ultrasound to assess for possible fetal anemia [104]. The cerebroplacental ratio is calculated by the middle cerebral artery pulsatility index divided by the umbilical vein pulsatility index. If the cerebroplacental ratio is too low, this is a sign of brain sparing from physiological distress. Cardiac function is assessed by measuring umbilical vein pulsatility for possible high pressure in the right ventricle in the fetus. Another sign of cardiac compromise is reversal of the A wave in the ductus venosus velocity waveform measured by Doppler ultrasound. The sonographer examines the head, face, neck, stomach, bladder, umbilical cord insertion, spine, extremities, and sex of the fetus during the second and third trimester [103]. Sometimes the uterine artery is measured with Doppler ultrasound to assess risk for

preeclampsia and fetal growth restriction. Uterine artery assessment will be discussed in Chapters 5 and 6 in more detail. In many clinics, Doppler ultrasound of uteroplacental and fetoplacental vessels are reserved for research but are mentioned here to demonstrate how they can enhance the standard obstetrical exam.

3.2 Principles of flow and perfusion MRI

3.2.1 Signal generation

Magnetic resonance imaging (MRI) is the primary modality explored in this dissertation. MRI is advantageous over ultrasound for patient imaging in that it has high spatial and temporal resolution with large spatial coverage and can generate versatile contrasts to visualize different tissues. It is less operator-dependent than ultrasound because the patient can be consistently positioned on the table, in contrast to ultrasound's variability due to the sonographer's probe orientation. The MRI signal is generated by manipulating the water protons in tissues using magnetic and radiofrequency fields. When outside of a magnetic field water protons are oriented randomly, but once they are put within a magnetic field they align parallel to that magnetic field where half of the protons are pointing in the same direction and half are pointing in the opposite direction. However, slightly more protons align with the main magnetic field (B_0). At the same time, the protons are spinning on their own axes while precessing around the magnetic field direction at a precession Larmor frequency $\omega=\gamma B$, where γ is the gyromagnetic ratio (42.58 MHz/T) and B is the magnetic field strength (e.g. 1.5T). The collection of protons is called the net magnetization vector. By convention, the MRI coordinate system refers to the net magnetization vector as pointing in the positive direction of the z axis (direction of B_0) at equilibrium. The B_0 field is generated by running a current through a large spiral of wire, which generates a magnetic field based on Maxwell's Law.

To generate a signal, a radiofrequency (RF) pulse matching the Larmor frequency rotates the net magnetization vector towards the x-y plane. After the RF energy is turned off, the net magnetization begins to relax back to its equilibrium state in two independent but simultaneous processes. Longitudinal relaxation occurs when the net magnetization vector returns to positive z orientation. Transverse relaxation occurs when the protons begin to dephase or spread out until the net transverse magnetization vector eventually cancels out to zero. Imaging contrast in MRI is based on tissue-specific properties that describe how the protons interact in the presence of perturbations in the magnetic field. T1 describes how quickly the net magnetization reaches equilibrium parallel to B_0 (longitudinal magnetization). T2 describes how quickly the net magnetization decays along the axis parallel to B_1 (transverse magnetization). T1 and T2 are completely independent of one another but T1 ≥ T2. The RF pulse can be designed to rotate the net magnetization vector at any angle away from +z. The maximum signal is obtained with a 90º pulse which flips the vector to the x-y plane. The magnetic flux of the excited protons induces a current called a free induction decay (FID) into a receive coil based on Faraday's law. The signal has real and imaginary components and is amplified, digitized, and processed.

3.2.2 Spatial encoding and image formation

Spatial encoding is required to distinguish between the different tissue regions of the patient. This is enabled by gradient coils which form magnetic field gradients in the scanner. In order to select a slice and control its thickness a gradient magnetic field is applied in the z direction during the excitation RF pulse. The gradient amplitude and duration as well as RF properties such as bandwidth, can be used to adjust the slice thickness and position. In the x-y plane, the x gradient and y gradient cause the protons in the patient to have varying frequencies and phase. The signal of each location is denoted by the equation $s(k_x, k_y) = \iint \rho(x, y) e^{2\pi i(k_x x + k_y y)} dxdy$, where s is the signal and ρ is the object. Since the signal from each location is denoted by a particular

frequency and phase offset, the coordinates of the grid are marked by spatial frequency as 1/distance. This coordinate system is called k-space. To reconstruct the image back into object space, there are various ways to sample k-space with a Cartesian grid being one of the most common. The spatial resolution is determined by the extent of the grid denoted by k_x^{max} and k_y^{max}.

The field of view is determined by the interval between the samples denoted by Δk_x and Δk_y. The

MRI scanner is often known as a Fourier transform mechanism by encoding the signal in k-space. Therefore, reconstructing the image of the object from k-space requires the inverse Fourier transform. An important consideration when sampling in k-space is the satisfying the Nyquist sampling criterion. The readout gradient has a particular sampling frequency that must be at least two times the maximum spatial frequency in order to avoid aliasing artifacts.

3.2.3 Flow and perfusion MRI

The three cardiovascular MRI techniques discussed in this dissertation are arterial spin labeling (Chapter 4), 2D phase contrast/4D flow (Chapters 5 and 6), and time-of-flight angiography (Chapter 7).

3.2.3.1 Arterial spin labeling (ASL) MRI

Perfusion is the rate of blood flow into a tissue. In MRI intravenous gadolinium contrast is often used as an exogenous tracer to estimate blood flow into organs such as the brain. However, there are potential risks to administering gadolinium in pregnancy. Arterial spin labeling (ASL) MRI has been a technique of interest for imaging perfusion in pregnancy because it does not require exogenous contrast. Instead, blood water is used as an endogenous tracer by applying RF pulses to invert the net magnetization of blood before it travels through the arteries to the organ. Since the magnetization relaxes after the RF pulse, the perfusion-related signal decays

according to the T1 of blood, which is about 1-2 seconds. The amount of signal also depends on the volume of blood that is labeled using the RF pulses.

The basic framework of ASL involves the acquisition of two types of images. The label image is created when blood is inverted and after a duration of time (post-label delay) while blood enters the tissue, a readout module collects an image of the perfused organ. The control image is created without any RF inversion but the same readout module collects an image of the organ. The perfusion-weighted image is generated by subtraction of the label and control images. Theoretically, the difference between the two images is the labeled blood which reflects perfusion. However, in general the control-label difference is about 1% of the control image signal so a series of alternating label and control images are acquired and averaged to enhance the signal-to-noise ratio.

There are several types of labeling in ASL, but the one used in this dissertation is called pulsed arterial spin labeling (PASL). The key feature of PASL is that a single RF inversion pulse is applied to a large region of blood when acquiring the label image. Flow-sensitive Alternating Inversion Recovery (FAIR) ASL is a specific type of PASL in which a non-selective inversion pulse inverts all of the signal in the entire region covered by the RF coil to generate the control image, while the inversion pulse is only applied to the imaging slab to generate label image [106]. The disadvantage of FAIR is that different spins have different transit times reducing the precision of perfusion measurement. It is also difficult to localize where the blood is coming from. However, FAIR ASL is relatively easy to implement compared to other labeling techniques. In the placenta specifically, the non-selective inversion of FAIR ASL is able to tag both the ovarian arterial supply and the uterine arterial supply (Fig. 13).

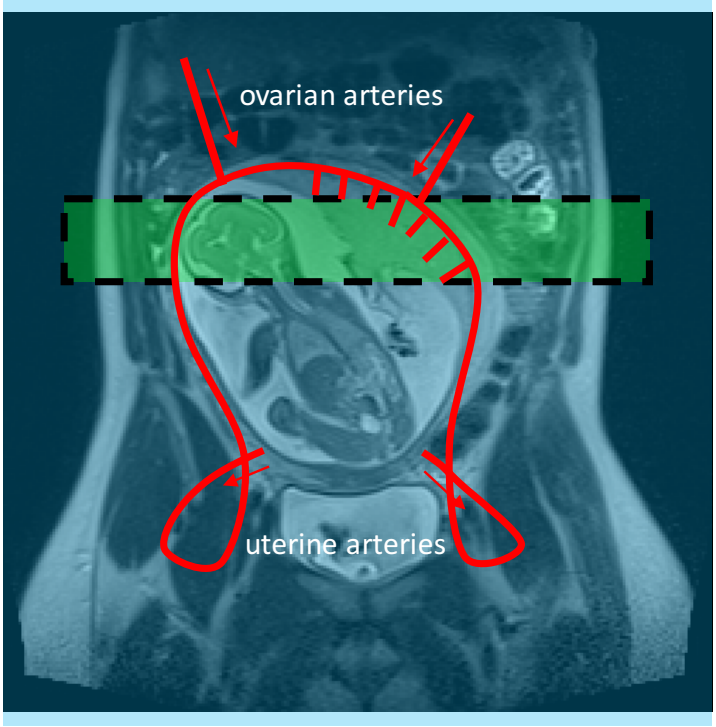

Figure 13 This diagram shows how FAIR ASL can be applied to the placenta. The green box shows the imaging slab and the entire blue translucent overlay shows the extent of the non-selective inversion pulse. The placenta has a dual arterial blood supply, ovarian and uterine arteries, which are covered by the non-selective inversion pulse.

The actual perfusion quantification (mL/min/100 g of tissue) uses a mathematically-derived model such as discussed in Buxton, et. al. [107]. The equation takes into account post-label delay, T1, tissue blood-water partition coefficient, and other effects. A common challenge in ASL MRI is unwanted signal from stationary tissue causing errors in perfusion estimation. To address this issue, background suppression is applied before labelling to reduce signal from stationary tissue. Background suppression uses inversion pulses at specific times for the purpose of inverting and allowing stationary tissue to become nulled or appearing as zero so as to not contribute to the perfusion-weighted image.

3.2.3.2 2D phase contrast (PC) and 4D flow MRI

Phase contrast (PC) MRI measures signal phase to distinguish static from moving spins. The main feature of the PC MRI pulse sequence is the addition of bipolar velocity-encoding gradients positioned along the direction of the blood vessel. Mathematically, the phase produced by a gradient is defined as $\varphi(\tau) = \gamma \int_0^\tau G(t)\, x(t) dt$, where $\gamma = 42.58\ MHz/T$ is the gyromagnetic ratio (constant), τ = duration of gradient, $G(\tau)$ = gradient amplitude, and $x(\tau)$ = position of the spin [108]. This equation can be rewritten using the Taylor expansion to get $\varphi(\tau) = \gamma \int_0^\tau G(t) \left(x_0 + v_0 t + \frac{1}{2} a_0 t^2 + \cdots\right) dt = \gamma \left(m_0(\tau) x_0 + m_1(\tau) v_0 + \frac{1}{2} m_2(\tau) a_0 + \cdots\right)$. By representing $x(t)$ in terms of initial position x_0, velocity v_0, acceleration a_0, etc., m_n becomes the nth gradient moment with respect to these nth order terms [108].

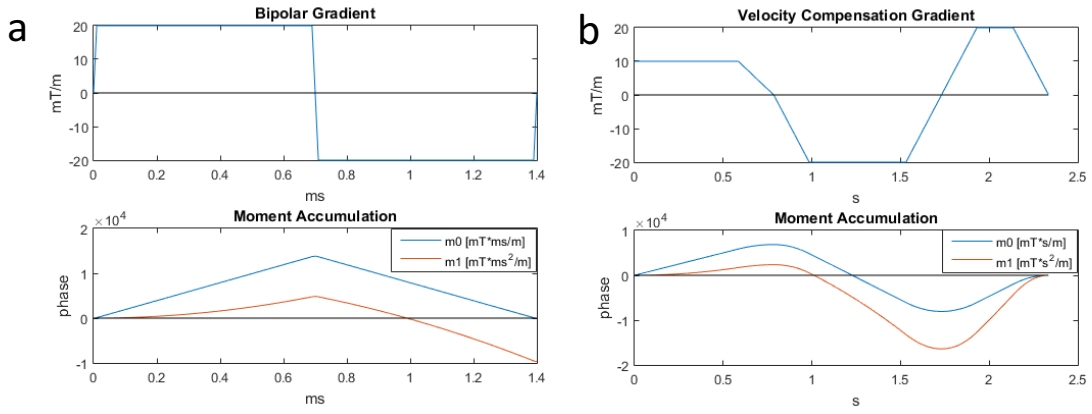

Figure 14 Modeling of a) bipolar gradients with only m0 nulling but m1 phase accumulation, b) velocity compensation gradients with both m0 and m1 nulling

Figure 14a (top) is a demonstration of the bipolar gradients. From τ = 0 to 1.4 ms is a pair of identical gradients with opposite polarity. When the spins are not moving, v_0, a_0, and other higher

order terms are 0. Figure 14a (bottom) shows that the zeroth moment m_0 increases and decreases linearly as the bipolar gradients are played. This is because the m_0 is the area of the gradient and the bipolar gradient areas cancel each other. This demonstrates that regardless of whether the spins are stationary or moving, they experience a linear phase accumulation until τ = 0.65 ms and complete reverse their phase from τ = 0.65 to 1.4 ms because $\varphi(\tau) = \gamma m_0(\tau) x_0$ and $m_0(\tau) = 0$ at the end of the bipolar gradients.

However, the bipolar gradients are not able to recover their first moment m_1, which is the area of the gradient multiplied by the time duration that the gradient is turned on, i.e. $m_1 = m_0 * \tau$. Assuming that the spins are moving at a constant velocity so that a_0 and other higher order terms are 0, from Eq. 2 we see that $\varphi(\tau) = \gamma m_1(\tau) v_0$, where this time $m_1(\tau) \neq 0$. If the spins are moving, the bipolar gradients are unable to refocus the spins back into phase, resulting in a residual phase accumulation at the time of the echo. Physically, this can be explained by the moving spins experiencing a progressively higher gradient field strength as they travel through the pipe. This prevents the second gradient from fully recovering the dephasing from the first gradient [108]. PC MRI is not only able to detect moving spins apart from static spins based on the presence of phase accumulation at the end of the bipolar gradients, it is able to use the phase measurement itself to solve for velocity which will be discussed later.

Phase accumulation leads to signal loss in the magnitude image because intravoxel spin dephasing reduces transverse magnetization faster than surrounding static spins. In the phase image, the velocity-dependent phase accumulation leads to misregistration artifacts in the phase encoding direction of the image. If phase accumulation due to flow is undesired, as is the case

when displaying vascular anatomy in angiograms, velocity compensation is necessary [108]. This requires modifying the bipolar gradients to ensure that $m_0(\tau) = m_1(\tau) = 0$. A tri-lobed gradient is typically implemented with some amplitude G from τ =0 to 0.8 s, -2G from t=0.8 s to t=1.7 s and G from t=1.7 s to 2.3 s (Fig. 14b). This ensures that there is zero phase accumulation in the moving spins as well as the static spins.

In 2D PC MRI, a pair of bipolar gradients is played along with velocity compensation gradients in the slice select gradient direction (z). While the bipolar flow encoding gradients cause the signal of the moving spins to accumulate phase, so do the other gradients involved in the sequence including the slice select (z direction), phase encoding (y direction), and readout (x direction) gradients. For this reason, the velocity compensation gradients are necessary to null the phase effects of the other non-flow encoding gradients.

There are additional factors that give rise to signal phase errors, such as those from eddy currents and magnetic field inhomogeneities [108]. By acquiring two consecutive scans while toggling the bipolar gradients, i.e. positive followed by negative gradient in the first scan and negative followed by positive gradient in the second scan, the phase images can be subtracted to eliminate these phase errors which are relatively constant compared to phase changes from moving spins. The phase difference is $\Delta\phi = \gamma \Delta m_1 v$, where $\Delta m_1 = 2m_1$ which is determined from the bipolar gradient design. The factor of 2 shows that subtracting phase images of opposite polarity also increases the dynamic range of the phases which eases the separation of velocities.

A major consideration in deriving velocity from phase measurements is the avoidance of aliasing. This arises from the limited range in which phase can be measured, i.e. from –π to π. In the event that the velocity of a particular region in the image exceeds the value corresponding to φ = π, then the phase will wrap to the negative range. To mitigate this problem, one can tune the

definition of φ = π appropriately for the expected range of velocities to be measured in the image. This parameter is known as the VENC (velocity encoding) and is often measured in cm/sec. Since $VENC = \frac{\pi}{\gamma \Delta m_1} = \frac{\pi}{\gamma G \tau^2}$ [109], this adjusts the strength of the gradient (G) and duration of the gradient (τ). In practice, if one is trying to minimize scan time, the G is maximized before lengthening τ. Although it is often desirable to set the VENC high to ensure the ability to capture a wide range of velocities, increasing the VENC simultaneously decreases the phase signal-to-noise ratio (SNR). SNR of the phase is simply the SNR of the magnitude image weighted by the phase φ.

Flow measured in volume/time (usually mL/min) is calculated as $Q = 60Av$, where A = cross sectional area (cm^2), v = velocity (usually cm/s), and 60 converts seconds to minutes. This means the measurement of velocity by PC MRI combined with the knowledge of the vessel geometry allows the computation of volumetric flow rate. Since the bipolar gradients are implemented on the slice selection axis in the direction of flow, the slice being imaged is a circular cross-sectional plane through the vessel. Ideally, the plane should be oriented perpendicular to the direction of flow but if not, the velocity is $vcos(\beta)$, where β is the orientation of the slice. The thickness of the slice also determines the sensitivity of the velocity approximation to the orientation of the slice.

The inverse Fourier transform of the k-space data collected are complex numbers, so to extract the phase term, one computes the arctangent of the ratio between the imaginary and the real part of each voxel $I(x,y)$: $\phi(x,y) = \arctan\left(\frac{Im(I(x,y))}{Re(I(x,y))}\right)$. Phase difference reconstruction is often described as computing $\Delta\phi$ by subtracting two phase images, but rather than taking the difference of two arctangents, it is more computationally efficient to do this by taking the complex

ratio so the arctangent only needs to be computed once: $\Delta\phi = \frac{I_1}{I_2} = I_1 I_2^* = \arctan\left(\frac{Im(I_1 I_2^*)}{Re(I_1 I_2^*)}\right)$. Once the phase difference image $\Delta\phi$ has been computed, one can extract velocity using the equation $v = \left(\frac{\Delta\phi}{\pi}\right) VENC : -VENC < v < VENC$ and the sign of the phase difference reflects the direction of blood flow. Similar to the concept of the wheels of the car appearing to move backwards in a motion picture, the flow appears to be moving in the wrong direction when $1 < \left|\frac{v}{VENC}\right| < 2, 3 < \left|\frac{v}{VENC}\right| < 4, \ldots$. This is called aliasing, which can be avoided by setting a high VENC or retrospective correction.

Unlike 2D PC MRI, which has one pair of bipolar gradients in the slice-select direction, 4D flow MRI has bipolar gradients in all three gradient directions. There are several ways to encode flow in all three directions. If one were to derive phase contrast imaging as described thus far and extrapolate to encode velocity in three dimensions, six scans would be expected in order to perform three phase image subtractions. This is called the “six-point” method. However, one can obtain a three-component velocity vector with only four scans: reference, bipolar in x and y, bipolar in x and z, and bipolar in y and z [110]. This is more commonly used to save scan time.

While it can be a challenge to parse the complex data from 4D PC MRI, having 3D spatial information, 3D velocity information, and time can be powerful tools for understanding cardiovascular structure and function. The most common approach is to display the three dimensions of flow as velocity vectors with the color or length representing the magnitude. One can also display flow in 3D by tracking each vector as a particle in the form of streamlines. These streamlines have been used to demonstrate qualitative flow patterns such as whether the flow is linear or tortuous.

3.2.3.3 Flow enhancement in time-of-flight (TOF) angiography

To explain TOF MRI blood vessels are treated as a continuous flow of spins at constant velocity through a cylindrical pipe. Assume that a 90-degree pulse is applied followed by a 180-degree pulse that rephases the spins in the transverse plane. If the spins are not moving, they will be able to experience both the 90-degree pulse and the 180-degree pulse so the signal remains high. On the other hand, if the spins are actively flowing through the pipe, they experience the 90-degree pulse but subsequently flow out of the plane of the slab such that they do not experience the 180-degree rephasing pulse. This results in signal loss in the 2D image and appears as a dark spot in the vessel called a flow void. Note that this is a misnomer because it implies the absence of flow when in fact it is the *presence* of flow itself that causes loss of signal [109].

To correct for the flow voids, one can apply a pulse sequence with a train of repeated RF pulses within the slice. The time between each RF pulse is the repetition time (TR). This process repeatedly flips the static spins into the transverse plane before they get a chance to fully recover their longitudinal magnetization signal. In contrast, moving spins upstream have not experienced as many RF pulses, if any, by the time they flow into the slab. Therefore, their signal is higher than that of the surrounding static tissue. If the spins are flowing fast with v*TR > h, where v is the velocity of the spins and h is the thickness of the slab, then a volume of blood from upstream to the slab will completely replace the slice being imaged, maximizing the intensity because these spins have not experienced any RF pulses. However, if the spins move slowly such that v*TR < h, then the upstream blood only partially fills the imaged slice, producing some enhancement but not as high as the fast moving blood. The amount of signal measured also depends on the flip angle of the RF pulse. A 90-degree pulse would immediately saturate all the spins in the first application, but smaller flip angles take more repeats to steady state saturation, making them more sensitive to the varied velocity of moving spins. This phenomenon is known as inflow enhancement used in TOF MRI of blood vessels [109].

3.2.4 Flow and perfusion MRI in general cardiovascular medicine

ASL MRI has been primarily used to study the brain for clinical medicine and research [111]. It has been used to assess acute stroke [112], tumor vascularization [113], and dementia [114]. These conditions have been found to be closely related to perfusion, also known as cerebral blood flow (CBF). ASL has also been used to research human behavior, learning [115], and mood [116], as CBF plays an important role in neural activity. By understanding normal CBF patterns, ASL has also been used to study drug effects on the brain by monitoring comparative CBF changes. 2D PC MRI is a common technique to measure blood flow in any major vessel [117]. Velocimetry of the aorta, superior/inferior vena cava, pulmonary arteries, and other important vessels is useful for measuring function of the cardiovascular system. 2D PC MRI can identify stenosis, characterized by a narrow lumen with abnormally high velocity, or dissection, showing flow in a vessel adjacent to an extra cavity. 4D flow MRI is still mostly used in research settings, evaluating complex flow patterns in disease and post-surgical cases. One example is measuring wall shear stress to monitor progression of atherosclerosis [22]. TOF MRI is used routinely in the clinic to visualize vessel structure of arteries and/or veins for direct assessment or as a scout image for other MRI sequences.

3.2.5 Flow and perfusion MRI in obstetrics

Unlike routine ultrasound screening of pregnancies, MRI is generally reserved for advanced evaluation of high-risk cases in the event of suspected pregnancy complications. The soft tissue contrast, large field of view, and multiplanar capabilities make MRI suitable for assessing placental abnormalities (placental abruption, placental adhesive disorders, etc.), fetal abnormalities, and even maternal conditions unrelated to pregnancy such as tumors [118]. While the MRI protocols vary depending on the conditions being evaluated, localizers, T1/T2-weighted images, and fat-suppressed images are commonly used to visualize anatomy. Advanced MRI

techniques such flow and perfusion used in clinical obstetrics are beyond the scope of this dissertation, but some preceding uteroplacental flow and perfusion research is briefly discussed.

One of the earliest ASL studies on the human placenta was conducted at 0.5T using FAIR ASL which measured an average perfusion rate of 176+/-24 mL/100 mg/min. A later study of FAIR ASL on second trimester pregnancies with small for gestational age (SGA) or appropriate gestational age (AGA) outcomes show that SGA subjects had lower perfusion than AGA subjects [119]. ASL MRI has also been used to study placental perfusion in mice [120, 121] and non-human primates [122]. More recently, innovations in labelling of ASL sequences have been applied to the placenta as well using 3T, such as velocity selective ASL in the PERFOX technique [123] and pseudocontinuous ASL [24].

2D PC MRI has been used to measure uterine artery blood flow in human pregnancy at 1.5T [21] and 3T [124]. It can also be used to measure blood flow in umbilical and fetal vessels. Even though 2D PC MRI is a widely available technique, it is challenging to orient the imaging plane directly perpendicular to the vessel for accurate measurement of velocity within the complex vascular network of the female pelvis. 4D flow MRI has the advantage of allowing retrospective velocity measurement despite a long acquisition time. Recently, it has been used to study uteroplacental vessels in non-human primates [125].

A major concern of MRI in pregnancy is safety. In the general population, the main potential safety hazards of MRI are

1. The main magnetic field can attract metal objects, which can turn into projectiles and place the patient and other personnel at risk.

2. The RF excitation energy can cause heating of tissue.

3. Rapid switching of gradients can cause central and peripheral nerve stimulation.

4. The acoustic noise of the MRI can carry the risk of hearing loss.

Therefore, there has been significant research effort investigating the extent to which pregnant women and developing fetuses may be more vulnerable to these hazards than the typical patient previously considered. The main magnetic field was initially thought to be teratogenic or cause fetal harm but a retrospective study did not find strong evidence of increased adverse fetal health outcomes in those who were exposed to MRI in utero [126]. The RF energy used to excite MRI signals does carry a risk of heating maternal and fetal tissue. The distribution of heat in the body varies according to fetal position, maternal position, and body size and shape. To be conservative, most MRI protocols use a 2 W/kg specific absorption rate (SAR) limit or a temperature increase of 0.5ºC over a duration of 30 minutes [127]. The rapid switching of gradients potentially increasing the risk of central and peripheral nerve stimulation is taken into consideration when scanning any patient, but pregnancy has not been known to carry additional stimulation risk beyond a general subject. The MRI scanner generates loud noises which can cause hearing loss in the mother or fetus. The mother is required to wear ear protection. Fetal hearing is protected by surrounding maternal tissue which can attenuate sound. Typically scanning does not exceed the 90 dB limit set by American Academy of Pediatrics [126]. Like ultrasound, MRI does not generate ionizing radiation and can be a powerful diagnostic tool when the benefits outweigh the risks to the pregnant patient.

CHAPTER 4: SPIRAL ARTERY FUNCTION BY ARTERIAL SPIN LABELING (ASL) MRI

4.1 Abstract

Placental insufficiency has long been known to play a role in the development of HPD but the exact physiological nature of spiral artery dysfunction is an area of active research. In this study, Flow-sensitive Alternating Inversion Recovery (FAIR) ASL MRI was adopted and tested on human pregnancy subjects in the second and third trimester to optimize the technique and explore signal processing strategies that would benefit clinical understanding of HPD. 19 subjects in the second and third trimester were imaged with FAIR ASL MRI at 1.5 T and measured placental perfusion was 36.6, 76.4, and 118.9 mL/100g/min using manual, suprathreshold, and Bonferroni-corrected ROIs. An alternative pattern analysis approach was tested on a subset of six subjects. This showed that by taking a Bayesian approach with an alternate coordinate transformation and thresholding of the blood flow clusters, gestational hypertensive subjects seemed to have larger variation in total area and percent area than normotensive subjects. This may result from more motion or more intermittent flow in the abnormal pregnancies. The evidence provided by this study may serve as a foundation for future investigation in developing ASL MRI to evaluate the perfusion dynamics of the placenta.

4.2 Introduction

Placental histopathology suggest that insufficient placental perfusion may be strongly associated with HPD based on placental histopathology [128] because HPD often manifests as maternal stromal-vascular lesions such as accelerated villous maturation and intervillous fibrin deposition resulting from abnormal spiral artery flow in maternal vascular malperfusion. While the underlying etiology of this pathology is still being investigated, researchers speculate a combination of

genetic, environmental, and cellular processes (e.g. insufficient trophoblast invasion of the spiral arteries) contribute to maternal vascular malperfusion [13, 128]. In addition, data-driven mathematical modeling of blood flow in the spiral arteries and intervillous space have described damaging high-pressure, turbulent blood flow jets and high wall shear stress entering the intervillous space from poorly-modeled spiral arteries [53, 129]. These physiological studies highlight the potential of *in vivo* hemodynamic assessment of placental function to improve researchers' understanding of disease progression in HPD.

Measuring spiral artery flow in human pregnancy has been challenging. Recent studies have reported initial feasibility by Doppler ultrasound [130, 131], but they acknowledge that this is a localized measurement so the sensitivity is too low to predict HPD. Therefore, the primary method of measuring uteroplacental blood flow remains uterine artery Doppler ultrasound as a surrogate for spiral artery function. Arterial spin labeling (ASL) MRI is a promising technique for measuring placental blood flow in pregnant women because it is non-invasive, quantitative (mL/min/g tissue), and does not require a contrast agent. While clinical MRI does not have the spatial resolution to image individual spiral arteries, it has the potential to supersede ultrasound by imaging perfusion dynamics and other functional aspects as such diffusion and oxygenation of the whole placenta. Prior ASL MRI research in humans have used Flow-sensitive Alternating Inversion Recovery (FAIR) without background suppression at 0.5T [23], at 1.5T [119], pseudocontinuous labeling (pCASL) at 3T [24], or acquired simultaneously with oximetry [123].

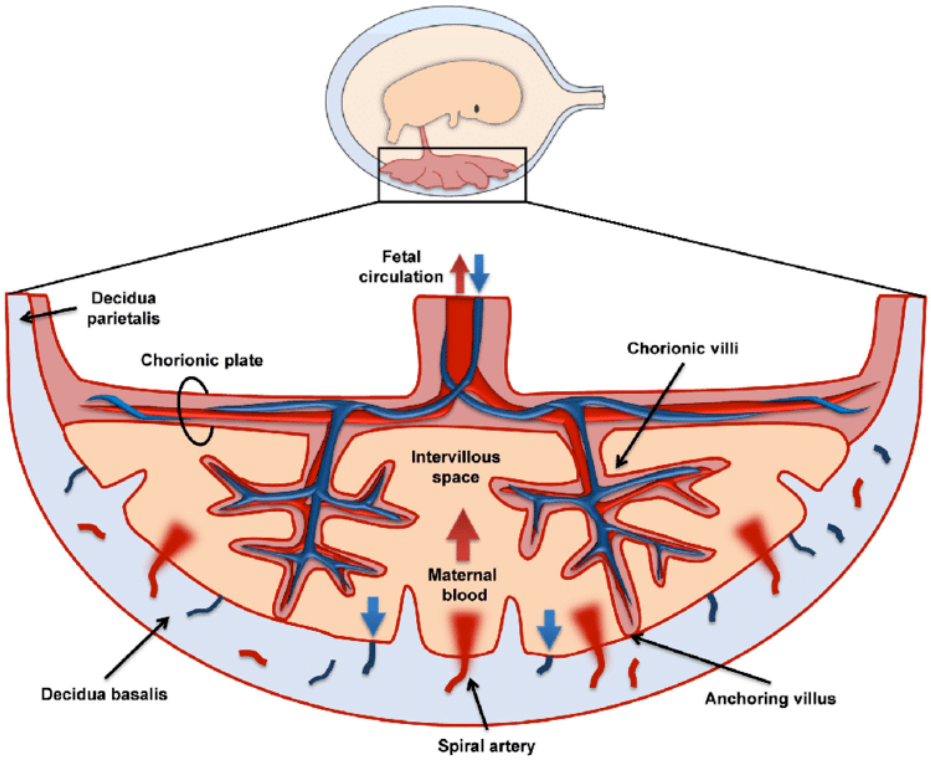

Figure 15 Diagram of placental anatomy showing blood sources and destinations around the intervillous space, an open pool of blood [11].

However, there are significant challenges to placental ASL, including: 1) vulnerability to motion artifacts and 2) lack of an appropriate perfusion model specific to the placenta. Motion can come from maternal breathing, fetal motion, and uterine contractions. In addition, prior studies rely on mathematical models of perfusion that were originally developed for organs with arterial-capillary-venous circulations such as the brain and kidney. In contrast, the placenta is unique anatomically and physiologically in that it consists of arterial blood flowing into an open space called the intervillous space that can be as large as 3 cm in diameter. The blood bathes the fetal capillaries before returning through the venous system (Fig. 15). This has led to innovations accommodating this unique physiology. For example, it is believed that measuring blood movement in a variety of directions, rather than in a single direction as in a capillary bed, is a critical part of the placental

blood flow pattern [132]. These challenges were also addressed in the following ASL MRI feasibility and pattern analysis studies I conducted.

First, feasibility of FAIR ASL at 1.5T was tested in pregnant human subjects, using background suppression to reduce physiological noise. The advantage of FAIR ASL is that it is relatively easy to acquire images from complex anatomy such as the placenta and surrounding vessels. 1.5T MRI systems are more widely available and more commonly approved for imaging pregnant women than 3T MRI, despite having considerably lower sensitivity for detecting ASL effects. This study was presented as an abstract at ISMRM 2018 [133].

Second, an image processing approach of placental ASL images was developed to characterize placental blood flow distribution without assuming the traditional perfusion model. Instead, the control and label signals were considered as separate normal distributions with the same standard deviation as a measure of temporal signal dynamics during the time of image acquisition. An alternate coordinate space was developed with meaningful spatial descriptors that would improve characterization of blood flow distribution from the maternal to fetal side of the placenta. This study was presented as an abstract at ISMRM 2019 [134].

4.3 Methods

4.3.1 Feasibility of 1.5T FAIR ASL MRI in human pregnancy to measure placental perfusion

19 healthy singleton pregnancies (GA range=17-38 weeks) were imaged to characterize normal placental perfusion at 1.5T. HASTE localizer images were acquired in four axial slice positions through the placenta, followed by free-breathing FAIR ASL in the same region with a 2D EPI readout (4 slices, 12.5 mm gap, GRAPPA rate=2, matrix=64x64, target voxel size=4x4x10 mm^3). A background suppression (BS) scheme was optimized to suppress the static tissue signal with

T1s between 650 and 4000 ms to 10% of its equilibrium value. An M0 scan with no magnetization preparation and identical imaging parameters was also acquired for quantification. BS FAIR ASL was acquired with several inversion times and test-retest reliability was also assessed in a subset of 8 subjects.

Data analysis included motion correction of the ASL images using a nonlinear deformation [135] and compared signal changes in three types of ROI:

1. manual tracing of the placenta based on the M0 image
2. statistical parametric mapping based on temporal correlation with the label/control paradigm thresholded at $p<0.05$ (uncorrected)
3. statistical parametric mapping based on temporal correlation with the label/control paradigm thresholded at $p<0.05$ (Bonferroni corrected for the number of placental voxels)

Placental blood flow was estimated using the traditional Buxton, et al. equation $F = \frac{6000*\Delta M*e^{TI/1.531}}{2*M0*TI}$ [107] with adjustment of M0 for 90% background suppression and using 1.53s for blood T1 at 1.5T in women [136].

4.3.2 Pattern analysis of placental blood flow distribution in ASL MRI of human pregnancy

A method of quantifying uteroplacental blood flow distribution using 2D FAIR ASL MRI was developed and tested in 6 of the 19 singleton pregnant subjects with clinical outcomes listed in Table 1. Rather than define a perfusion model as in traditional approaches of analyzing ASL images, it was assumed that the label and control signals were normally distributed with the same standard deviation. This would enable visualization of the temporal dynamics of the acquired data in a model-free fashion. Then, a Bayesian approach was adopted by drawing 100 samples from

the posterior distribution of the control and label signal difference. The median value from each voxel was extracted and masked based on a statistical threshold to remove inconsistent signals. Figure 16 demonstrates this concept in a representative image showing motion artifacts in the control-label difference from maternal breathing, fetal motion, and uterine contractions (panels a-c) with improvement in image quality in the median image (panel d) after removing motion artifacts.

Subject	Gestational Age (N weeks N days)	Clinical Comments
A	21w6d	Normal
B	32w4d	Normal
C	38w4d	History of tobacco use, IUGR
D	32w6d	Gestational hypertension (diagnosed intrapartum)
E	25w5d	Gestational hypertension (diagnosed intrapartum), IUGR
F	17w0d	Gestational hypertension (diagnosed postpartum)

Table 1 Six pregnant subjects (subset of 19 total) whose data was analyzed using the model-free approach to characterize placental blood flow pattern

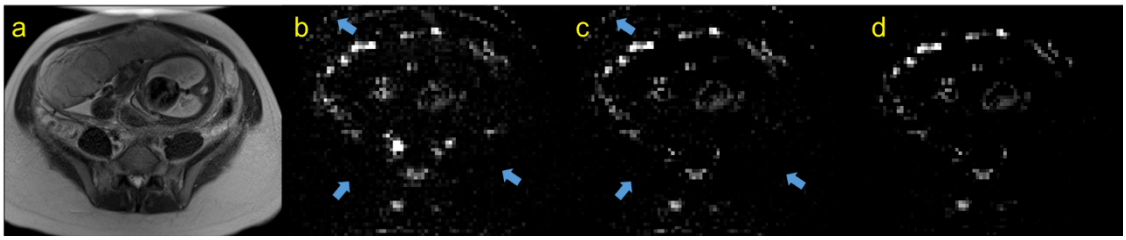

Figure 16 Corresponding HASTE (a) and control-label difference (ΔM) images (b,c,d) at a representative slice position in Subject C: both absolute value |ΔM| (b) and positive ΔM (c) images show noise-like artifactual signal (blue arrows) outside of expected areas of perfusion in the placenta and major maternal arteries. The masked median extracted from 100 samples of the posterior distribution appears to effectively remove artifacts (d).

The advantage of acquiring axial images of the placenta is that this orientation allows for a cross-sectional visualization of arterial blood flow from the maternal to fetal side. To facilitate this analysis, an alternate coordinate system was developed by positioning a spline-based curve along the uteroplacental interface of the placenta and projecting bidirectional rays along this curve. Interpolation was performed along these rays to form a projected image of the ΔM signal in both the individual 100 samples per slice and the corresponding masked median drawn from those samples (Fig. 17b,d).

Since the blood flow signal was distributed in the form of clusters, reminiscent of placental lobules, watershed segmentation was performed and computed various metrics on the clusters to quantify their lobule-like pattern (Fig. 17c). A probability map was generated from the 100 samples that depicted uncertainty based on temporal signal stability within each voxel (Fig. 17e) and the distribution of the cluster metrics was reported (Table 2). In the cohort of six subjects, the cluster metrics on a per subject basis were generated and compared.

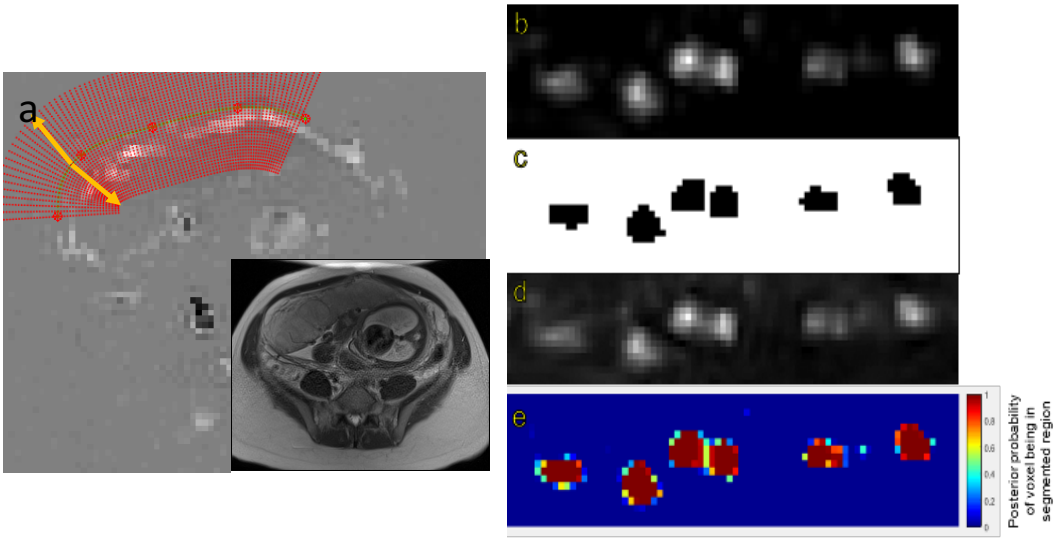

Figure 17 a) Diagram of control points and spline interpolation on a median image with corresponding HASTE image of placenta, b) projection image from masked median image, c) binary watershed threshold segmentation of (b), d) one of the 100 samples of the posterior distribution, e) probability cluster map from 100 samples

Clustering Metrics	Masked median	100 samples median [2.5%,97.5%]
Number of clusters	6	6 [5,7]
Total area of all clusters	145 VU^2	147 [138,156]
Average area across clusters	24.2 VU^2	24.3 [18.4,30.8]
% area of the image containing clusters	9.7%	10.5 [9.8,11.1]
Mean signal in clusters	2034.3 AU	1946.1 [1724.6,2090.3]
Maximum horizontal distance between clusters across columns	11 VU	11 [9,12]

Table 2 Cluster metrics computed from the binary projection images (VU=voxel units, AU=arbitrary units)

4.4 Results

4.4.1 Feasibility of 1.5T FAIR ASL MRI in human pregnancy to measure placental perfusion

Using data from the p<0.05 corrected voxels, ASL signal changes starting at TI=1000 increased with TI in a manner consistent with the increasing signal regime [107] based on an estimated arterial transit time of 700 msec [24] (Fig. 18a). Compared to the other ROIs, the Bonferroni-corrected ROI produced a larger signal (Fig. 18b). When comparing the agreement between two repetitions of the 2000 ms inferior labeling using a more generous P<0.05 uncorrected mask, a considerable but not perfect overlap was found (Fig. 19). Average overlap was 54% and 50% for the p<0.05 corrected and uncorrected maps after excluding two subjects with very poor reproducibility. Estimated placental perfusion results using the three ROI are presented in Table 3.

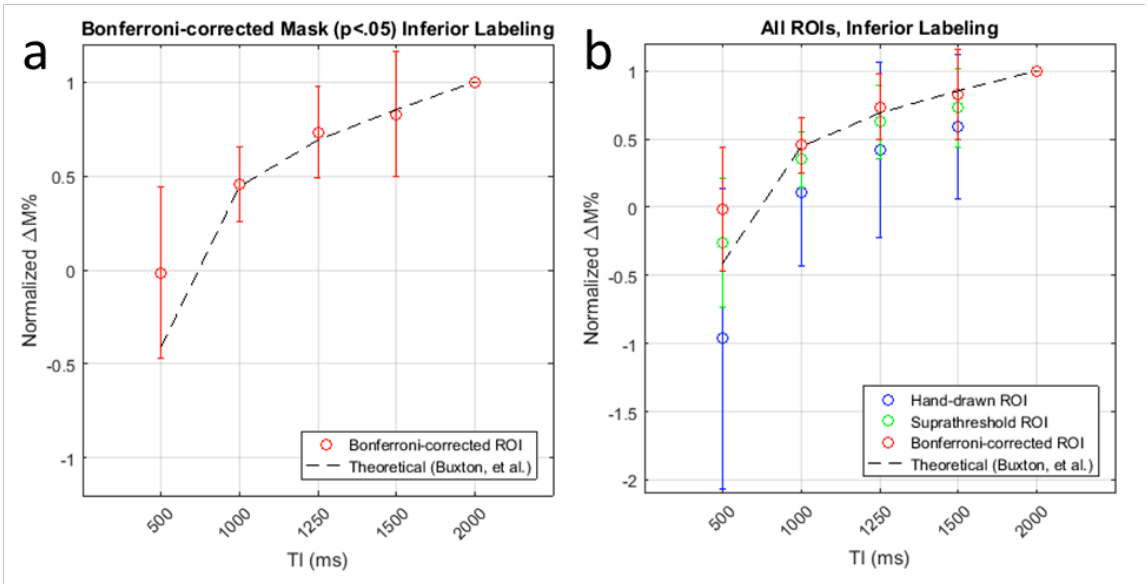

Figure 18 a) Normalized ΔM% versus TI for inferior labeling with the ROI generated from the Bonferroni-corrected threshold set at p<0.05. The predicted signal was based on transit delay Δt=700 ms. It shows that the signal behavior across TIs matches the theory presented in Buxton et al. [107]; b) Comparison of the normalized ΔM% versus TI curves from the hand-drawn ROI, suprathreshold ROI, and the Bonferroni-corrected ROI. It shows that the Bonferroni-corrected ROI produces the largest signal.

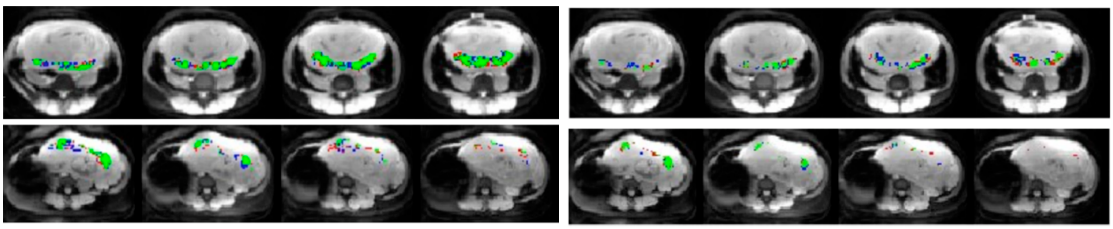

Figure 19 M0 images of posterior placenta (top row) and anterior placenta (bottom row) with ASL ROIs generated using statistical parametric mapping of the ASL time series with the label/control paradigm thresholded at Bonferroni corrected p<0.05 (right) and p<0.05 uncorrected (left). Test-retest maps are shown in red and blue, while overlapping voxels are shown in green.

TI = 2000 ms	PBF (mL/100g/min)
Manual ROI	36.62 ± 18.47
Suprathreshold ROI	76.41 ± 25.32

Bonferroni-corrected ROI	118.93 ± 34.71

Table 3 Comparison of PBF (mL/100 g/min) in three types of ROIs TI=2000ms excluding two subjects with poor reproducibility in perfusion signal based on test-retest analysis

4.4.2 Pattern analysis of placental blood flow distribution in ASL MRI of human pregnancy

In Fig. 20 shows box plots of selected cluster metrics (**Total Area**, **% Area**, and **Mean**). When comparing individuals with no gestational hypertension and those with gestational hypertension, it appears that the latter group demonstrates larger within-subject variability of **Total Area** and **% Area** in the 100 samples of the posterior distribution compared to the former group (Fig. 20a,b). The **Mean** signal of the gestational hypertensive subjects appears to be about the same or slightly lower than the non-hypertensive subjects (Fig. 20c).

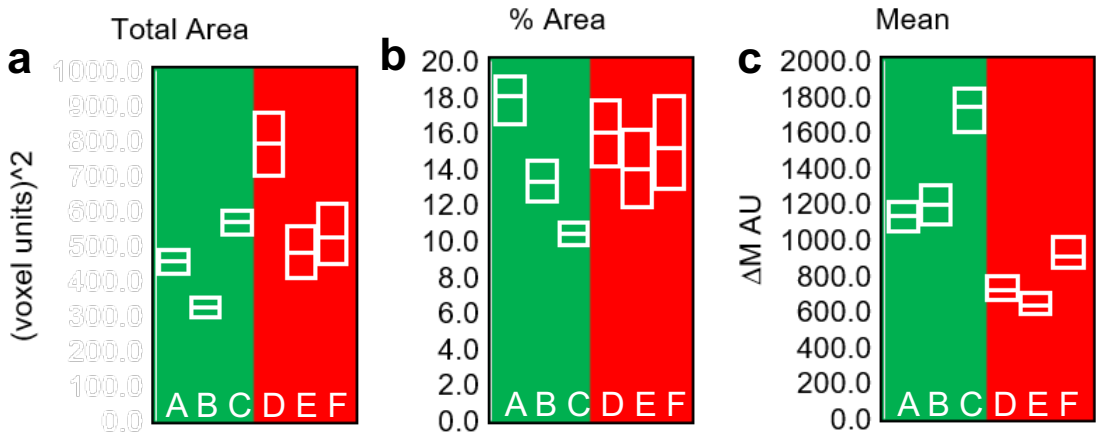

Figure 20 Per subject box plots of 2.5%,50%,97.5% quantiles for select cluster metrics. For Total Area (a) and % Area (b), subjects with gestational hypertension (red) have similar median and larger posterior variances compared to subjects without gestational hypertension (green). For Mean (c), subjects with gestational hypertension appear to have about the same median as or lower than the non-hypertensive subjects.

4.5 Discussion

In these studies, background suppressed 1.5T FAIR ASL was found to be feasible in second and third trimester pregnancies and suitable for pattern analysis to better understand blood flow distribution in the placenta. The control-label difference signal changes yielded a TI dependence consistent with ASL theory and provided reproducible maps of placental blood flow. As expected, placental perfusion was highest in the ROI comprised of the voxels with the most significant label/control effect. Note that placental “perfusion” is not homogeneous, but rather signal changes are localized to discrete regions likely representing the distributions of individual spiral arteries, which deliver blood to chorionic villi. Some of these spiral artery distributions are found to be infarcted in patients with fetal growth retardation [75], and placental ASL provides a potential approach for detecting this pathology in vivo. Placental blood flow values were in the range of previously published values [23, 24], though when averaged across the anatomically defined ROI, values were considerably lower.

An alternative approach of measuring blood flow distribution in the placenta rather than traditional perfusion was shown to be feasible in this ASL dataset. This approach did not assume a perfusion model in characterizing the open circulation of the intervillous space, thus allowing the opportunity for understanding the unique potential blood flow dynamics directly from the data. Initial results showed promise in distinguishing between normotensive and gestational hypertension subjects by showing the second group had a larger within-subject variability in the total area and percent area of blood flow clusters over scan duration. This pattern may be related to more motion or intermittent flow in the abnormal pregnancies. Although a larger subject population would be needed to confirm the clinically relevant differences seen, it is possible based on initial evidence that these patterns can be related to placental lobular morphology and function. For example, placental infarcts may manifest as reduced density of blood flow distribution.

In future work, this ASL acquisition and signal processing method can be improved upon by extending to 3D coverage of the placenta. Simultaneous-Multislice (SMS) and accelerated imaging strategies can be used to greatly increase the slice coverage. Another potential improvement is finer and larger range sampling of TIs, particularly shorter TIs less than 150 ms, to better capture temporal perfusion dynamics.

4.6 Conclusions

These studies demonstrated the feasibility of measuring and quantifying placental blood flow in healthy pregnant subjects in the second and third trimester using background suppressed FAIR ASL at 1.5T. Placental ASL with Bayesian statistics provides an approach for noninvasively mapping and evaluating maternal blood flow pattern in the placenta. Metrics quantifying characteristics of HPD-related placental dysfunction can potentially be clinically relevant biomarkers for assessing risk of adverse pregnancy outcomes.

CHAPTER 5: NON-INVASIVE IMAGING OF THE UTERINE ARTERY DURING HUMAN PREGNANCY WITH UTERINE ARTERY US, 4D FLOW MRI, AND TIME-OF-FLIGHT (TOF) MRI

5.1 Conventional uterine artery assessment by Doppler ultrasound (US)

Clinicians have largely relied on Doppler ultrasound velocimetry of the UtAs as an indirect measure of placental hemodynamics in suspected HPD patients based on the notion that pathologic high resistance to flow in the poorly remodeled spiral arteries would be reflected in the upstream UtAs, particularly after 24 weeks gestation. This approach is feasible because the UtAs are larger (3-5 mm in diameter) than the spiral arteries (~300 μm) and can be reliably localized.

UtA velocity waveforms are commonly measured using a transabdominal probe at the lower uterus near the inguinal ligament. Historically UtA velocity was first measured using continuous wave Doppler [137, 138], but later with the availability of color pulsed wave Doppler the UtA became easier to locate. The key feature for finding the UtA is the crossover between the vessel and the external iliac artery. The sonographer rotates the probe until the characteristic spectral Doppler waveform is found. In nonpregnant and early first trimester subjects, the velocity waveform of the UtA has a sharp systolic peak and a low velocity diastolic phase, called a diastolic notch. By the end of the second trimester, it normally converts to a sharp systolic peak with a steady positive diastolic phase, indicating reduced resistance to flow [92].

When studies began to show that adverse pregnancy outcomes seemed to be correlated with a persistent diastolic notch in late pregnancy, researchers began reporting metrics to identify abnormal UtA waveforms in pregnancy cohorts. Systolic/diastolic ratio, resistance index, and pulsatility index were used to circumvent the need to adjust for the insonation angle, which must

be considered to accurately quantify velocity. Nomograms and statistical thresholds were subsequently developed to categorize patients into low-risk and high-risk categories for HPD [139-141].

5.2 Assessment of the uterine artery structure and hemodynamics by 4D flow and TOF MRI

5.2.1 Abstract

Given the challenges associated with uterine artery Doppler ultrasound, MRI was investigated as an alternative imaging technique for HPD. The purpose of this study was to determine the feasibility of 4D flow MRI in pregnant subjects by characterizing UtA anatomy, computing UtA flow, and comparing UtA velocity, pulsatility and resistivity indices (PI, RI) with transabdominal Doppler US.

In a prospective cross-sectional study from June 6, 2016 to May 2, 2018, non-contrast angiography and 4D flow MRI of the UtA and placenta using 1.5T were performed for forty-one singleton pregnant subjects (age [range]=27.0±5.9 [18-41] years) in their second or third trimester. We additionally scanned three subjects who had pre-pregnancy diabetes or chronic hypertension. UtA anatomy was described based on 4D flow-derived non-contrast angiography, while UtA flow properties were characterized by net flow, systolic/mean/diastolic velocity, PI and RI through examination of 4D flow data. PI and RI are standard hemodynamic parameters routinely reported on Doppler US. Spearman's rank correlation, Wilcoxon signed rank tests, and Bland-Altman plots were used to preliminarily investigate the relationships between flow parameters, gestational age, and Doppler US.

4D flow MRI and UtA flow quantification was feasible in all subjects. There was considerable heterogeneity in UtA geometry in each subject between left and right UtAs and between subjects.

Mean 4D flow-based parameters were: mean bilateral flow rate=605.6±220.5 mL/min, PI=0.72±0.2, and RI=0.47±0.1. Bilateral flow did not change with gestational age. We found that MRI differed from US, showing lower PI (mean difference -0.1) and RI (mean difference <-0.1) with Wilcoxon signed rank test results of p=0.05 and p=0.13, respectively. 4D flow MRI was shown to be a feasible approach for describing UtA anatomy and flow in pregnant subjects.

5.2.2 Introduction

The placenta plays an essential role in supporting the endocrine, nutritional, and oxygenation needs of the growing fetus [54]. During gestation, the maternal uterine arteries (UtA) undergo extensive remodeling, hypertrophy and hyperplasia of vascular smooth muscle, and decreased arterial impedance to match fetal demand for oxygen and nutrients [46]. Arterial dysfunction is characteristic of pregnancy disorders (e.g. preeclampsia and fetal growth restriction) and reduced UtA flow is implicated in reduced birth weight and spontaneous preterm birth [142]. Quantitative parameters that can characterize abnormal UtA remodeling and reduced UtA flow may provide effective screening tools to identify women who have the greatest risk for adverse pregnancy outcomes.

Transabdominal Doppler ultrasound (US) is the primary method used to assess UtA flow but is challenging due to the heterogeneous and tortuous UtA anatomy, location, and dependence of measured velocity on insonation angle [21]. Some of the limitations of US may be addressed with 2D phase contrast MRI [20, 21], but this is also challenged by difficulty planning 2D plane locations, lack of three-dimensional anatomy visualization, and, in the case of unidirectional velocity encoding, dependence of flow direction on the plane angle.

Time-resolved 3D phase contrast imaging (“4D flow”) is an MRI technique that maps all three spatial components of blood and shows 3D arterial morphology and flow dynamics. While we do not anticipate this method to be readily leveraged in standard clinical practice, it may be useful for

research as it enables assessment of blood flow in highly tortuous vessels such as the UtAs, with reduced operator dependence compared to US [22, 143, 144]. Compared to 2D phase contrast MRI, 4D flow requires longer scan times to achieve the spatial coverage and spatial resolution needed to image the UtA. As a result, fetal or maternal respiratory motion may corrupt 4D flow data.

The purpose of this study was to assess the feasibility of obtaining 4D flow MRI data in pregnant subjects. A second objective was to characterize UtA structure and hemodynamics using 4D flow and compare these results to Doppler US.

5.2.3 Methods

5.2.3.1 Study Population

This study was completed on forty-one pregnant subjects (50 originally enrolled) who gave informed consent between June 6, 2016 and May 2, 2018 to be enrolled in this cross-sectional study approved by the HIPAA-compliant Institutional Review Board. Inclusion criteria included singleton gestations at 16 weeks or greater. Exclusion criteria were: (1) morbid obesity (BMI ≥ 35 at the start of the pregnancy), (2) uterine fibroids and major structural fetal anomaly, (3) routine MRI contraindications such as metallic implants/devices and claustrophobia, (4) insufficient MRI image quality, and (5) lack of US scan for comparison. The 9 subjects who underwent MRI and were excluded from analysis are reported in Figure 21, leaving a final count of forty-one females for whom data analysis was completed. Reasons for exclusion from the data analysis were: incorrect setting of maximum velocity encoding threshold (VENC) parameter (n=4), the attending physician was not available for Doppler US (n=5), or one UtA could not be located on either MRI or US but the other UtA remained in the dataset (n=3). Additionally, we scanned and analyzed three subjects with more serious risk factors of adverse pregnancy (one with pre-pregnancy diabetes mellitus and two with chronic hypertension).

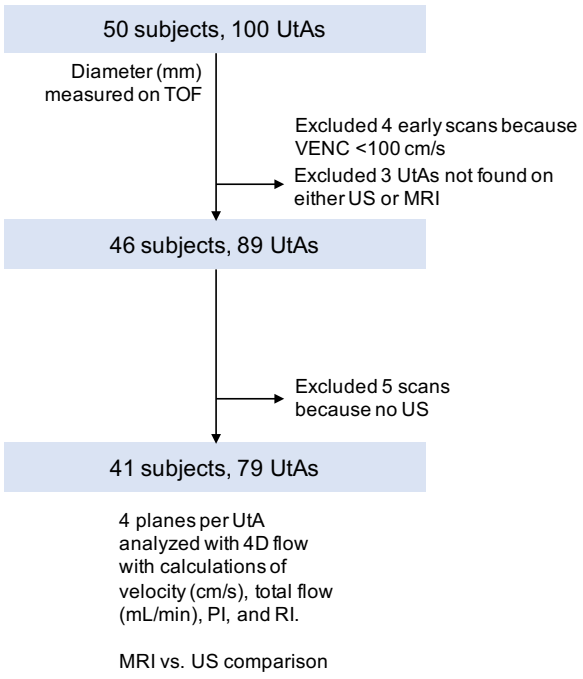

Figure 21 Diagram of exclusion criteria for analysis.

5.2.3.2 Ultrasound

Doppler US was collected and analyzed in forty-one subjects (E10 Voluson; GE Healthcare, Chicago, IL). US measurements of blood flow velocity in the left and right UtAs were acquired using a transabdominal probe. Real-time color velocimetry allowed for identification of the intersection between the uterine and external iliac arteries, and velocity waveforms were recorded according to standard guidelines [96]. Following a standard routine protocol, the angle of insonation between probe and UtA was kept as close to zero as possible, and in all cases <30 degrees. Angle correction was used when a zero angle was not obtainable. MRI-compatible fiducials were adhered to each side of the surface of the abdomen bilaterally where the US probe had been located for identification of spatial correspondence on subsequent MRI.

5.2.3.3 Magnetic Resonance Imaging

MRI was performed at 1.5T (Avanto; Siemens Healthcare, Erlangen, Germany) with a 12-channel spine array and 4-channel body array coil. 37 subjects were in supine position and 4 subjects were in left lateral decubitus position based on their individual comfort level. 3-lead ECG leads were used for cardiac-gated acquisitions. Anatomical localization of the abdomen and placenta was obtained with a half-Fourier acquisition stimulated echo (HASTE) sequence.

An ECG-gated 2D multislice axial time-of-flight (TOF) angiogram was acquired, including the bifurcation of the descending aorta and the top of the femoral heads of the thigh bones based on the HASTE images to ensure coverage of the UtAs near the internal uterine orifice (Figure 22). The imaging parameters are listed in Table 4. Details of TOF parameter optimization are provided in Figure 23.

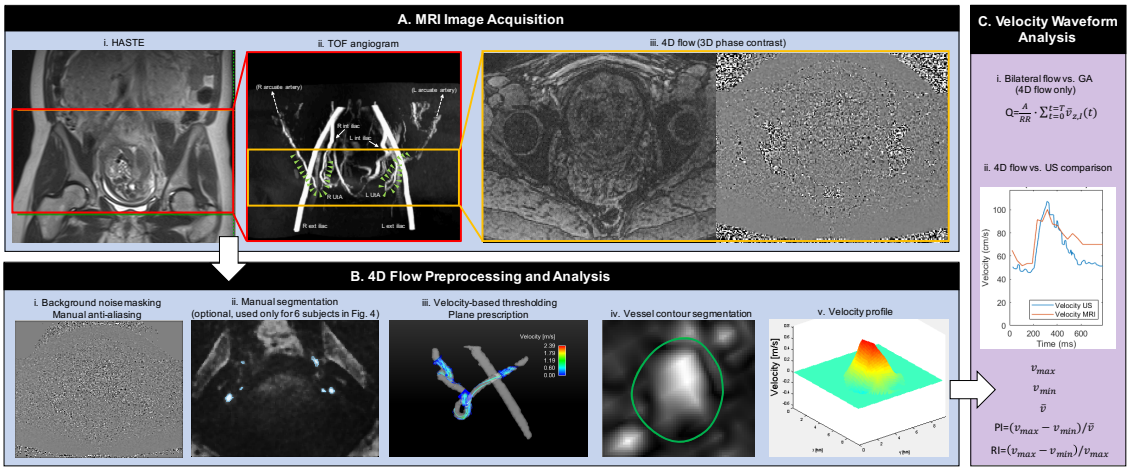

Figure 22 Methodology workflow. A, MRI Image Acquisition. The TOF scan (A.ii) was planned from a HASTE localizer (A.i). The 4D flow scan (A.iii) was positioned at the UtA hairpin using the TOF scan as a reference. The overall scan time was 30-40 minutes. B, 4D Flow Preprocessing and Analysis. The 4D flow analysis included phase difference image noise filtering and, if needed, manual anti-aliasing (B.i). For improved visualization in the subjects in Fig. 25, optional manual segmentation of UtA from 4D flow-generated angiograms (B.ii) was used in addition to velocity-based thresholding. Velocity-based thresholding was performed to create volumetric isosurfaces, from which four measurement planes were distributed along the UtA and oriented perpendicular to the blood flow (B.iii). The vessel was segmented (B.iv) and velocity profiles (B.v) were

extracted from each plane at each phase. C, Velocity Waveform Analysis. Flow (Q), systolic velocity (v_{max}), diastolic velocity (v_{min}), mean velocity ($\bar{v}$), pulsatility (PI), and resistivity indices (RI) were estimated. We compared MRI and US in the corresponding UtAs of each subject.

	Time-of-Flight	4D flow
Flip angle	50 degrees	8 degrees
TR/TE	394/4.4 ms	5.5/2.67-3.13 ms
FOV	350 x 208-330 x 140-280 mm^3	192-320 x 176-320 x 16-174 mm^3
Voxel size	1.1 x 1.1 x 2.8 mm^3	1.17-2 x1.17-2 x1-2 mm^3
BW/pixel	200 Hz/pixel	445-455 Hz/pixel
Segments/shot	N/A	2
Temporal resolution	N/A	42.4-46.4 ms
# Cardiac phases	N/A	10-18
Acceleration factor	N/A	4.7
VENC	N/A	50-200 cm/s
Acquisition time	7-12 min.	12-20 min.

Abbreviations: FOV=field-of-view; BW/pixel=bandwidth per pixel; VENC=velocity encoding; TOF=time-of-flight

Table 4 Summary of uterine artery TOF and 4D flow MRI parameters.

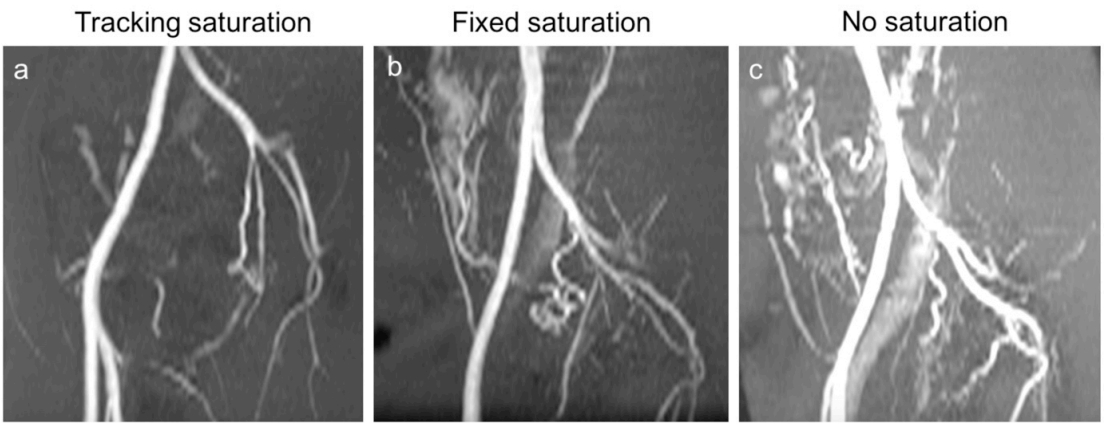

Figure 23 Comparison of TOF saturation schemes: a) saturation band that follows axial multi-slice acquisition from inferior to superior in an excluded subject, b) stationary saturation band below the uterine arteries in Subject 8, c) no saturation band in Subject 20. The stationary saturation band provided uterine artery details without displaying extensive venous signal contamination. Details on how saturation configuration relates to direction of blood flow in 2D TOF angiography can be found in [108].

4D flow MRI was obtained with a prospectively-gated time-resolved 3D phase contrast sequence with three-directional velocity encoding. Each cine cardiac phase consisted of four-point velocity encoding, 2 segments/shot, and 5.5 ms TR resulting in a temporal resolution of 8TR=44 ms. Other imaging parameters were as follows: Parallel MRI With Extended and Averaged GeneRalized Autocalibrating Partial Parallel Acquisition Kernels (PEAK-GRAPPA) acceleration factor=4.7 [145], velocity encoding parameter (VENC)=50-200 cm/s [22], acquisition time=12-20 min., number of cardiac phases=10-18 (Table 4). To reduce scan time, respiratory navigation or gating was not used. Online phase difference reconstruction with Maxwell correction of concomitant gradient terms was performed from the scanner [108, 146].

5.2.3.4 Image Analysis

MRI Vascular Geometry Analysis

The diameter of the UtAs were measured in the TOF multiplanar reformats at the location of intersection between the UtA and the external iliac artery on each side. Measuring the diameter of

the UtAs with US was not part of the study and therefore no area measurements were obtained to compute flow rate from US.

4D Flow MRI Data Analysis

Phase difference images from all the subjects were filtered and received anti-aliasing correction, if present (Figure 22.B.i), using custom software (Matlab; The MathWorks, Natick, MA, USA) [147]. Image noise was removed by magnitude image thresholding. All pixels below the threshold were removed from magnitude and phase data. Anti-aliasing was performed by phase unwrapping [148].

For the six subjects in Figure 25, additional masking was performed to reduce residual signal from outside the vessel regions (Figure 22.B.ii). Mean magnitude-weighted velocity phase contrast angiograms were generated as described in [147-149]. Additional manual segmentation was performed (Seg3D; Univ. of Utah SCI). The resulting binary segmentation was used to mask the magnitude and phase difference images.

For all subjects, filtered magnitude and phase difference images were imported into flow analysis software (Ensight, CEI; Apex, NC). A vascular isosurface was generated by thresholding the phase difference images. Eight planes were selected along the UtAs (four on each side), with the plane normal oriented parallel to the flow direction. The planes were distributed uniformly between the branching point of the internal iliac artery and UtA and the intersection of the UtA and the external iliac artery. The distal location was confirmed by fiducial markers placed during US as described in the methods section. Pathlines were generated to visualize the movement of blood for confirming the direction of flow and data visualization. The vessel lumen was segmented at each time point, and velocity profiles were generated (Figure 22.B.iii-v).

	Subject 16	Subject 25	Subject 30	Subject A	Subject B	Subject C
Condition/Outcome	Normal	Normal	Normal	Pre-pregnancy diabetes	Chronic hypertension	Chronic hypertension
GA (#weeks#days)	24w3d	26w5d	29w4d	26w4d	36w0d	36w3d
Maternal age (years)	22	27	23	32	23	20
Placental position	Posterior, far right	Anterior, center	Anterior, center	Posterior, center	Posterior, left	Posterior
TOF Angiogram						

Figure 24 Gestational age (GA), maternal age, placental position, and time-of-flight (TOF) angiogram of the pelvic arteries in three representative subjects (16, 25, 30) and three abnormal subjects (A, B, C).

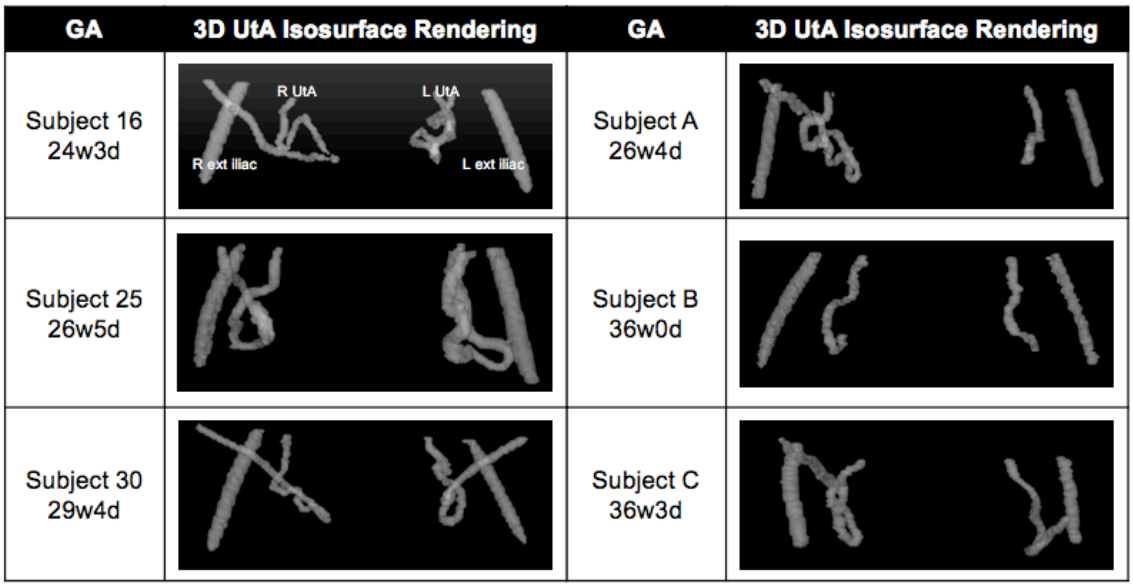

Figure 25 Uterine artery surface renderings obtained from 4D flow in three representative subjects and three abnormal subjects. There was considerable intersubject and intrasubject heterogeneity in the geometrical structure of the hairpin loop of the pelvic uterine arteries.

Velocity Analysis

4D flow phase difference images provided 3D velocity information to generate a time-resolved waveform for each plane. Let vector $\mathbf{v} = \langle v_x, v_y, v_z \rangle$ at each voxel represent velocity in cm/s and $\mathbf{n}$ be the unit normal vector to the plane pointing in the direction of blood flow. Let $v_\perp = \mathbf{v} \cdot \mathbf{n}$ be the scalar component of the velocity vector along $\mathbf{n}$ and parameterized as $v_\perp(i,t)$ where $i \in \{1, \dots, N\}|N$=number of voxels in the prescribed plane and $t \in \{1, \dots, T\}|T$=number of cardiac phases in one RR interval. Spatial peak and mean velocity are defined for each phase as $v_{\perp,I}(t) = \max_i v_\perp(i,t)$ and $\bar{v}_{\perp,I}(t) = \frac{\sum_{i=1}^{N} v_\perp(i,t)}{N}$, respectively. Temporal mean velocity is defined as $\bar{v}_{\perp,IT} = \frac{\sum_{t=1}^{T} v_{\perp,I}(t)}{T}$. Time-resolved waveforms were generated from the spatial peak and mean velocities, $v_{\perp,I}(t)$ and $\bar{v}_{\perp,I}(t)$, at each plane. Since 4D flow was a prospectively-gated scan, some cardiac phases were not collected during end-diastole. Missing data were extrapolated by filling the rest of the RR interval with the average between the first and last measured velocity.

Flow (Q) [mL/min] was computed from the spatial mean velocity waveforms from 4D flow. Pulsatility index (PI) and resistivity index (RI) were computed from both the spatial peak velocity waveforms from 4D flow and the Doppler velocity waveforms from US:

$$Q = \frac{A}{RR} \cdot \frac{60s}{min} \cdot \sum_{t=0}^{t=T} \bar{v}_{\perp,I}(t),$$

$$PI = \frac{\max_t v_{\perp,I}(t) - \min_t v_{\perp,I}(t)}{\bar{v}_{\perp,IT}}, \text{ and}$$

$$RI = \frac{\max_t v_{\perp,I}(t) - \min_t v_{\perp,I}(t)}{\max_t v_{\perp,I}(t)}, \text{ where}$$

A=cross-sectional area, RR=RR interval (sec), $\max_t v_{\perp,I}(t)$=systolic velocity, $\min_t v_{\perp,I}(t)$=diastolic velocity, and $\bar{v}_{\perp,IT}$=temporal mean velocity.

Q, PI, and RI were computed for each plane and were subsequently averaged together across the four planes per vessel. PI and RI were computed from the 4D flow MRI and US waveforms for comparison. For each subject, unilateral flow coefficient-of-variation (CoV) was determined. Intrascan reliability and inter- and intra-observer measurement reliability was performed. Most measurements had strong reliability (Table 7).

5.2.3.5 Statistical Analysis

Descriptive statistics are reported as mean±standard deviation(SD). Tests for statistical normality were performed on the 41 subjects were performed for statistical normality using the Shapiro-Wilk test and for heteroscedasticity using the Bartlett's and Breusch-Pagan tests. Correlations between variables were assessed by computing Pearson's R correlation coefficient for MRI flow rate and Spearman's rank correlation coefficients (rho) for US and MRI velocity parameters. Comparisons between modalities were reported using Wilcoxon signed rank tests and Bland-Altman plots. Statistical significance was defined as $p<0.05$.

5.2.4 Results

5.2.4.1 Subject Characteristics

26 subjects were recruited in the second trimester and 15 subjects in the third trimester. Subjects had a maternal weight=74.8±13.6 kg and gestational age (GA)= 26.0±5.1 (range=18-38) weeks. Individual subject information is summarized in Table 5. 4D flow MRI was acquired and well-tolerated in all subjects.

ID	Maternal age (y)	Maternal height (cm)	Maternal weight (kg)	Gestational Age (#weeks#days)	Gravidity and Parity
1	18	157	74	18w1d	unknown
2	34	155	49	18w3d	G1P0
3	32	170	82	18w4d	G1P0
4	18	165	62	18w5d	unknown
5	24	163	86	18w6d	G4P3
6	30	unknown	59	19w0d	G1P0
7	21	163	86	21w5d	G2P1
8	30	168	75	22w4d	G1P0
9	26	160	56	22w5d	G1P0
10	34	163	60	22w6d	G2P1
11	25	147	64	23w3d	G2P1
12	26	170	77	23w4d	G2P1
13	31	160	80	23w4d	G7P6
14	23	170	65	23w5d	G2P1
15	22	165	93	24w3d	G3P2
16	26	173	66	24w4d	G3P2
17	23	165	81	24w4d	G1P0
18	28	173	88	24w4d	unknown
19	20	155	57	25w3d	G3P2
20	33	168	85	25w3d	G2P1
21	19	175	106	25w4d	G1P0
22	41	157	66	25w5d	G3P2
23	34	152	68	25w5d	G3P2
24	32	178	89	26w4d	G3P2
25	27	160	56	26w5d	G3P2

26	22	157	81	26w6d	G3P2
27	35	156	63	27w6d	G2P1
28	19	165	80	28w5d	G1P0
29	39	175	93	28w6d	G4P3
30	23	150	55	29w4d	G1P0
31	21	157	80	29w4d	unknown
32	28	157	74	29w6d	G2P1
33	31	165	65	30w3d	G2P1
34	26	168	86	30w3d	G1P0
35	34	170	69	31w1d	G1P0
36	21	170	92	31w2d	G1P0
37	25	157	86	31w4d	G4P1
38	20	170	56	32w6d	G1P0
39	33	165	88	35w4d	G5P4
40	28	168	96	37w2d	G5P4
41	32	170	82	37w3d	G2P1

Abbreviations: G=gravidity, P=parity

Table 5 Subject demographic data

5.2.4.2 Uterine Artery Anatomy in Second and Third Trimester

In all subjects, right and left UtAs branched from the internal iliac artery, became a tortuous hairpin proximally, made a 180° turn from superior-inferior (SI) to IS trajectory, and became a distal straight segment towards the uterus before additional branching at the arcuate artery. UtA proximal segments were predominantly medial while distal segments were lateral and intersected the external iliac arteries at locations confirmed by MRI-compatible fiducials. Average UtA diameter within the imaged extent was 4.05±0.7 mm.

There was considerable inter- and intrasubject anatomical heterogeneity. GA, maternal age, maternal MRI position, placental position, and arterial TOF angiograms of six representative subjects are shown in Figure 24. Figure 25 shows heterogeneity in the geometry of the left and right UtA from the same six representative subjects (see also Supplementary Video 1 in [150]).

5.2.4.3 Uterine Artery Hemodynamics

Hemodynamic measurements from 4D flow MRI were reported as the average of measurements in four planes. Flow in the left UtA was Q_L=291±111 mL/min, right UtA was Q_R=322±147 mL/min, and bilateral (total) flow was Q_T=606±221 mL/min. Flow rate measurement reliability statistics are reported in **Section 5.2.4.5** and Table 7. There was no association between UtA bilateral flow and GA in these subjects (R^2=0.01, p=0.49) (Figure 26). UtA structure and hemodynamics are shown using pathlines derived from one representative subject in Figure 27 and Supplementary Video 2 in [150].

MRI differed from US in terms of PI (0.72±0.26 vs. 0.84±0.42, p=0.05) and RI (0.47±0.11 vs. 0.50±0.11, p=0.13) based on Wilcoxon signed rank tests (Figure 28). MRI and US were also moderately correlated in terms of systolic velocity (ρ=0.39, p<<0.01), diastolic velocity (ρ=0.42, p<<0.01), mean velocity (ρ=0.44, p<<0.01) (Figure 29), PI (ρ=0.37, p<<0.01), and RI (ρ=0.38, p<<0.01) (Figure 30).

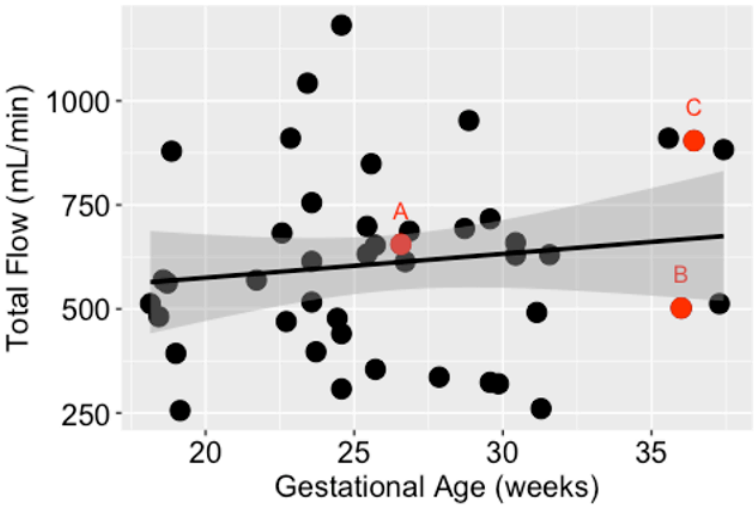

Figure 26 Scatter plot of flow vs. gestational age across forty-one subjects with results from a linear fit and Pearson's correlation analysis including 95% confidence interval (gray region). Red dots indicate abnormal subjects (A,B,C).

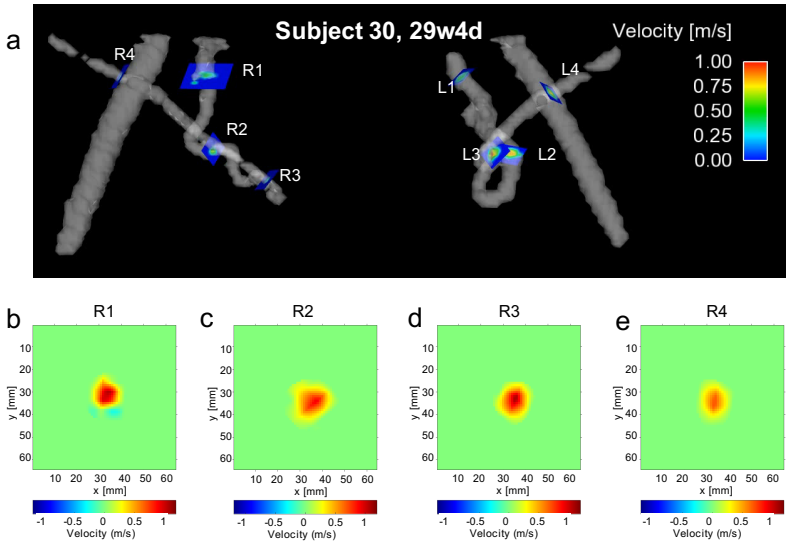

Figure 27 a) The eight 4D flow planes, four planes on each side, distributed along the UtAs in Subject 30. Planes R4 and L4 were estimated to correspond with the location of Doppler US velocity measurements. The interpolated velocity profiles of planes R1 (b), R2 (c), R3 (d), and R4 (e) are shown.

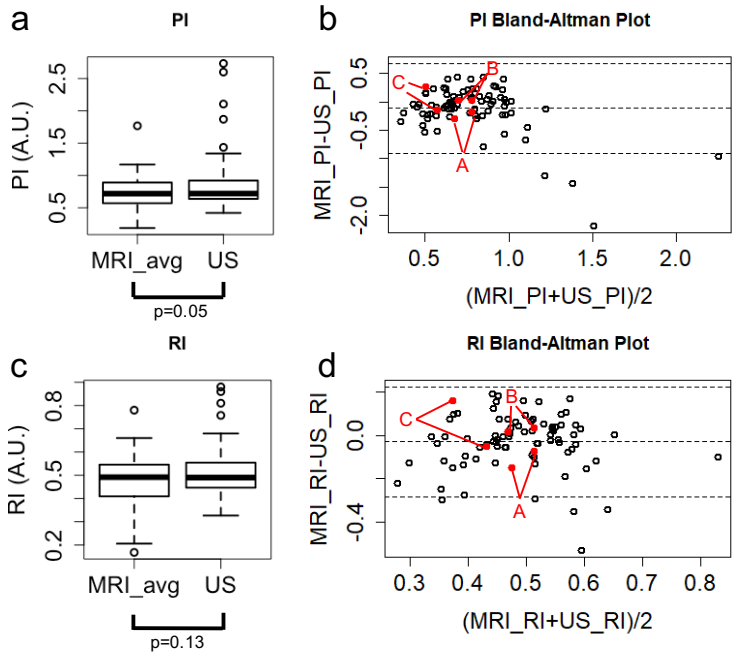

Figure 28 Box-and-whisker and Bland-Altman plots of pulsatility index (a,b) and resistivity index (c,d) comparing MRI and US.

5.2.4.4 Feasibility in Subjects with Risk Factors for Adverse Pregnancy

We separately identified three subjects with representative risk factors for adverse pregnancy, one with pre-pregnancy diabetes mellitus and two with chronic hypertension. In these subjects, 4D flow MRI was feasible. Individual subject information is reported in Table 6. For Subject A with diabetes, we measured Q_T=655.5 mL/min and average unilateral PI=0.61. For Subject B with chronic hypertension, we measured Q_T=502.4 mL/min and PI=0.75. For Subject C with chronic hypertension, we measured Q_T=904.4 mL/min and PI=0.57. These results demonstrate that measurement of these hemodynamic parameters were feasible in abnormal pregnant subjects with 4D flow MRI. These subjects are presented in Figure 24 and Figure 25. Their results are annotated in Figures 26, 28-30.

ID	Maternal age (y)	Maternal height (cm)	Maternal weight (kg)	Gestational Age (#weeks#days)	Gravidity and Parity	Risk Factor
A	25	175	84	19w1d	unknown	Diabetes mellitus
B	23	160	83	36w0d	G1P0	Chronic hypertension
C	20	168	96	36w3d	G2P1	Chronic hypertension

Table 6 Abnormal subject demographic data

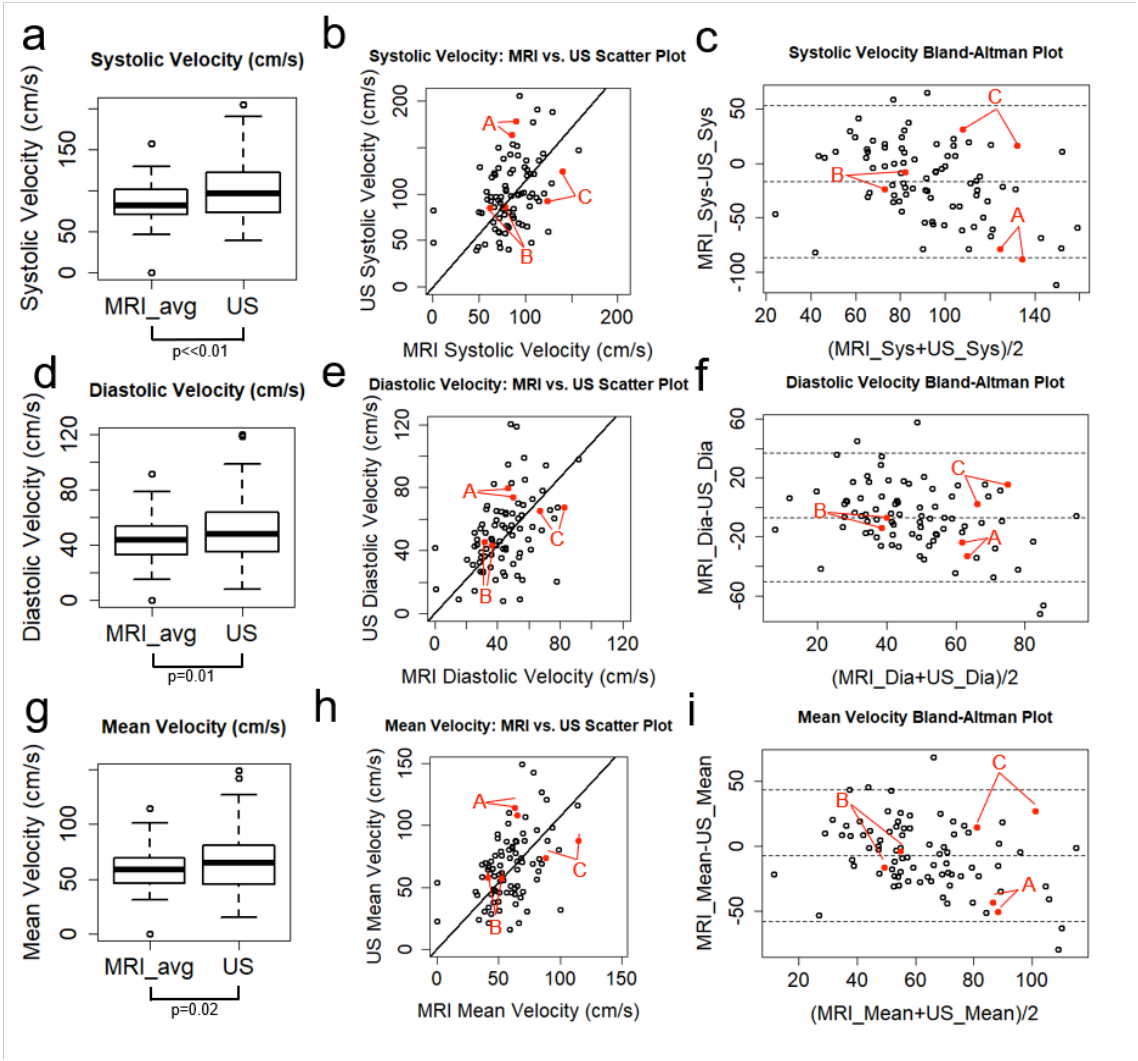

Figure 29 Box-and-whisker, Spearman's rho correlation coefficients with linear fit, and Bland-Altman plots comparing MRI and US in terms of systolic velocity (a,b,c), diastolic velocity (d,e,f), and mean velocity (g,h,i).

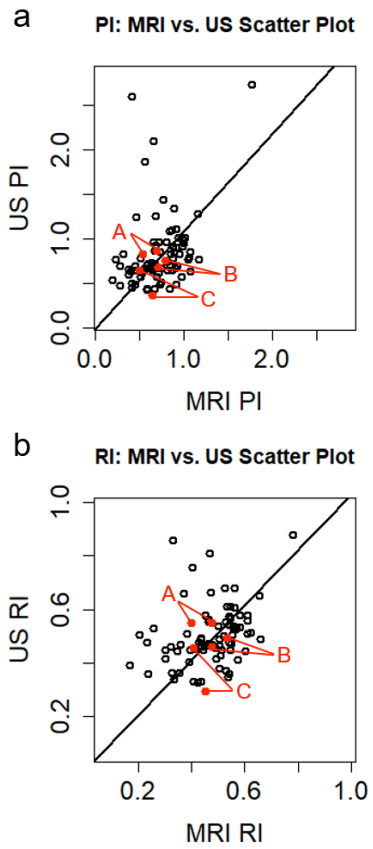

Figure 30 Spearman's rho correlation coefficients with linear fit comparing MRI and US in terms of PI (a) and RI (b).

5.2.4.5 Reliability analysis of 4D flow MRI measurements

We include supplementary information reported in Hwuang et al. [150] to further discuss the reliability of 4D flow MRI by taking into account potential confounders. This section provides details on how 4D flow MRI was assessed in terms of: 1) reliability in repeated measurements of flow rate, 2) comparison with US after removing temporal resolution differences, and 3) eddy current correction.

Flow Rate Reliability Analysis

To determine scan-rescan reliability of step A.iii (Figure 22), two subjects were scanned twice consecutively in an imaging session and the intraclass correlation coefficient (ICC) of the flow rate was determined. To determine interobserver measurement reliability, two users each performed post-processing steps B.i, B.iii, B.iv (Figure 22) and the ICC was determined for bilateral and unilateral flow. To determine intraobserver measurement reliability, one user performed post-processing steps B.i, B.iii, B.iv and B.iv (contouring alone) and the ICC was determined for bilateral and unilateral flow. Scan-rescan, interobserver, and intraobserver reliability were measured by ICC(consistency) and ICC(absolute agreement) based on results from two-way analysis of variance (ANOVA) without replication using the procedure described in [151]. The results are reported in Table 7. We also measured the variation across the four planes prescribed in each UtA in the forty-one subjects. The average of standard deviation across the four planes was 78.9 mL/min in the right UtA and 68.5 mL/min in the left UtA. The coefficient of variation of unilateral flow was 27.4±16.6% in the right UtA and 24.0±10.6% in the left UtA.

Scenario in which Q was measured:	ICC (consistency)	ICC (absolute agreement)
1. Unilateral flow intrascan reliability (n=2)^	0.99	0.83
2. Bilateral flow measurement interobserver reliability n=5)*	0.98	0.86
3. Unilateral flow measurement interobserver reliability (n=5)*	0.98	0.89
4. Bilateral flow measurement intraobserver reliability (n=5)*	0.90	0.68
5. Unilateral flow measurement intraobserver reliability (n=5)*	0.89	0.79
6. Unilateral flow measurement intraobserver reliability (n=1)#	>0.99	>0.99

^reliability of step A.iii of Figure 22

*reliability of steps B.i, B.iii, and B.iv of Figure 22

#reliability of step B.iv of Figure 22

Table 7 ICC results for reliability experiments with repeated flow rate measurements using 4D flow. ICC (consistency) and ICC (absolute agreement) were computed from the results of a two-way ANOVA.

Temporal Resolution in MRI-US Comparisons

We were interested in seeing if the difference in temporal resolution between MRI and US played a role in the agreement between the two modalities when measuring velocity-based parameters. While the US parameters reported in the main text were given by the US machine, we separately processed the waveforms for this supplementary analysis. The US velocity waveforms from each UtA were extracted from the images by cropping, binary thresholding, and edge detection in MATLAB (MathWorks; Natick, MA). The US data (~160-360 points/cardiac cycle) was downsampled to match the temporal resolution of 4D flow MRI (~14 cardiac phases). We then repeated the MRI-US comparative statistical analyses (Wilcoxon signed rank test, Spearman's rho correlation coefficient, and Bland-Altman plot) with the downsampled version of the US waveforms. The results are reported in Table 8. In general, it appears that the downsampled US measurements were closer than the original US machine measurements to the MRI measurements, indicating that the difference in temporal resolution may play a role in the agreement between MRI and US.

	MRI	US	US_{ds}	Wilcoxon		ρ		Mean difference [95% limits of agreement]	
				MRI vs. US	MRI vs. US_{ds}	MRI vs. US	MRI vs. US_{ds}	MRI-US	MRI-US_{ds}
Systolic velocity (cm/s)	83.8±25.3	99.9±36.7	96.2±35.1	p<<0.01*	p<<0.01*	ρ=0.39 p<<0.01*	ρ=0.41 p<<0.01*	-16.0 [-84.3,52.3]	-12.3 [-77.5,52.8]

RI (A.U.)	0.47±0.11	0.50±0.11	0.51±0.13	p=0.13	p=0.04*	ρ=0.38 p<<0.01*	ρ=0.40 p<<0.01*	<-0.1 [-0.3,0.2]	<-0.1 [-0.3,0.2]
PI (A.U.)	0.72±0.26	0.84±0.42	0.88±0.53	p=0.05*	p=0.02*	ρ=0.37 p<<0.01*	ρ=0.37 p<<0.01*	-0.1 [-0.9,0.7]	-0.2 [-1.1,0.8]
Mean velocity (cm/s)	58.9±19.5	65.6±27.8	63.1±27.4	p=0.02*	p=0.17	ρ=0.44 p<<0.01*	ρ=0.49 p<<0.01*	-6.7 [-57.2,43.8]	-4.3 [-52.5,44.0]
Diastolic velocity (cm/s)	44.1±16.5	50.6±23.7	48.5±23.6	p=0.01*	p=0.12	ρ=0.42 p<<0.01*	ρ=0.49 p<<0.01*	-6.5 [-50.6,37.6]	-4.4 [-46.6,37.9]

*Wilcoxon or Spearman's rho, p<0.05

Table 8 Comparison of MRI, US, and downsampled US (USds) velocity-based parameters. We report mean±standard deviation, Wilcoxon signed rank test p-value, Spearman's rho correlation coefficient (ρ) with p-value, and Bland-Altman mean difference with limits of agreement based on a 95% confidence interval.

Eddy Current Correction

While we did not perform eddy current correction (ECC) in the original 4D flow cohort, we were interested in assessing the impact of ECC on the results. Therefore, in six subjects we performed steps B and C (Figure 22) with the addition of eddy current correction using custom software (Matlab; The MathWorks, Natick, MA, USA) developed by UKL Freiburg and NU Radiology [147]. We report ICC between flow measurements generated with and without ECC (Table 9). The paired Wilcoxon signed rank test between the two versions of unilateral flow was not significant (p=0.08). We also present a Bland-Altman plot of unilateral flow rate (Figure 31).

Scenario in which Q was measured:	ICC (consistency)	ICC (absolute agreement)

1. Bilateral flow measurement (n=5)*	0.86	0.84
2. Unilateral flow measurement (n=5)*	0.92	0.89

Table 9 Comparison of flow measurements using 4D flow with and without eddy current correction.

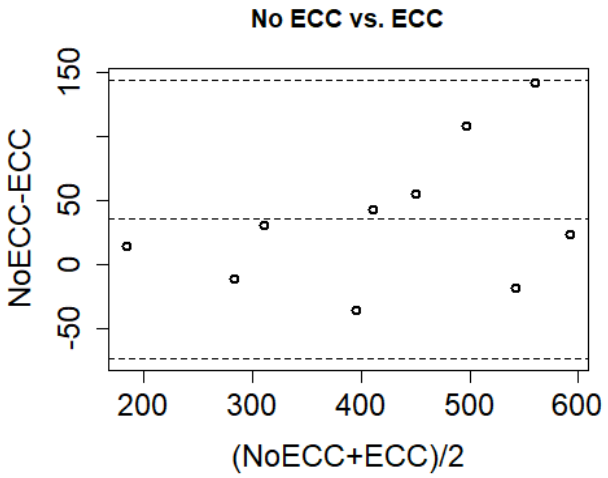

Figure 31 Bland-Altman plot of unilateral UtA flow rate measured with 4D flow MRI with and without eddy current correction (ECC). The mean difference was 35.12 mL/min with 95% limits of agreement [-73.57,143.8] mL/min.

5.2.5 Discussion

We report the feasibility of UtA anatomical and hemodynamic assessment in second and third trimester pregnant subjects using 4D flow MRI acquired at 1.5T. 4D flow images enabled detailed characterization of the UtA blood flow, independent of the orientation of the examination plane, and at locations inaccessible to US. After branching from the internal iliac artery, the tortuous UtA traversed inferiorly and medially, formed a hairpin loop in the pelvis, and subsequently carried blood superiorly and laterally to radial and spiral arteries. This anatomy has been partly described in embolization procedures for peripartum hemorrhage [152, 153], however there is limited knowledge of its normal and pathophysiologic anatomical variation. We observed substantial

bilateral UtA anatomical and hemodynamic heterogeneity, which may reflect variations in placental location, molecular signals that promote UtA remodeling and growth, body habitus, and variations in patient position during imaging.

UtA diameter derived from TOF agreed with previous reports obtained using 2D phase contrast MRI [20, 154] and US [63, 155]. UtA outward hypertropic remodeling occurs throughout gestation and the vessel cross-sectional area enlarges [46, 63, 155]. Similar positive associations between flow rate and GA have also been reported [63, 142]. These studies show a moderate association between flow and GA in the first trimester [142], but a comparatively weaker association in the second and third trimester [63], suggesting that the most extensive UtA remodeling occurs during the first trimester. Our findings in second and third trimester subjects were consistent with this, and no substantial blood flow changes in the late second and third trimesters were found. This contrasts with fetal weight growth, which is slower in the first two trimesters than the third [105]. Altogether, these findings suggest that during early placental development the UtAs are primed to increase blood flow so that the placenta may have sufficient reserve to accommodate changes in fetal oxygen demand during late gestation. Failure of UtA growth and remodeling with placental dysfunction in the first trimester may limit fetal growth in later trimesters.

There was moderate correlation between PI and RI obtained using MRI and US, which was consistent with prior observations using 2D phase contrast MRI [21]. However, some observed discordance between MRI and US may be attributed to hemodynamic differences caused by body habitus [156] during MRI (mostly supine) and US (inclined supine), location of measurement, and differences in temporal and spatial resolution. Previous studies have reported flow rate measured with US [142, 155, 157] but this was omitted in this study. US-based flow rate requires measurement of diameter, which has not yet been standardized in obstetric research because the UtA lumen is not always clearly visible from low spatial resolution and vessel tortuosity.

Time-resolved three-dimensional velocity field data can be used to compute additional complex flow parameters such as relative pressure gradients [158], pulse wave velocity [159], and wall shear stress [159]. These flow parameters in the UtA may provide new predictive markers of pregnancy health in early gestation. Decreased vascular resistance at the uteroplacental junction increases UtA blood flow, which may increase wall shear stress and stimulate endothelial production of nitric oxide (NO) [46, 60, 160]. Targeted therapies such as dietary arginine supplementation may increase NO production, vasodilatory remodeling, and improve UtA flow [13]. Additional imaging markers may improve the predictive value of these studies.

All MRI scans performed in this study were below the limit mandated by the United States Food and Drug Administration (FDA). No additional restrictions were placed on the hardware beyond the current FDA limitations on rate of time-varying magnetic fields (dB/dt) and maximum allowable specific absorption rate (SAR). While caution is recommended when imaging obstetric patients, most recent guidelines have identified MRI to be safe in this population because concerns about harm to the fetus remain theoretical with no established clinical evidence [161, 162]. The American College of Radiology states that no special considerations need to be made for women in their first trimester more than any other trimester [163]. Studies of MRI in pregnancy have shown MRI exposure to not pose a concern for adverse fetal outcome in the first trimester [126] and after the first trimester [164, 165]. In this study, no additional safety considerations were enforced beyond the FDA requirements.

This cross-sectional study may be affected by physiologic subject variation (e.g. height, weight, and internal iliac branching geometry) that can potentially be reduced with a longitudinal study. Subjects can also vary in the distribution of flow between the uterine and ovarian arteries. As a result, interpretations about placental perfusion from only UtA flow assessment can be misleading. It is possible that the ovarian arteries also remodel during gestation because the PI has been found to be lower than in non-pregnant subjects similar to the UtA [166, 167]. There are

also some limitations of 4D flow assessment of UtA function. The tortuous UtAs may cause MRI acceleration and displacement artifacts such as inaccurate velocity encoding and spatial encoding. The current spatial resolution may preclude accurate flow quantification in the first trimester. In non-pregnant subjects scanned during protocol development, we observed that the UtA was not readily visible. Even when the UtA is visible in pregnant subjects, three voxels span the vessel at best, which does not allow the calculation of pressure gradient or wall shear stress. Pulse wave velocity can possibly be calculated with high temporal resolution or a long vessel path to compensate for low spatial resolution. Nevertheless, our 4D flow acquisition has a spatial resolution that is superior to the state-of-the-art of 2D PC acquired of the UtA reported in [154]. Respiratory gating was not performed in our subjects to reduce scan time as much as possible. Consequently, potential sources of artifacts include fetal and peristaltic motion. Further investigation is needed to determine if respiratory gating reduces artifacts sufficiently to justify the additional scan time. Future work leveraging more highly parallelized acquisitions and sparse imaging methods may also be needed to increase spatial resolution and/or reduce scan time. This may allow us to robustly image the UtA in the first trimester, compute complex flow parameters, and provide a larger FOV to capture more distal segments of the ascending UtA later in pregnancy.

5.2.6 Conclusions

This study shows the feasibility to characterize UtA anatomy and hemodynamics using 4D flow MRI in second and third trimester pregnancies. Expected flow characteristics were validated across GA with no observed bias with respect to transabdominal Doppler US.

CHAPTER 6: PATHOPHYSIOLOGY OF HYPERTENSIVE PREGNANCY DISORDER AS ASSESSED USING NON-INVASIVE IMAGING

6.1 Review of US assessment of uterine artery to screen for HPD

Screening studies have been conducted to assess the utility of uterine artery Doppler ultrasound for predicting the development of HPD. Despite high specificity and high negative predictive value, uterine artery Doppler ultrasound had poor positive predictive value, meaning that many women with abnormal uterine artery waveforms had normal pregnancies. It also had poor sensitivity, especially missing women who would develop late-onset preeclampsia [139, 168]. More recently, researchers sought to improve upon screening for HPD in the first trimester by developing multi-parametric models combining uterine artery Doppler ultrasound with maternal factors and serum biomarkers [16, 17]. However, this approach is still under investigation. The following study begins to examine the performance of MRI-based uterine artery assessment in relation to clinical outcome and compares it to the performance of ultrasound. Uterine artery flow measured by MRI was significantly lower in pregnant women with preeclampsia and/or small-for-gestational age deliveries than in normal pregnant women.

6.2 Uterine artery assessment by 4D flow MRI in association with delivery outcomes

6.2.1 Abstract

Clinical assessment of uterine artery (UtA) hemodynamics is currently limited to ultrasound (US) Doppler velocimetry. We previously demonstrated the feasibility of 4D flow magnetic resonance imaging (MRI), which allows flow quantification throughout the entire vessel, to evaluate UtA

hemodynamics during pregnancy. In this study, we seek to further validate the physiologic relevance of 4D flow MRI measures of UtA blood flow rate by exploring their associations with pregnancy outcomes relative to US-based metrics.

This was a cross-sectional study of 87 singleton pregnant women, enrolled between May 2016 and April 2019, who underwent a 4D flow MRI scan to measure UtA pulsatility index (PI) and blood flow rate (in mL/min). UtA PI was also measured using US. The primary outcome was a composite (COMP) of either preeclampsia (PEC), small for gestational age (SGA), or both PEC+SGA. The secondary outcomes were PEC and SGA individually. Wilcoxon rank-sum tests were performed to study the ability of MRI-flow, MRI-PI, and US-PI to distinguish between no disease versus disease. Linear regression was also performed to study MRI-flow versus gestational age (GA).

Of the 74 subjects that were analyzed, 18 subjects were COMP: PEC (n=3), SGA (n=11), and both PEC+SGA (n=4). Additionally, one subject excluded from the analysis had an intrauterine fetal demise (IUFD). When comparing subjects with and without COMP, no differences in maternal age, body mass index (BMI), nulliparity, gravidity, or race were found. In 66 of the 74 subjects US data was also available. Both median MRI-PI (0.95 vs. 0.70, $p<0.01$) and median US-PI (0.95 vs. 0.73, $p<0.01$) were significantly increased in subjects with COMP compared to no COMP. UtA blood flow rate, as measured by MRI, did not significantly increase from 2nd to 3rd trimester (median flow [interquartile range]=543[419,698] vs. 575[440,746] mL/min, $p=0.77$), but it was significantly lower in COMP compared to no COMP (median flow [interquartile range]=486[366,598] vs. 623[457,749] mL/min, $p=0.04$). The AUCs for MRI-flow, MRI-PI, and US-PI in predicting COMP were comparable (0.69, 0.74, and 0.73) with non-significant differences among the three AUCs ($p=0.87$).

4D flow MRI can yield physiologic measures of UtA blood flow rate and PI that are associated with adverse pregnancy outcomes. This may open new avenues in the future to explore more robust MRI-based evaluation of UtA hemodynamics in pregnancy.

6.2.2 Introduction

Doppler ultrasound (US) assessment of the maternal uterine arteries (UtAs) has shown promising results for predicting risk of adverse pregnancy outcomes [16, 17], but the multiparametric models required for these assessments are more complex than current clinical US practice. US also has inherent limitations, such as its sensitivity to the angle between the device and the interrogated flow direction, that preclude accurate and reproducible assessment of UtA remodeling and hemodynamic function during pregnancy [141]. The Nulliparous Pregnancy Outcomes Study: Monitoring Mother-to-be (nuMoM2b) study found UtA Doppler US to have low positive predictive value in predicting small-for-gestational-age neonates [18]. Other studies have reported variable results depending on gestational age of onset of preeclampsia [169] and superimposed fetal growth restriction [170]. Mounting evidence suggests that some women with abnormal trophoblast invasion have normal UtA Doppler waveforms while others with abnormal UtA Doppler waveforms have healthy deliveries [171, 172]. Thus, a more robust tool to investigate UtA remodeling and hemodynamics during pregnancy is still needed.

Four-dimensional (4D) flow magnetic resonance imaging (MRI) time-resolves each component of the blood flow velocity vector along with morphological data in a single, non-invasive, non-ionizing scan [173]. This is advantageous given the complex hemodynamic nature in various cardiovascular conditions. Therefore, it has successfully been used to measure advanced parameters such as pressure and wall shear stress [158, 174-176]. During pregnancy, a key advantage of 4D flow MRI is its large spatial coverage allowing for evaluation of the entire course of the UtA. We previously demonstrated that this modality is technically feasible in pregnant women [150] but did not correlate UtA flow measurements with pregnancy outcomes. In this

study, we sought to further validate the 4D flow MRI measures of UtA blood flow by exploring the association of these measures with adverse pregnancy outcomes and by comparing these associations with similar associations drawn from Doppler US.

6.2.3 Methods

6.2.3.1 Study participants

A total of 87 singleton pregnant subjects were enrolled between May 26, 2016 and April 25, 2019 in this cross-sectional study approved by the institutional HIPAA-compliant Institutional Review Board. Inclusion criteria included singleton gestations at 15 weeks or greater. Exclusion criteria were: (1) morbid obesity (pre-gravid BMI ≥ 35), (2) major structural fetal anomaly, (3) routine MRI contraindications such as metallic implants/devices and claustrophobia. For some analyses involving comparison with outcomes, subjects lost to follow-up after MRI were not included, and subjects with intrauterine fetal demise (IUFD) were analyzed separately from deliveries after 24 weeks with neonates that reached viability. Only subjects whose pregnancies reached viability and whose obstetric outcomes were available were included in analyses comparing MRI to pregnancy outcomes. For analyses involving associations between US-pulsatility index (PI) and pregnancy outcomes, subjects without US scans were not included. Pregnancy outcomes were extracted from the medical record. The primary outcome was a composite (COMP) of either or both preeclampsia (PEC), as defined by the American College of Obstetricians and Gynecologists criteria [78], and small for gestational age (SGA) defined as birth weight <10th percentile [177]. Secondary outcomes were PEC and SGA individually. Both MRI-PI and MRI-flow were each analyzed as predictors of the outcomes, while US-PI was also analyzed as a predictor of outcome for comparison.

6.2.3.2 Measurement of PI and flow with 4D flow MRI

Prospective ECG-gated 4D flow MRI [150] at 1.5T (Avanto, Siemens Healthineers, Erlangen, Germany) was acquired of the UtAs and external iliac arteries near the internal orifice of the cervix (Fig. 32) using a 12-channel spine and two 4-channel body matrix coils. The sequence parameters were: flip angle=8°, repetition time/echo time=5.5/3ms, voxel size=1.25x1.25x1.25mm^3, field-of-view=320x200x60mm^3, bandwidth per pixel=445-455 Hz/pixel, segments/shot=2, temporal resolution=42.4-46.4ms, acceleration factor=4.7, velocity encoding (VENC)=100 cm/s, number of cardiac phases=10-18, and scan time=12-20 minutes depending on subject's heart rate. Noise was removed from the velocity maps with thresholding and four planes distributed along each vessel were manually prescribed to extract velocity maps at each plane location (Ensight, CEI; Apex, NC). On each velocity map, the UtA was manually contoured using custom software (Matlab; The MathWorks, Natick, MA, USA). MRI-PI was computed from the spatial maximum MRI velocity waveforms as $PI = (v_{max}\text{-}v_{min})/\bar{v}$ and averaged across the four planes for each vessel, where v_{max}=temporal maximum velocity, v_{min}=temporal minimum velocity, and $\bar{v}$=temporal mean velocity. UtA flow rate (mL/min) was computed from the spatial mean MRI velocity waveforms and vessel cross-sectional area and averaged across the four planes for each vessel (Fig. 32). More details about the MRI acquisition, post-processing procedure, repeatability of 4D flow MRI scans, and interobserver reproducibility of post-acquisition measures were previously described [150].

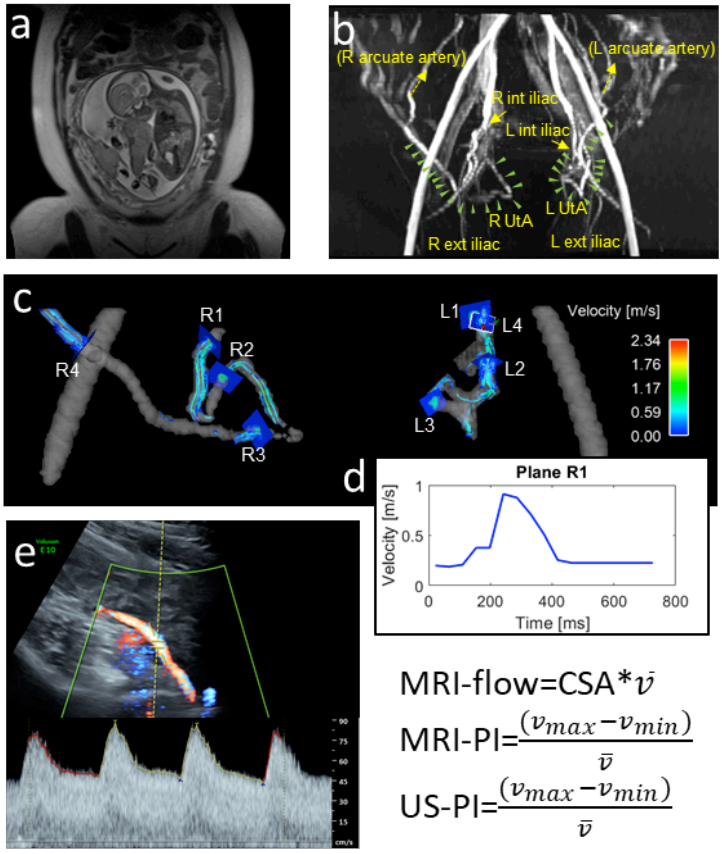

Figure 32 Diagram outlining methodological workflow: a) MRI localizer, b) time-of-flight MRI angiogram, and c) 4D flow MRI were collected from UtAs. 4D flow post-processing consisted of extracting velocity waveforms from each plane (example for Plane R1 shown in (d)). e) Transabdominal Doppler US was collected from the UtAs. MRI-flow was computed by multiplying cross-sectional area (CSA) by mean velocity ($\bar{v}$) from 4D flow data. MRI-PI and US-PI were computed from 4D flow MRI and US waveforms, where v_{max}=systolic maximum velocity and v_{min}=diastolic minimum velocity. For each subject, MRI-flow was averaged across four planes in each UtA and added together for total bilateral MRI-flow used in subsequent statistical analysis. MRI-PI and US-PI were also averaged from repeated measurements or planes and additionally averaged from both UtAs.

6.2.3.3 Measurement of PI with Doppler US

Each subject was positioned in semi-recumbent supine. The UtAs were scanned using the C4-8 transabdominal probe of a GE Voluson E10 (GE Healthcare, Wisconsin, United States) US machine by a Maternal Fetal Medicine clinician (Nadav Schwartz, MD) with extensive experience

in prenatal US. An average of three measurements of UtA Doppler PI values were recorded bilaterally.

6.2.3.4 Statistical Analysis

MRI-flow, MRI-PI, and US-PI values are reported as median and interquartile range (IQR, 25%-75%) or mean and standard deviation (SD). Scatter plots of MRI-flow versus gestational age (GA) were generated and R-squared calculated from fitting linear regression models. Wilcoxon rank-sum test was used to investigate differences in MRI-flow, MRI-PI, and US-PI between the pregnancies with and without one of the three outcomes (COMP, PEC, and SGA). We also report adjusted results after accounting for demographic parameters that were statistically significantly different between COMP and no COMP. In addition, Spearman's correlation and Wilcoxon signed-rank test were used to compare between MRI-PI and US-PI. Receiver-operating characteristics (ROC) curves and the corresponding area under the curve (AUC) were generated for MRI-flow, MRI-PI, and US-PI across outcomes, and a Wald test was used to compare the AUC values associated with MRI-PI and US-PI. Statistical significance was considered at $p<0.05$. Statistical analysis was performed using Stata 14.2 (College Station, TX).

6.2.4 Results

6.2.4.1 Delivery Outcomes and Exclusions

After recruitment for MRI, 4D flow post-processing, and applying exclusions for analysis, data from 74 pregnant subjects were analyzed for both UtAs (Fig. 33, Table 10). The remaining subjects included one with IUFD and 7 subjects lost to follow-up. Of the 74 subjects, 18 developed a COMP outcome, including 3 with PEC, 11 with SGA, and 4 with both. In 66 of the 74 subjects US Doppler data was acquired on the same day as MRI (Fig. 33, Table 11). No significant demographic differences between COMP and no COMP were found in terms of age, race, BMI, nulliparity, and gravidity (Table 11). However, in comparison to no COMP subjects, the

COMP subjects were scanned at later GA and delivered at earlier GA with lower birthweight. They also had higher rates of chronic hypertension (CHTN). 39 out of the 74 subjects (35 out of the 66 subjects) were also reported in a previous study [150].

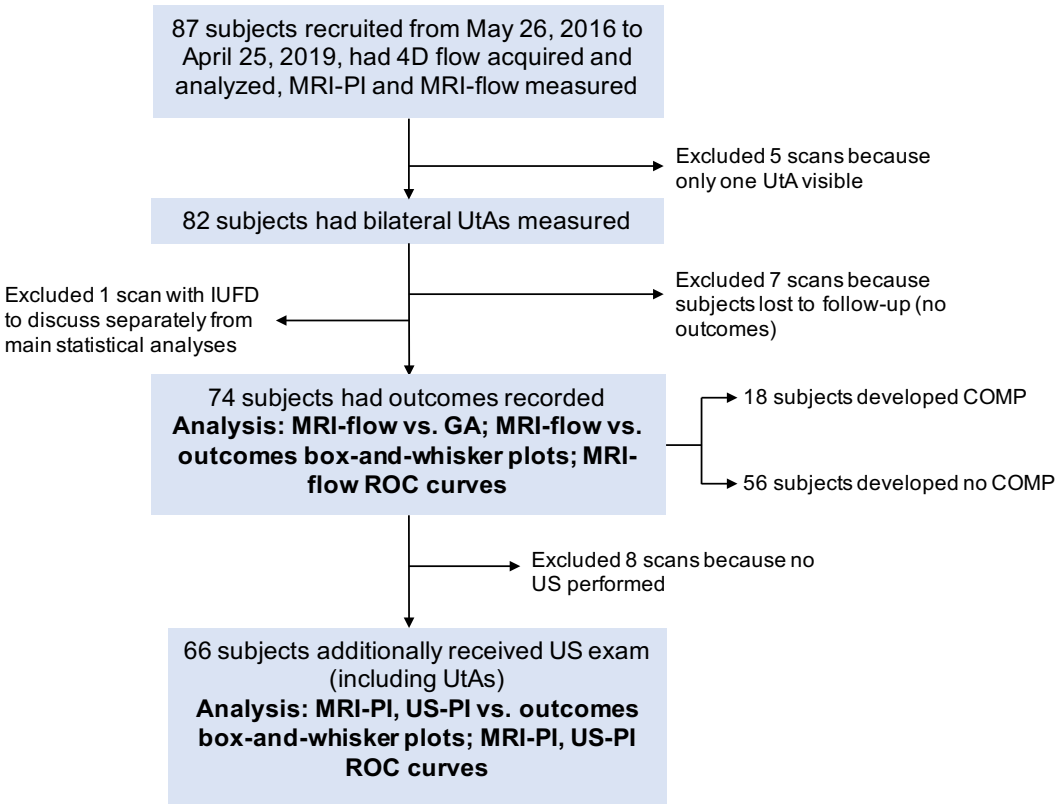

Figure 33 Diagram of exclusion criteria for analysis

	Cohort with Delivery Info	COMP	No COMP	p-value
N (%)	74 (100)	18 (24)	56 (76)	
Age (std)	27.5 (6.2)	26.2 (5.9)	27.9 (6.3)	0.315

Race				0.223
Black (%)	53 (72)	16 (89)	37 (66)	
White (%)	16 (22)	2 (11)	14 (25)	
Other (%)	5 (7)	0 (0)	5 (9)	
BMI (IQR)	30.2 (26.2-33.3)	30.2 (25.2-34.6)	30.2 (26.2-32.7)	0.99
Nulliparity (%)	41 (55)	9 (50)	32 (57)	0.596
Gravidity (IQR)	2 (1-3)	2 (1-3)	2 (1-3)	0.521
CHTN (%)	6 (8)	4 (22)	2 (4)	0.028*
GDM (%)	6 (8)	2 (11)	4 (7)	0.592
GA at delivery (IQR)	39.3 (37.9-40.1)	37.3 (37.1-39.0)	39.5 (38.4-40.6)	0.001*
Birthweight (g) (IQR)	3147.5 (2680-3620)	2375 (2015-2685)	3310 (3072.5-3679.5)	0.001*
GHTN (%)	16 (22)	6 (33)	10 (18)	0.165
PEC (%)	7 (9)	7 (39)	0 (0)	0.001*
SGA (%)	15 (20)	15 (83)	0 (0)	0.001*
GA at MRI (IQR)	28.4 (23.6-32.9)	31.6 (25.7-36.4)	26.6 (23.1-31.2)	0.009*
Total Uterine Artery Flow (mL/min) - MRI (IQR)	591.8 (440.9-742.5)	486.1 (366.1-598.2)	623.8 (456.6-748.6)	0.038*

Table 10 Demographic information for subjects with delivery info, divided into subsets COMP and no COMP. BMI=body mass index, CHTN=chronic hypertension, GDM=gestational diabetes mellitus, GA=gestational age, GHTN=gestational hypertension, PEC=preeclampsia, SGA=small-for-gestational age, PI=pulsatility index, %=percentage, std=standard deviation, IQR=interquartile range (25%-75%), p-values reported from two-sample Wilcoxon rank-sum test, *p<0.05

	Cohort with Delivery & US Info	COMP	No COMP	p-value
N (%)	66 (100)	15 (23)	51 (77)	
Age (std)	28.1 (6.3)	27.2 (6.0)	28.3 (6.4)	0.542
Race				0.289

Black (%)	46 (70)	13 (87)	33 (65)	
White (%)	15 (23)	2 (13)	13 (25)	
Other (%)	5 (8)	0 (0)	5 (10)	
BMI (IQR)	30.6 (26.2-33.4)	31.3 (25.5-35.0)	30.4 (26.2-32.6)	0.493
Nulliparity (%)	34 (52)	6 (40)	28 (55)	0.31
Gravidity (IQR)	2 (1-3)	2 (1-3)	2 (1-3)	0.675
CHTN (%)	6 (9)	4 (27)	2 (4)	0.021*
GDM (%)	6 (9)	2 (13)	4 (8)	0.516
GA at delivery (IQR)	39.1 (37.7-40.0)	37.1 (36.7-39.0)	39.4 (38.3-40.3)	0.001*
Birthweight (g) (IQR)	3142.5 (2685-3640)	2380 (1885-2690)	3350 (3050-3740)	0.001*
GHTN (%)	16 (24)	6 (40)	10 (20)	0.105
PEC (%)	7 (11)	7 (47)	0 (0)	0.001*
SGA (%)	12 (18)	12 (80)	0 (0)	0.001*
GA at MRI and US (IQR)	27.4 (23.4-32.9)	31.6 (25.7-36.4)	25.6 (22.6-31.1)	0.013*
Uterine Artery PI, Right - US (IQR)	0.71 (0.62-0.99)	0.84 (0.71-1.14)	0.69 (0.58-0.96)	0.015*
Uterine Artery PI, Left - US (IQR)	0.79 (0.67-0.92)	0.91 (0.76-1.67)	0.78 (0.65-0.87)	0.008*
Uterine Artery PI, mean - US (IQR)	0.78 (0.67-1.03)	0.95 (0.76-1.37)	0.73 (0.64-0.92)	0.007*
Uterine Artery PI, Right - MRI (IQR)	0.71 (0.58-0.91)	0.91 (0.67-1.08)	0.68 (0.56-0.87)	0.043*
Uterine Artery PI, Left - MRI (IQR)	0.75 (0.60-0.94)	0.91 (0.70-1.43)	0.73 (0.56-0.84)	0.014*
Uterine Artery PI, mean - MRI (IQR)	0.75 (0.63-0.94)	0.95 (0.75-1.13)	0.70 (0.61-0.86)	0.006*
Total Uterine Artery Flow (mL/min) - MRI (IQR)	616.4 (451.8-748.1)	469.8 (356.4-630.4)	648.2 (480.6-755.4)	0.023*

Table 11 Demographic information for subjects with delivery and US info, divided into subsets COMP and no COMP. BMI=body mass index, CHTN=chronic hypertension, GDM=gestational diabetes mellitus, GA=gestational age, GHTN=gestational hypertension,
108

PEC=preeclampsia, SGA=small-for-gestational age, PI=pulsatility index, %=percentage, std=standard deviation, IQR=interquartile range (25%-75%), p-values reported from two-sample Wilcoxon rank-sum test, *p<0.05

6.2.4.2 MRI-flow with GA and Delivery Outcomes

Median total UtA blood flow (sum of left and right UtA flow) was 592 (IQR 441-742) mL/min in the 74 subjects. There was no correlation with GA (y=-0.47x+614.67, R^2<0.01, p=0.91). Fig. 34 shows a scatterplot of MRI-flow values along GA. The subject with IUFD imaged at 15 weeks gestation had lower flow than the other subjects at 109.5 mL/min with normal US-PI of 1.98 and MRI-PI of 1.92. When evaluating COMP and no COMP subjects separately, median UtA blood flow was 486.1 (IQR 598.2-366.1) mL/min in the 18 COMP subjects and 623.8 (IQR 456.6-748.6) mL/min in the 56 no COMP subjects. As a group, the COMP subjects had slightly lower flow than the no COMP group, particularly in the second trimester. No correlations between UtA flow and GA were found in the COMP group (y=6.14x+314.75, R^2=0.06, p=0.34) and no COMP group (y=1.20x+599.67, R^2<0.01, p=0.82). The two-sample Wilcoxon rank-sum test showed a reduction in MRI-flow in COMP subjects (p=0.04), with a trend towards reduction when examining PEC (p=0.08) and SGA (p=0.08) individually. Box-and-whisker plots of MRI-flow in the 74 subjects with delivery outcomes are available in Fig. 35. After adjusting for GA (at MRI) and CHTN, mean ± SD MRI-flow was 496.9 ± 54.6 mL/min in COMP and 635.0 ± 29.8 mL/min in no COMP subjects (p=0.03). In the 18 COMP subjects, there was an average of 40 ± 35 days between the imaging exam and delivery. In 16 of the 18 subjects, diagnoses of PEC and SGA were recorded at delivery.

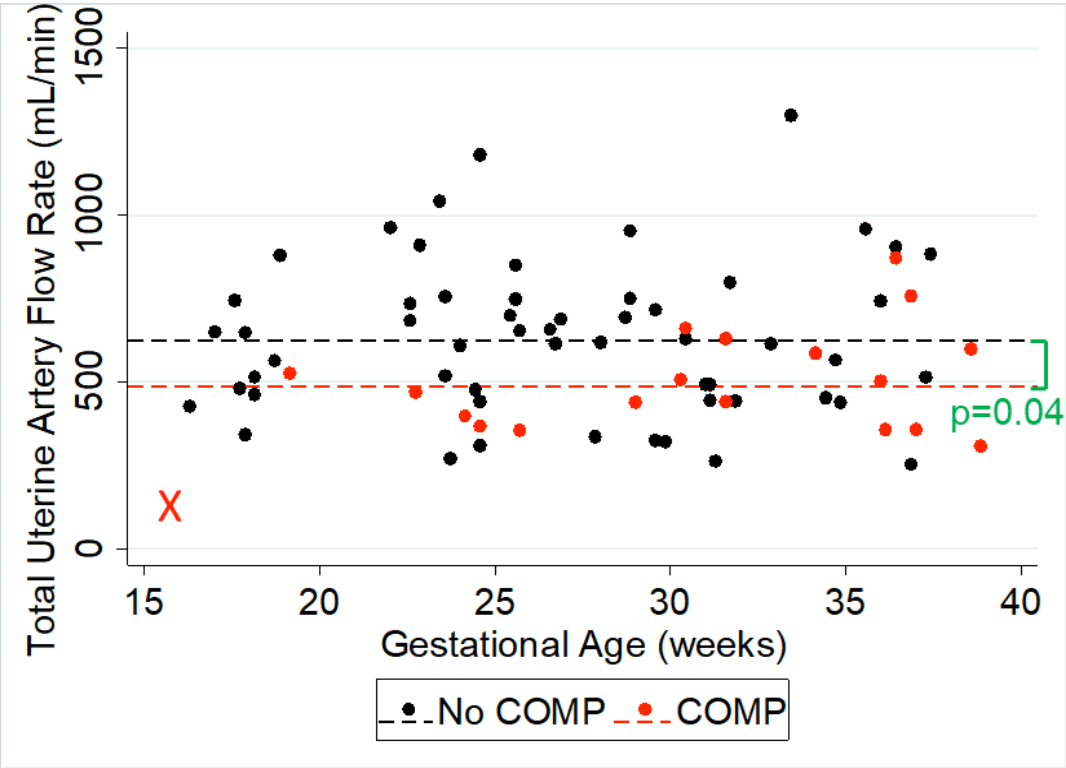

Figure 34 Scatterplot of MRI-flow vs. GA in 74 pregnant subjects with significantly lower median total uterine artery flow in no COMP compared to COMP subjects (dashed lines). Correlation was not found between MRI-flow and GA for all subjects, COMP, and no COMP. The red "X" indicates the total uterine artery flow of the IUFD subject for visual comparison.

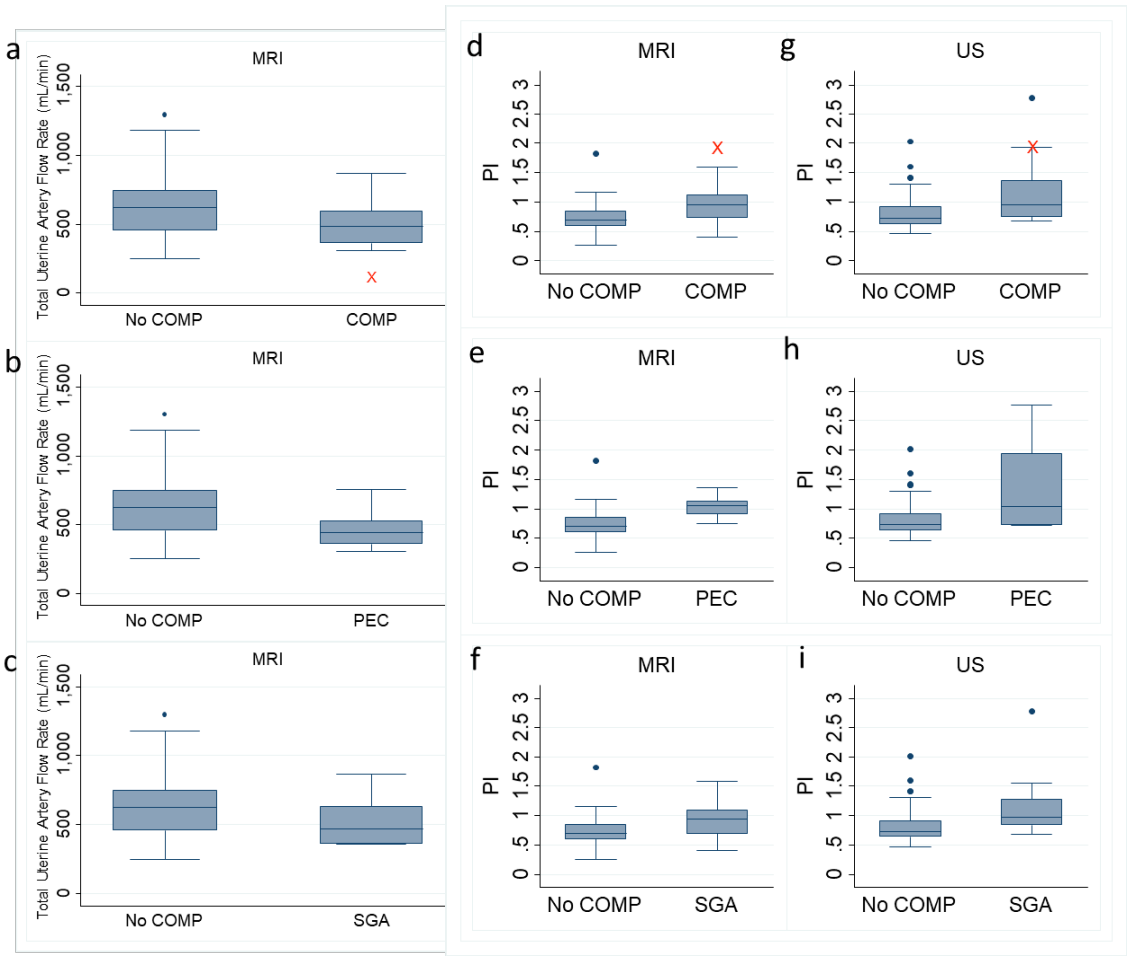

Figure 35 In the 74 subjects with delivery outcomes recorded, we present the box-and-whisker plots of MRI-flow showing difference in a) no COMP vs. COMP (p=0.04), b) no COMP vs. PEC (p=0.08), c) no COMP vs. SGA (p=0.08). In the 66 subjects with US data available, we present box-and-whisker plots showing difference in d,g) no COMP vs. COMP by MRI-PI (p<0.01) and US-PI (p<0.01), e,h) no COMP vs. PEC by MRI-PI (p<0.01) and US-PI (p=0.02), and f,i) no COMP vs. SGA by MRI-PI (p=0.03) and US-PI (p<0.01). Red "X" shows MRI-flow, MRI-PI, and US-PI for the IUFD subject.

6.2.4.3 MRI-PI and US-PI with Delivery Outcomes

A comparison between MRI-PI and US-PI showed a moderate Spearman's correlation with ρ=0.69 (p<0.01) and significant bias with median MRI-PI=0.75 (IQR 0.63-0.94) and median US-PI=0.78 (IQR 0.67-1.03) (p<0.01). Both MRI and US techniques were able to detect increased PI in the 15 subjects with COMP (out of 66 subjects) (MRI-PI: p<0.01; US-PI: p<0.01) (Fig. 35). These differences in both MRI and US PI remained significant when looking at PEC (MRI-PI: p<0.01; US-PI: p=0.02) and SGA (MRI-PI: p=0.03; US-PI: p<0.01) as individual outcomes as well. After adjusting for GA (at MRI and US) and CHTN, MRI-PI was 1.02 ± 0.07 for COMP and 0.72 ± 0.04 for no COMP (p<0.01); US-PI was 1.23 ± 0.1 for COMP and 0.81 ± 0.05 for no COMP (p<0.01).

6.2.4.4 MRI-flow, MRI-PI, and US-PI ROC Curves

The ROC AUCs provided by MRI-flow for no COMP, no PEC, and no SGA were 0.66, 0.69, and 0.64, respectively for the 74 subjects (Fig. 36). The AUC values from MRI-PI vs. US-PI for the following groups in the 66 subjects were also compared. Further, no significant difference was found between the two modalities: COMP (0.74 vs. 0.73, p=0.94), PEC (0.84 vs. 0.75, p=0.31), and SGA (0.69 vs. 0.75, p=0.40) (Fig. 37). In Fig. 38, the ROC curves from MRI-flow, MRI-PI, and US-PI were compared in the 66 subjects which show no significant difference in predicting COMP (p=0.87).

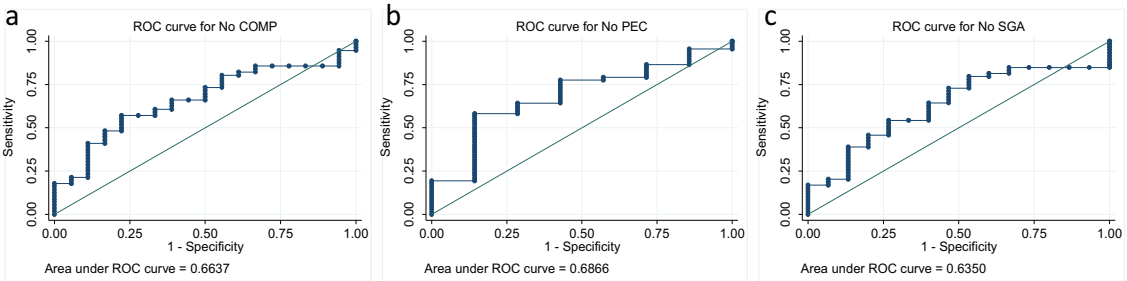

Figure 36 MRI-flow ROC curves for: a) no COMP with AUC=0.66, b) no PEC with AUC=0.69, and c) no SGA with AUC=0.64

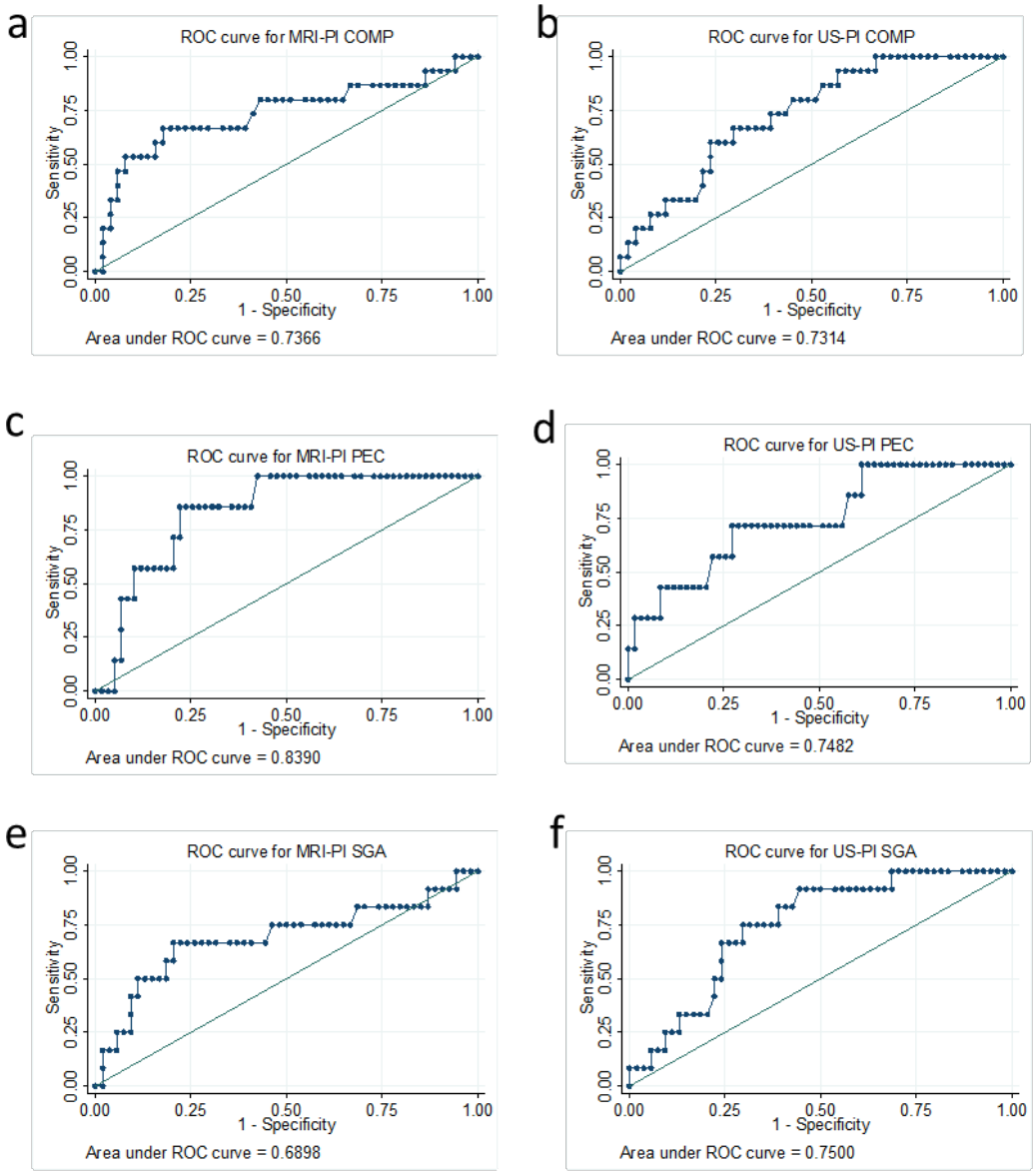

Figure 37 ROC curves from MRI-PI for a) COMP with AUC=0.74, c) PEC with AUC=0.84, and e) SGA with AUC=0.69. ROC curves from US-PI for b) COMP with AUC=0.73, d) PEC with AUC=0.75, and f) SGA with AUC=0.75.

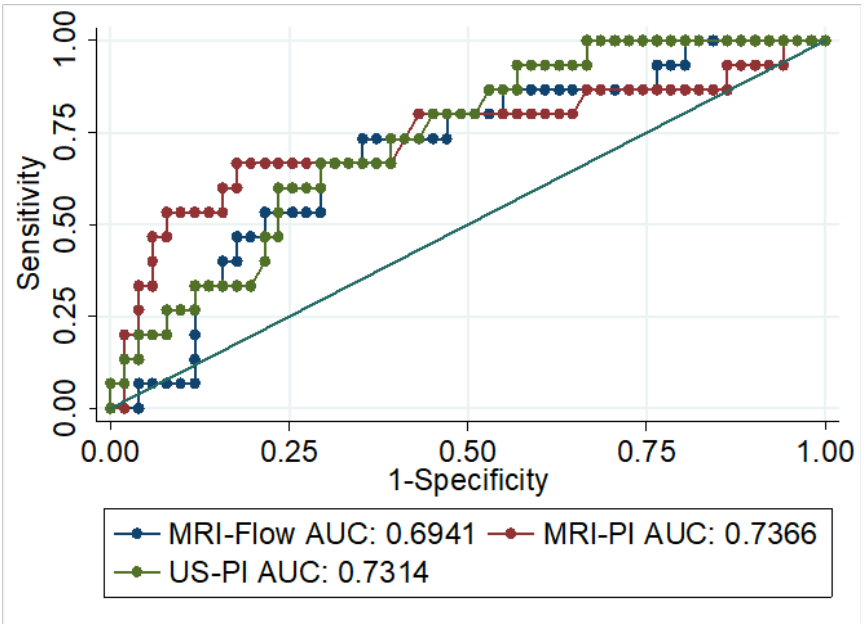

Figure 38 Comparison of the ROC curves from MRI-flow, MRI-PI, and US-PI in 66 subjects for COMP. They show no statistically significant difference (p=0.87).

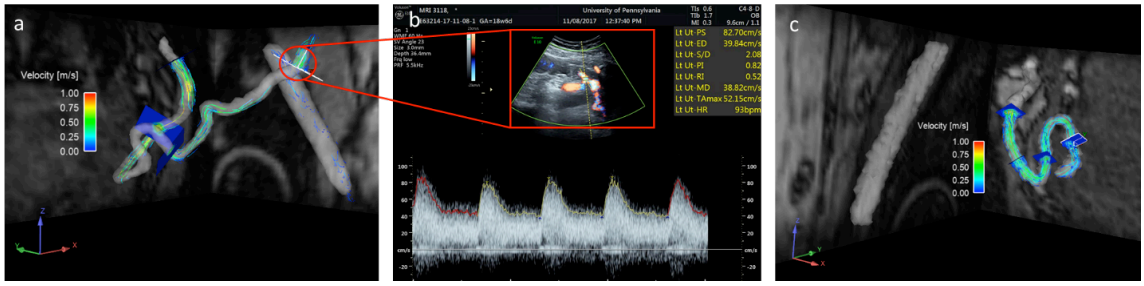

Figure 39 a) Example of healthy pregnant uterine artery 4D flow MRI pathlines, b) ultrasound of corresponding uterine artery with panel a, c) example of uterine artery 4D flow MRI in preeclamptic pregnancy

6.2.5 Discussion

The principal finding of this study is concordance between 4D flow MRI and US in distinguishing between pregnancies with no COMP and COMP. We successfully applied 4D flow MRI to the UtAs and found increased MRI-PI in pregnancies that went on to develop SGA and PEC [32, 178-

180], outcomes associated with impaired trophoblastic invasion. US-PI is used to measure UtA resistance as a reflection of downstream trophoblast invasion [96, 140, 141, 178]. As compared to US, 4D flow MRI provides the spatial coverage to visualize the length of the UtAs, measure lumen area, and decompose blood velocity in three orthogonal directions. In this study, both US and MRI-PI showed similar prediction of adverse outcomes based on ROC analysis. While US is more accessible, our data suggests that MRI-PI values are physiologically relevant, providing support for its continued development as a tool for assessing placental health.

We observed that MRI-flow was lower in COMP than no COMP subjects. The no COMP vs. PEC/SGA group comparisons showed the same trend but sample size may not have been large enough to demonstrate significance. Elevated UtA PI may be a concern during late pregnancy because high resistance limits delivery of oxygenated blood to the placenta [96, 140, 141]. UtA flow is a more direct measurement of perfusion than PI. We previously demonstrated the feasibility of measuring UtA flow during pregnancy with 4D flow MRI [150]. The one IUFD subject in our study was found to have low UtA flow despite normal MRI/US-PI compared to the cohort of live births. Our findings are consistent with the notion that reduced total UtA flow rate to the placenta is linked to poor pregnancy outcomes. While studies of US-based measurements of UtA flow have reported lower flow in PEC [181-184] and SGA [185, 186], technical challenges have precluded clinical use of US-based flow. US is more user-dependent than MRI and sensitive to body habitus, angle of insonation, and instrument gain artifacts. As lumen diameter is a significant contributor to accurate flow measurements, flow measurements may be difficult to reproduce since lumen walls may not be clearly resolved [181]. Furthermore, since the UtAs are often tortuous, absolute measures such as flow rate that depend on measurement angle are challenging to interrogate [181].

We did not observe a significant change in MRI-flow with GA, which we previously attributed to our subject population being imaged only in the second/third trimester [150], since prior work

suggested that most of the increase in UtA flow occurs in the first trimester [142, 183, 187]. However, several studies have also reported an increase in UtA flow measured by US in the second and third trimester [63, 155, 188, 189]. Our findings suggest that low MRI-flow measures are meaningful and associated with adverse pregnancy outcomes, though intersubject heterogeneity in our population may have weakened the MRI-flow vs. GA relationship in our cross-sectional study. Although the mean GA at MRI was significantly later for the COMP than no COMP group ($p<0.01$, Table 11), this did not mask the effect of significantly lower MRI-flow in COMP than no COMP ($p=0.04$). Since GA is a plausible confounder [63, 186], we adjusted the analysis for GA and significant group differences persisted ($p=0.03$).

In this study, US-PI showed an absolute positive bias over MRI-PI ($p<0.01$), consistent with our previous report [150], which can be attributed to MRI/US differences in spatiotemporal resolution, subject body positioning, and location of measurement along the UtA. Even though MRI-PI and

MRI-flow AUC performances were comparable to US-PI (Fig. 38), UtA Doppler is still largely an investigational tool. US-PI has been found to have inconsistent performance especially in first trimester pregnancy and unselected, low risk populations [18, 168]. In Fig. 39, we show an example of the 4D flow geometry and pathlines in healthy and PEC subjects. This approach has the advantage of deeper penetration and larger field-of-view, thus able to more comprehensively visualize the uterine vessels for localization.

4D flow MRI has been gaining clinical attention, showing utility in assessing various cardiovascular diseases [173]. For example, 4D flow MRI has been shown to measure wall shear stress (WSS), which can be utilized as a meaningful tool for assessing and managing intracranial aneurysms [190, 191]. For our purposes, the pathophysiology of PEC also involves inherent vessel wall dysfunction [32, 72, 139, 179, 192, 193]. Further development of 4D flow MRI for assessing the UtAs in pregnancy can lead to clinically impactful tools to aid in risk stratification,

identifying early signs of pathology, and guiding future clinical trials aimed at exploring potential preventive and treatment strategies.

Our study had a high percentage of COMP subjects (18/74, 24%) compared to the 10-15% prevalence of PEC and SGA in the general population, but this is expected because the University of Pennsylvania serves a community with a large population of black women, and black race is a risk factor for PEC/SGA [194]. One limitation of this study is that it is cross-sectional, making it difficult to distinguish between intersubject variability and gestational MRI-flow progression. Longitudinal studies can better characterize changes in UtA MRI-PI/flow. Another limitation is that the 4D flow MRI sequence used in this study had limited spatial (1.25x1.25x1.25 mm^3; ~3-4 voxels across the UtA diameter) and temporal resolution (42 ms), potentially limiting the accuracy of PI and flow rate measurements. We measured a median UtA flow of 623 mL/min in the no COMP subjects, which seemed lower than the values reported by US [63, 186] and 2D phase contrast MRI [124]. While it appeared possible that US overestimated mean velocity over the cross-sectional area by sampling the center of the vessel, we may have underestimated flow by using lower spatial and temporal resolution with a 1.5T rather than the 3T magnetic field strength used for 2D phase contrast MRI [124]. We believe this was a systematic bias that affected measurements in both COMP and no COMP subjects and we did demonstrate repeatability in a previous study [150]. Fortunately, substantial progress in 4D flow MRI is being made to decrease scan time and improve temporal and spatial resolution [195, 196]. We believe with optimization and technical improvements 4D flow MRI can potentially be useful earlier in gestation.

6.2.6 Conclusions

Effective methods to predict risk of adverse pregnancy outcome are critical to obstetric care. This study demonstrates that 4D flow MRI is comparable to Doppler US in measuring PI and additionally measures flow. Both PI and flow are able to distinguish between pregnancies with

PEC, SGA, or both and a reference group. 4D flow MRI is a technique that can serve as the foundation for more robust tools to better understand the hemodynamics of the UtAs during pregnancy.

CHAPTER 7: EXTENDED ANALYSIS OF MATERNAL PELVIC ARTERY GEOMETRY AND HEMODYNAMICS

7.1 Maternal cardiovascular system in HPD

Consistent with the placental origin hypothesis, some evidence indicates Research that UtA US is a better predictor of early-onset preeclampsia (diagnosed before 34 weeks or requiring delivery before 37 weeks) than other forms of HPD [139]. In contrast, the alternative maternal cardiovascular origin hypothesis may better explain late-onset preeclampsia and other forms of HPD for which UtA US does not perform as well [72]. It is possible that HPD results when a mother with cardiovascular disease has difficulty undergoing the significant changes in cardiac output, blood volume, systemic vascular resistance, and other processes to support the pregnancy. The fact that preeclampsia patients share many of the same risk factors, signs, and symptoms as cardiovascular disease patients motivates the value of investigating the maternal cardiovascular system beyond the uteroplacental network [197]. This chapter discusses two additional studies that analyze the images collected with 4D flow MRI of the uterine arteries to better understand the nature of uterine artery structure and hemodynamics. Unlike the previous chapters, which only discussed the placenta and uterine arteries alone, these studies expand the scope of the image assessment towards the entire maternal vascular network by also including descending aorta and external iliac arteries. Time-of-flight angiography (TOF) was performed for localization of the uterine arteries. However, because of the large field of view and high spatial resolution, centerline extraction could be extended to quantify length and curvature starting from the descending aorta to the uterine arteries and external iliac arteries. Furthermore, combining length information (TOF) and velocity information (4D flow and 2D phase contrast) in the maternal pelvic network enabled estimation of pulse wave velocity. Pulse wave velocity is relevant to HPD

research because it is a marker of arterial stiffness, which is a condition commonly suspected in HPD patients [32].

7.2 Centerline geometry characterizes tortuosity

7.2.1 Abstract

The uterine artery undergoes morphological changes during pregnancy, but little is known about the gestational progression of the tortuosity and how it is abnormal in HPD. This study developed an MRI-based technique to quantitatively characterize the length and curvature of the uterine arteries. Preliminary results show the unilateral length of the UtAs from the bifurcation of the internal and external iliac arteries to the most inferior point of the UtAs was 144.8±29.7 mm (range = 89.6-230.9 mm). The RMS curvature was found to be 0.125 ± 0.034 mm^{-1} (range = 0.064-0.2 mm^{-1}) within the same UtA segments. There was a decreasing trend between gestational age and RMS curvature from the bifurcation to the most inferior point of the UtA (R^2 = 0.1, p = 0.007). Geometric parameters characterizing the UtAs based on TOF angiography may ultimately provide clinically relevant biomarkers of aberrant remodeling in early gestation.

7.2.2 Introduction

During pregnancy, the maternal uterine arteries (UtAs) undergo vasodilation and elongation to accommodate the gravid uterus and match fetal demand for oxygen and nutrients [46]. Maternal arterial dysfunction is characteristic of pregnancy disorders such as preeclampsia [168] and patients have inward smooth muscle hypertrophy, increased wall thickness, and limited vasodilation at delivery [198]. However, there is limited quantitative information about temporal remodeling of UtAs. This information may add value to diagnosis and screening of hypertensive pregnancy disorders [46]. We have shown that noninvasive, non-contrast MRI is feasible for characterization of UtA anatomy and hemodynamics in humans [199]. Our objective was to

quantitatively describe the geometry of the pelvic arteries in healthy pregnant subjects using time-of-flight (TOF) MRI angiography. We hypothesize that the UtA lengthens and becomes more tortuous with gestational age.

7.2.3 Methods

TOF MRI data from 36 healthy pregnant subjects were analyzed (n=23 in the 2nd trimester, and n=13 in the 3rd trimester, gestational age range=16 to 39 weeks). The TOF parameters were: TR=394 ms, TE=4.4 ms, flip angle=50 degrees, and diastolic ECG-gating. The TOF angiogram was segmented, isosurfaces and centerlines were generated, and length and curvature were quantified (Fig. 40b). The centerline connected the center points of maximally-inscribed spheres, approximated by a Voronoi diagram, along the interior of the vessel. The curvature, κ, was defined as the reciprocal of the radius, r, of the osculating circle $\left(\kappa = \frac{1}{r}\right)$ tangent to the centerline in the normal direction using the Frenet reference system (Fig. 40c). Vessel curvature for an entire vessel was calculated using the root mean squared (RMS) curvature. Pearson's R correlation was performed to test for linear correlations between path length, RMS curvature, and gestational age.

7.2.4 Results

Figure 41a shows the centerline and UtA curvature histograms of a representative subject (Fig. 41b,c). The UtAs formed a tortuous structure, looped superiorly, and crossed the external iliac arteries towards the placenta at the fundus of the uterus. The unilateral length of the UtAs from the bifurcation of the internal and external iliac arteries to the most inferior point of the UtAs was 144.8±29.7 mm (range = 89.6-230.9 mm). An increasing trend was observed (R^2 = 0.04, p = 0.08) between gestational age and unilateral length (Fig. 42a). The RMS curvature was found to be 0.125 ± 0.034 mm-1 (range = 0.064-0.2 mm-1) within the same UtA segments. There was a

decreasing trend between gestational age and RMS curvature from the bifurcation to the most inferior point of the UtA (R^2 = 0.1, p = 0.007; Figure 42b).

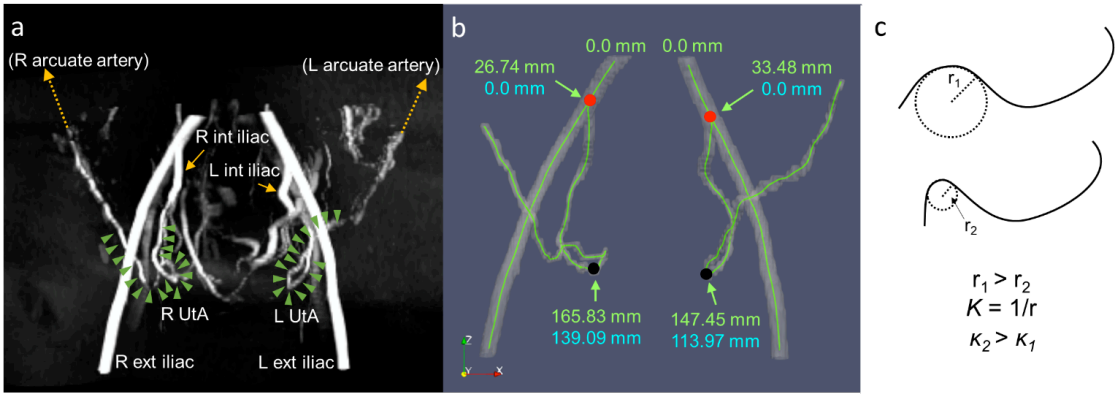

Figure 40 a) 3D maximum intensity projection of the TOF angiogram in a representative subject. The green arrowheads delineate the UtAs after branching from the internal iliac arteries. b) The isosurface rendering and centerline extraction of the same subject. Red dots represent the starting landmarks at the bifurcation of the internal and external iliac arteries. Black dots represent the ending landmarks at the most inferior point of the UtAs. The path length and root mean squared curvature reported in this study are calculated from the blue coordinates. C) Diagram of how curvature is computed based on the tangent osculating circle to a curve. The more tortuous curve has a smaller radius (r) and higher curvature (κ).

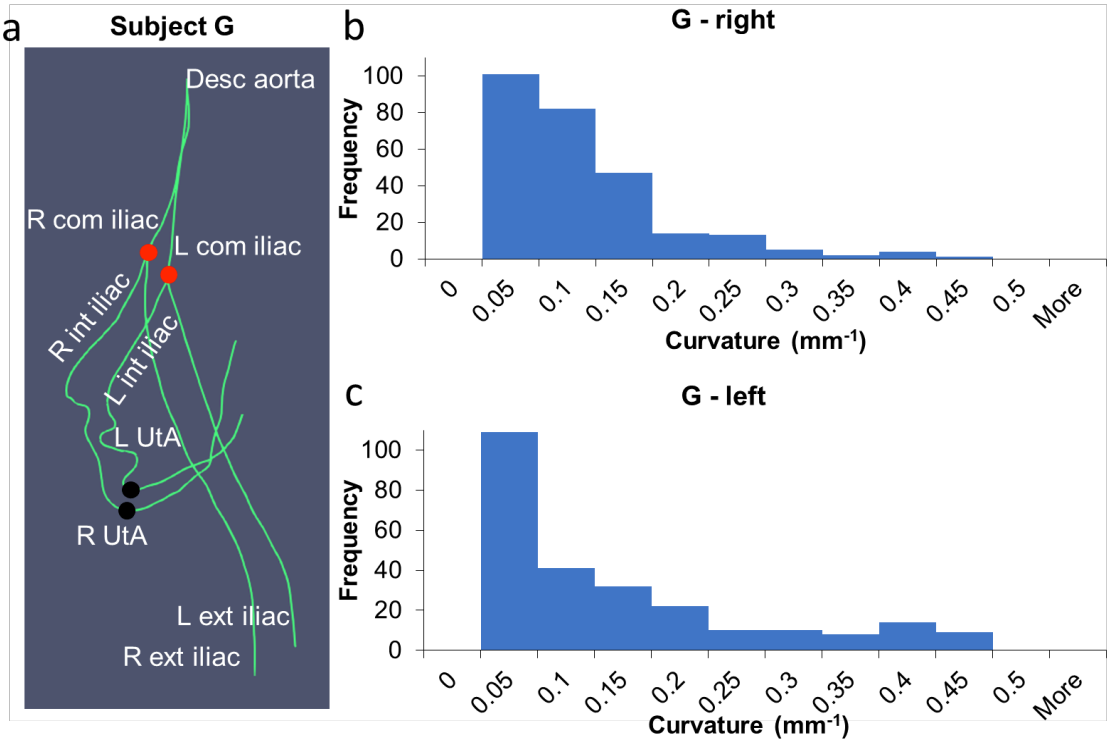

Figure 41 a) Centerlines of a representative subject with difference in tortuosity between the left and right UtA. It extends from the descending aorta through the common iliac arteries, internal iliac arteries, UtAs, and external iliac arteries. Red dots represent the starting landmarks at the bifurcation of the internal and external iliac arteries. Black dots represent the ending landmarks at the most inferior point of the UtAs. The curvature histogram of the right UtA (b) has a narrower distribution than the left UtA (c).

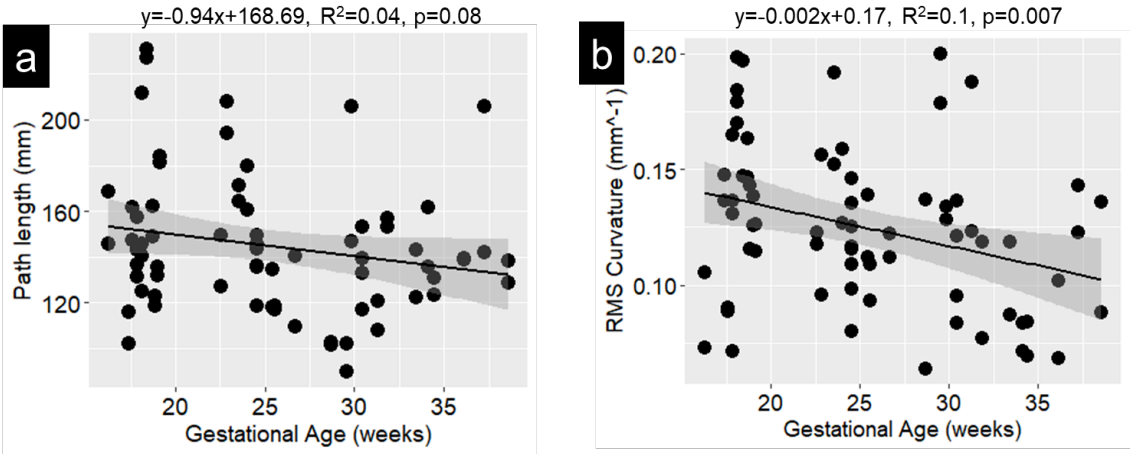

Figure 42 a) Plot with linear correlation results showing decreasing trend in path length over gestational age (GA) in the left UtA and right UtA. b) Plot with linear correlation results showing curvature with decreasing trend with gestational age (GA) in the left UtA and right UtA.

7.2.5 Discussion

This study demonstrated quantitative characterization of UtA length and curvature geometry using TOF MRI angiography. Curvature was found to be a quantitatively meaningful descriptor of UtA tortuosity and could differentiate bilateral UtA anatomical heterogeneity. This may reflect variations in placental location, viability and distal uterine and spiral arterial remodeling. Additionally, this study provided important preliminary data regarding the association between UtA length, curvature and gestational age. It was expected that the UtA path length would increase during angiogenesis and become more tortuous to accommodate fetal growth and decreasing blood flow pulsatility. However, we saw a decrease in length and curvature, which may be because the uterine artery was originally coiled and the expanding uterus causes it to uncoil. UtA remodeling is believed to rapidly occur within the first two trimesters to anticipate increased fetal oxygen and metabolic demand, tapering off by 3rd trimester [46, 200]. We observed that path length and curvature vary considerably with laterality. Future work will investigate curvature and tortuosity in patients with adverse pregnancy outcomes.

7.2.6 Conclusions

The major contributions of this study are 1) the development of an approach to measuring length and curvature of the UtAs, and 2) trends toward UtA path length shortening and decreased tortuosity with gestational age. Additional subjects will confirm that these trends are consistent with UtA remodeling in animals [46]. This approach is applicable to studying UtA remodeling early in pregnancy and can be used to investigate the relationship between vascular geometry and hemodynamics.

7.3 Pulse wave velocity characterizes arterial stiffness

7.3.1 Abstract

Maintenance of blood supply to the placenta is believed to be dependent on the geometric and hemodynamic properties of the uteroplacental vasculature. In this study we present an MRI method for measuring pulse wave velocity in the uterine arteries. In 6 healthy pregnant subjects, we measured path length and time-to-peak of the velocity waveforms in the uterine arteries and external iliac arteries. The uterine arteries have lower pulse wave velocity than the external iliac arteries (5.5±2.5 vs. 12.9±4.6 m/s, $p=3x10^{-5}$), suggesting biomechanically greater compliance.

7.3.2 Introduction

After successfully showing feasibility in human pregnancy, we sought to extend the 4D flow MRI analysis technique by estimating pulse wave velocity (PWV) in the UtAs. UtA remodeling is believed to involve increasing arterial compliance to reduce blood flow resistance to the placenta [138] based on flow-mediated dilation studies and animal models [60, 201-203]. A limitation of ultrasound-based flow-mediated dilation studies is their inability to visualize the UtAs beyond 3-4 cm in length at a time. In this study, we leveraged time-of-flight (TOF) and 4D flow MRI to measure and compare PWV measured from the descending aorta (dAo) to the UtAs and external

iliac arteries (EIAs). To our knowledge, 4D flow MRI measurements of PWV in the UtAs in human pregnancy have not yet been reported. We hypothesized that the UtAs would have lower PWV than the EIAs.

7.3.3 Methods

We acquired TOF and 4D flow MRI in 6 healthy singleton pregnant women (gestational age (GA)=18-25 weeks) at 1.5T (Avanto; Siemens Healthcare, Erlangen, Germany). They were imaged in supine position with 8-channel spine array, two 4-channel body array coils, electrocardiogram synchronization. The MRI protocol consisted of a half-Fourier acquisition stimulated echo (HASTE) to localize the pregnant uterus, TOF angiogram from the dAo to the femoral heads of the thigh bones, 2D phase contrast velocimetry at the dAo, and 4D flow of the UtAs (total acquisition time=30-40 min). The TOF parameters were: repetition time (TR)/echo time (TE)=394/4.4 ms, flip angle (FA)=50º, field-of-view (FOV)=350x250x190 mm^3, voxel size=1.1x1.1x2.8 mm^3. The 4D flow parameters were: TR/TE=5.5/2.8 ms, FA=8º, FOV=320x240x60 mm^3, voxel size=1.25x1.25x1.25 mm^3, PEAK-GRAPPA acceleration factor=4.7 [145], velocity encoding parameter (VENC)=120-160 cm/s [22], number of cardiac phases=10-18. The TOF angiograms were segmented (Seg3D; Univ. of Utah SCI) and centerlines were extracted (VMTK) to compute path length (PL) from the dAo to the UtAs and EIAs. The 4D flow images were processed with custom software (MATLAB) [147] and volumetric velocity-based thresholding (Ensight, CEI; Apex, NC). Eight planes were prescribed in each vessel and time-to-peak (TTP) was computed from the velocity waveform extracted from each plane. PWV was computed by PWV=PL/TTP [m/s]. We used box-and-whisker plots, two-tailed paired t-test, and two-way ANOVA to compare the PWV results.

7.3.4 Results

Figure 43 shows the dAo, EIA and UtA blood velocity in one subject at 18 weeks gestation. Across all subjects, PWV was 5.5±2.5 m/s (mean±std) in the UtAs and 12.9±4.6 m/s in the EIAs ($p=3x10^{-5}$). The difference in PWV was 7.4 m/s with 95% confidence interval [5.2,9.6] m/s. Figure 44 shows that the UtAs have lower PWV than the EIAs. When comparing PWV measurements between vessel type (UtA vs. EIA) and laterality, there was an effect of vessel type ($p=3x10^{-4}$) but not in laterality (p=0.42). The UtA and EIA diameters were 6.2±0.7 mm and 8.2±1.0 mm ($p=1x10^{-4}$), respectively. Table 12 contains the data for each subject.

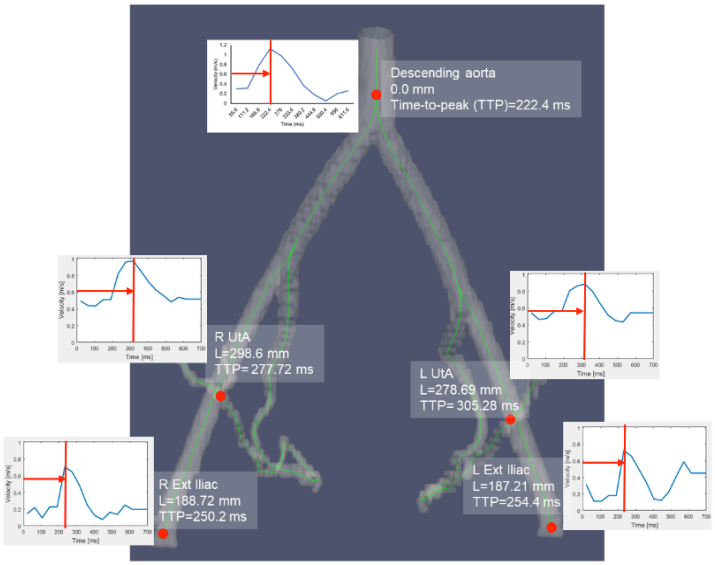

Figure 43 Vessel isosurface including the descending aorta, UtAs, and EIAs in a subject at 18 weeks gestational age. Only one 2D phase contrast measurement was obtained at the descending aorta. The remaining red dots indicate approximate locations at which eight planes were extracted from the 4D flow acquisition. Path length (PL) and time-to-peak (TTP) were computed and normalized to the reference measurement in the descending aorta to calculate PWV.

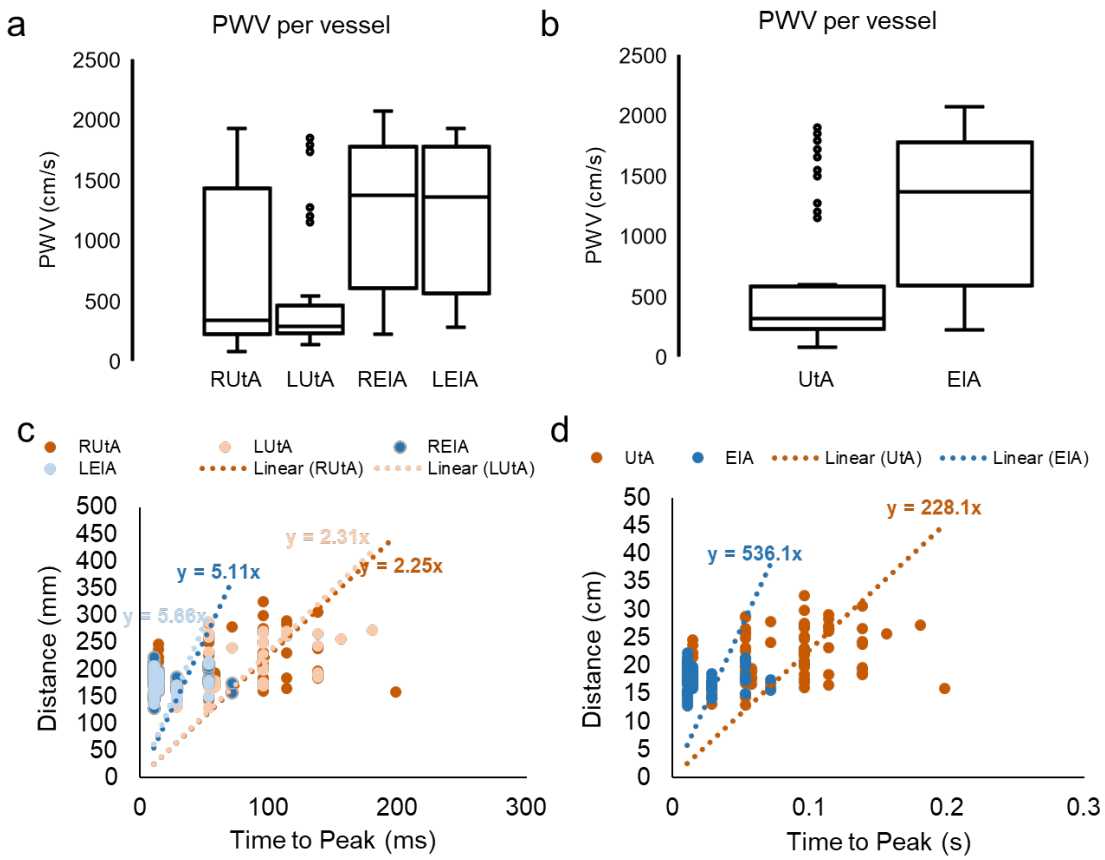

Figure 44 a) Box-and-whisker plot of individual left and right UtAs and EIAs, b) box-and-whisker plot of UtAs and EIAs with left and right sides averaged together, c) scatter plot with linear fit of individual left and right UtAs and EIAs, d) scatter plot with linear fit of UtAs and EIAs with left and right sides averaged together.

			UtA			EIA		
Subject	GA (wks)	Laterality	PL (cm)	TTP (ms)	PWV (m/s)	PL (cm)	TTP (ms)	PWV (m/s)
A	18.9	R	19.9	69.1	4.2	15.8	16.1	13.0
		L	20.1	79.7	2.6	16.1	21.4	11.8
B	18.7	R	23.4	79.7	6.1	19.7	37.3	9.2
		L	21.1	69.1	5.0	19.3	26.7	12.7
C	19.1	R	20.7	25.2	11.9	18.1	14.4	12.6
		L	17.6	30.6	8.8	18.2	14.4	12.6
D	22.9	R	22.5	53.2	9.0	20.4	10.8	18.9
		L	24.0	85.0	5.0	20.0	16.1	16.5
E	24.6	R	22.1	108.1	2.6	17.0	39.2	5.1
		L	22.1	92.2	2.7	15.7	28.6	5.5
F	24.6	R	20.8	63.8	8.3	18.6	10.8	17.2
		L	22.0	85.0	4.6	18.3	16.1	15.3
Mean±std:			**21.4±1.7**	**70.1±24.2**	**5.9±3.0**	**18.1±1.6**	**21.0±9.8**	**12.5±4.3**

Table 12 Details of each subject. It appears that the longer TTP in the UtA compared to the EIA is a major contributing factor to the smaller PWV. GA=gestational age, PL=path length, TTP=time to peak, PWV=pulse wave velocity

7.3.5 Discussion

We found that the UtA PWV was lower than EIA PWV between 18-25 weeks of pregnancy. According to the Moens-Korteweg equation, this would indicate reduced UtA wall compliance or wall thickness compared to the EIAs. We speculate PWV decreases with time as UtA wall compliance increases with gestational remodeling [60]. This response is important in maintaining low blood flow resistance and high flow rate to the placenta [60]. PWV can potentially be used to monitor UtA hemodynamics in patients with high risk of hypertensive disorders of pregnancy, which are believed to reflect systemic endothelial dysfunction [202, 203]. A limitation of 4D flow is its low temporal resolution compared to the EIA pulse wave transit time (Δt=40 vs. TTP=21 ms). This was mitigated by selecting a large distance between the reference (dAo) and the UtA/EIA locations, and measuring PWV at several UtA/EIA locations. Nevertheless, we found that EIA PWV was slightly higher than previous US studies (9.4-9.8 m/s) [38, 39], which may imply a combination of inaccurate spatial distance measurements in US and low temporal resolution. A further limitation of this study is that it assumes inviscid flow since there is no dependence on

viscosity [204]. Finally, differences in radius between the EIA and UtA may also have contributed to this trend since the UtAs have a smaller radius than the EIAs. In future work, fluid dynamic simulations and increase in spatial resolution of 4D flow would aid in better understanding of the viscous interactions between the blood flow and the arterial wall. A longitudinal study can better investigate the change in UtA PWV with gestational age.

7.3.6 Conclusions

The major contribution of this work is a joint structural-functional approach to assessing PWV in pregnant women. Physiologic changes in the female pelvic vasculature are believed to reflect pregnancy health during the course of gestation. Therefore, PWV may be a potential biomarker of UtA remodeling during clinical monitoring for adverse pregnancy outcomes.

CHAPTER 8: CONCLUSIONS, LIMITATIONS, AND FUTURE DIRECTIONS

8.1 Conclusions

Today, the mechanisms of HPD are under investigation and early prediction of adverse pregnancy outcomes continues to be a challenge. This motivates researchers to continue developing technologies that can noninvasively study human placental physiology and to provide biomarkers that can be used in clinical diagnosis and management. This dissertation contributes to this effort by exploring how current MRI flow and perfusion methods already successful in the brain and cardiovascular system can be applied to the uteroplacental circulation. The evidence presented in this thesis shows the feasibility of MRI in human pregnancy by addressing challenges such as motion and extracting functional information from small vessels. These studies also explored innovative ways to characterize the uteroplacental structure and function by developing visualizations and metrics based on these imaging techniques.

Chapter 4 described the application of arterial spin labeling (ASL) to the placenta, the key organ of nutrient exchange between the mother and fetus. However, placental MRI is susceptible to motion artifacts from respirations, contractions, and fetal movement. This study of FAIR ASL was affected by these artifacts, but it showed promise as images processed by traditional methods demonstrated the expected pattern of perfusion. After establishing the feasibility of placental ASL, the need for a novel pattern analysis approach to more accurately capture the unique physiology of the placenta was identified. The combination of Bayesian statistics, spline-based coordinate transformation, and cluster analysis showed blood distribution aggregates reminiscent of the known lobular structure of the placenta. This work opens the door for future investigation in the ability of ASL cluster analysis to distinguish between hypertensive and normal pregnancies.

In response to the numerous uterine artery Doppler flow velocimetry studies to evaluate pregnancy health, especially the risk of HPD, Chapter 5 described the application of 4D flow MRI to the uterine arteries in human pregnancy. 4D flow MRI enabled 3D pathline visualization of blood flow in the tortuous vessels, extraction of time-resolved 2D velocity fields at vessel cross sections, calculation of flow rate, pulsatility index (PI), and resistivity index (RI). By comparison, corresponding ultrasound PI and RI moderately agreed with MRI. The other information such as flow rate were believed to be more reliable in MRI and generate interest in further investigation of complex flow properties that may be more physiologically relevant than PI and RI (Chapter 7).

Chapter 6 correlated information from 4D flow MRI of the uterine arteries with pregnancy outcomes to see if this technique can detect the difference between preeclampsia/small for gestational age and normal pregnancies. It was shown to perform successfully and similarly to ultrasound PI. This establishes the validity of 4D flow MRI and the value of further technical improvement to leverage the additional complex hemodynamic information unique to this method for HPD research.

Chapter 7 explored cardiovascular physiology extending beyond the uteroplacental vessels. Time-of-flight (TOF) MRI angiography originally used for localization of the uterine artery also captured a large field of view including the descending aorta through the external iliac arteries/uterine arteries. It was also apparent that the uterine arteries had a unique tortuous structure that was probably an adaptation to the expanding uterus. To aid exploration, centerline extraction from the TOF MRI was performed and followed by calculation of path length and curvature. Path length information combined with velocimetry of the aorta (2D phase contrast MRI) and uterine artery/external iliac artery (4D flow MRI) enabled estimation of pulse wave velocity (PWV). Since arterial stiffness of endothelial dysfunction has been identified as a potential biomarker of HPD and PWV is known to be related to arterial stiffness, this technique of measuring PWV was developed to examine possible correlation with adverse pregnancy

outcomes. Results show promise as PWV was found to be higher in the external iliac arteries than the uterine arteries, which is consistent with the expectation that the former vessels would be stiffer.

8.2 Limitations

There are several limitations to the version of ASL presented in Chapter 4. First, the sequence was a 2D multislice technique that had a 2.5 mm slice gap and only four 10 mm slices, which meant that there was incomplete coverage of the placenta. An accelerated 3D version of ASL would be needed to assess the entire intervillous space for maternal vascular malperfusion abnormalities. Second, the post-label delay time points were sparse, only 2 to 4 points between 500 to 2000 ms. By these times, most of the blood has reached steady state in the intervillous space. To capture perfusion dynamics, shorter post-label delays would have been needed (<150 ms). Third, this study was conducted at 1.5 T MRI field strength, which compared to 3T limited the amount of perfusion signal distinguishable from physiological noise. Fourth, there was a small sample size when correlating adverse pregnancy outcomes with the cluster based metrics, so a larger sample size would be needed to confirm that the cluster metrics are related to placental health.

One of the limitations of the UtA 4D flow MRI studies presented in Chapter 5 and Chapter 6 was that it was cross-sectional, which made the results vulnerable to physiologic variation (e.g. height, weight, and internal iliac branching geometry). This can be mitigated with a longitudinal study to track flow changes over time for each subject. Also, the accuracy of 4D flow MRI assessment of UtA function may have been limited by UtA tortuosity, causing MRI acceleration and displacement artifacts. The findings were also limited by spatial resolution. Even when the UtA was visible in pregnant subjects, three voxels spanned the vessel at best, which did not allow the calculation of interesting complex hemodynamic parameters such as pressure gradient or wall

shear stress. Limited temporal resolution also made it difficult to identify detailed features of the UtA velocity waveforms such as diastolic notch in ultrasound.

The centerline extraction and pulse wave velocity studies described in Chapter 7 were proof-of-concept and had several limitations. The centerline geometry did not contain the other branches of the internal iliac arteries which may be important for understanding the structure of the UtAs relative to the other vessels. The path lengths were denoted as ending at the most inferior point of the "hairpin loop" of the UtAs before they ascended along the side of the uterus, but this missed part of the tortuous segment immediately after the inferior point. The end point may have also been slightly arbitrary because the extent of the visible UtAs transitioning to arcuate arteries was limited by vessel size and time-of-flight MR image quality. The path length and curvature versus gestational age correlations may have been confounded by other factors including maternal height, maternal weight, fetal weight, and body habitus during MRI scan.

A limitation of the PWV study was that the time shift of the UtA and external iliac artery velocity waveforms relative to the aorta velocity waveform was calculated based on peak velocities. Ideally the time shift should be measured between the "foot" (minimum velocity immediately after the peak) of each waveform in order to avoid wave reflections interfering with the time shift of the forward wave. However, this was not feasible with the current 4D flow MRI sequence because of low temporal resolution. Another consequence of low temporal resolution was that a large distance between the starting and the end velocity measurements was required to estimate global PWV. Therefore, even though the aorta, UtAs, and external iliac arteries were expected to have different vessel wall properties, local PWV could not be calculated with this technique. Both centerline extraction (path length and curvature) and PWV studies did not have a gold standard to evaluate accuracy.

8.3 Future Directions

Placental ASL MRI can be further improved upon by implementing 3D full coverage of the placenta using simultaneous multi slice imaging and by performing studies at 3 Tesla to increase sensitivity [24]. This would allow three-fold acceleration of the scan to acquire the images in a reasonable amount of time while capturing perfusion dynamics with multiple post-label delays. To mitigate the risk of slice order introducing bias into the ASL image contrast, slice shuffling can be used to average out these slice order effects. New labeling strategies can be tested to see if they can overcome the inflexible localization of labeled blood, the main limitation in FAIR ASL. Also, the ASL-related patterns can be correlated with placental oxygenation techniques such as BOLD MRI and T2* mapping. The placental pattern analysis can be improved upon by parameterizing the distance from the maternal to fetal side. This would make blood distribution characterization more precise when comparing between subjects. For validation, the in vivo patterns captured by ASL MRI could be mapped to post-delivery placental pathological features. In HPD, the key signs of maternal vascular malperfusion include placental hypoplasia, accelerated villous maturation, and decidual arteriopathy.

The UtA 4D flow MRI can be improved by conducting a longitudinal study to distinguish between intersubject variability and gestational MRI-flow progression. The MRI sequence can be accelerated using recent innovations such as 3D radial readout trajectory [195], spiral trajectory [205], and compressed sensing [205]. A shorter scan time (<10 min.) increases comfort for the pregnant subject lying supine and decreases the risk of motion introducing artifacts in the images. Acceleration can also achieve better image quality, reaching 15 ms temporal resolution and <1x1x1 mm^3 spatial resolution. Also, since the prospective gating causes the scan to miss some end-diastolic cardiac phases per cycle, implementing retrospective reconstruction can lead to more accurate calculations of hemodynamic parameters. These improvements may allow 4D flow MRI to be more suitable for assessing the UtAs earlier in gestation.

There are various ways to improve upon the time of flight MRI centerline analysis of the maternal pelvic arteries. The main limitation of the current study was that the path length and curvature versus gestational age analyses were cross-sectional and therefore susceptible to confounding factors. These factors include maternal height, maternal weight, fetal weight, and body habitus during MRI, which should be considered in a future study because they can potentially affect uterine artery path length and curvature. A future longitudinal study of how path length and curvature change over gestation in each subject may help better understand the involvement of vessel geometry in the physiological adaptation of pregnancy without interference of intersubject variability. Additional MRI vessel wall imaging of the uterine arteries can enable investigation of the vessel wall changes involved during gestation. A recent study [206] reported mathematical modeling of the spiral geometry of the spiral arteries to simulate its effect on flow rate and resistance. It was found that increased complexity in the structure of the vessel increased resistance to flow while decreasing flow rate. Similar analysis can be applied to the uterine arteries to better understand the physiological remodeling process during pregnancy.

Improvements can be made to the PWV study. In the future, ultrasound-based measurement of PWV can be used as a baseline reference to validate MRI-based PWV. Alternatively, a repeatability of the 4D flow MRI-based PWV can be used to test for robustness of the method. The main concern of the 4D flow MRI sequence was the low temporal resolution, so future studies should leverage state-of-the-art acceleration and reconstruction techniques to reduce measurement error. An experimental phantom such as the one described by Ruesink et. al. [207] can be used to model uterine artery mechanical properties to monitor their effect on hemodynamics including PWV. Computational fluid dynamics can also serve a similar purpose by modeling the uterine artery geometry, mechanical properties, and hemodynamics computationally.

8.4 Summary

This dissertation describes the application of ASL and 4D flow MRI to investigate the blood supply to the placenta during pregnancy. ASL MRI was found to be sensitive to blood flow patterns in the placenta that were consistent with structure of the intervillous space and lobular arrangement. 4D flow MRI was found to successfully measure flow rate in the uterine arteries, a parameter which was predictive of adverse pregnancy outcomes. Path length, curvature, and PWV of uterine arteries were additional parameters that were found to be measurable with MRI. They can potentially be relevant biomarkers of HPD. MRI is a noninvasive technique that offers potential to better characterize the physiological changes in pregnancy and, with further development, become a useful clinical tool for risk assessment in HPD.

BIBLIOGRAPHY

[1] "Report of the National High Blood Pressure Education Program Working Group on High Blood Pressure in Pregnancy," *Am J Obstet Gynecol,* vol. 183, no. 1, pp. S1-S22, Jul 2000.

[2] C. V. Ananth, K. M. Keyes, and R. J. Wapner, "Pre-eclampsia rates in the United States, 1980-2010: age-period-cohort analysis," *BMJ,* vol. 347, p. f6564, Nov 07 2013.

[3] K. Fingar, I. Mabry-Hernandez, Q. Ngo-Metzger, T. Wolff, C. Steiner, and A. Elizhauser, "Delivery Hospitalizations Involving Preeclampsia and Eclampsia, 2005-2014," in "HCUP Statistical Brief #222," Agency for Healthcare Research and Quality, Rockville, MD. April 2017, Available: www.hcup-us.ahrq.gov/reports/statbriefs/sb222-Preeclampsia-Eclampsia-Delivery-Trends.pdf.

[4] L. C. Liu, Y. C. Wang, M. H. Yu, and H. Y. Su, "Major risk factors for stillbirth in different trimesters of pregnancy--a systematic review," *Taiwan J Obstet Gynecol,* vol. 53, no. 2, pp. 141-5, Jun 2014.

[5] C. H. Backes, K. Markham, P. Moorehead, L. Cordero, C. A. Nankervis, and P. J. Giannone, "Maternal preeclampsia and neonatal outcomes," *J Pregnancy,* vol. 2011, p. 214365, 2011.

[6] I. Craici, S. Wagner, and V. D. Garovic, "Preeclampsia and future cardiovascular risk: formal risk factor or failed stress test?," *Ther Adv Cardiovasc Dis,* vol. 2, no. 4, pp. 249-59, Aug 2008.

[7] L. D. Levine, M. A. Elovitz, M. Limaye, M. D. Sammel, and S. K. Srinivas, "Induction, labor length and mode of delivery: the impact on preeclampsia-related adverse maternal outcomes," *J Perinatol,* vol. 36, no. 9, pp. 713-7, Sep 2016.

[8] Y. Dai and J. Ge, "Clinical use of aspirin in treatment and prevention of cardiovascular disease," *Thrombosis,* vol. 2012, p. 245037, 2012.

[9] D. L. Rolnik *et al.*, "Aspirin Versus Placebo in Pregnancies at High Risk for Preterm Preeclampsia," (in English), *Obstetrical & Gynecological Survey,* vol. 73, no. 1, pp. 11-12, Jan 2018.

[10] G. J. Hofmeyr, L. Duley, and A. Atallah, "Dietary calcium supplementation for prevention of pre-eclampsia and related problems: a systematic review and commentary," *Br J Obstet Gynaecol,* vol. 114, no. 8, pp. 933-43, Aug 2007.

[11] G. J. Hofmeyr, T. A. Lawrie, A. N. Atallah, and M. R. Torloni, "Calcium supplementation during pregnancy for preventing hypertensive disorders and related problems," *Cochrane Database Syst Rev,* vol. 10, p. CD001059, Oct 1 2018.

[12] R. N. Taylor, J. M. Roberts, F. G. Cunningham, and M. D. Lindheimer, Eds. *Chesley's Hypertensive Disorders in Pregnancy*, Fourth Edition ed. Waltham, MA: Elsevier Inc., 2015.

[13] J. V. Ilekis *et al.*, "Placental origins of adverse pregnancy outcomes: potential molecular targets: an Executive Workshop Summary of the Eunice Kennedy Shriver National Institute of

Child Health and Human Development," *Am J Obstet Gynecol,* vol. 215, no. 1 Suppl, pp. S1-S46, Jul 2016.

[14] C. M. Koopmans *et al.*, "Induction of labour versus expectant monitoring for gestational hypertension or mild pre-eclampsia after 36 weeks' gestation (HYPITAT): a multicentre, open-label randomised controlled trial," *Lancet,* vol. 374, no. 9694, pp. 979-988, Sep 19 2009.

[15] M. Y. Tan *et al.*, "Screening for pre-eclampsia by maternal factors and biomarkers at 11-13 weeks' gestation," *Ultrasound Obstet Gynecol,* vol. 52, no. 2, pp. 186-195, Aug 2018.

[16] A. Wright, D. Wright, A. Syngelaki, A. Georgantis, and K. H. Nicolaides, "Two-stage screening for preterm preeclampsia at 11-13 weeks' gestation," *Am J Obstet Gynecol,* vol. 220, no. 2, pp. 197 e1-197 e11, Feb 2019.

[17] D. Wright *et al.*, "Predictive performance of the competing risk model in screening for preeclampsia," *Am J Obstet Gynecol,* vol. 220, no. 2, pp. 199 e1-199 e13, Feb 2019.

[18] S. Parry *et al.*, "Role of early second-trimester uterine artery Doppler screening to predict small-for-gestational-age babies in nulliparous women," *Am J Obstet Gynecol,* vol. 217, no. 5, pp. 594 e1-594 e10, Nov 2017.

[19] A. E. Guttmacher, Y. T. Maddox, and C. Y. Spong, "The Human Placenta Project: placental structure, development, and function in real time," (in English), *Placenta,* vol. 35, no. 5, pp. 303-4, May 2014.

[20] B. Issa *et al.*, "Quantification of blood velocity and flow rates in the uterine vessels using echo planar imaging at 0.5 Tesla," *J Magn Reson Imaging,* vol. 31, no. 4, pp. 921-7, Apr 2010.

[21] R. A. Hawkes *et al.*, "Uterine artery pulsatility and resistivity indices in pregnancy: Comparison of MRI and Doppler US," *Placenta,* vol. 43, pp. 35-40, Jul 2016.

[22] M. Markl, A. Frydrychowicz, S. Kozerke, M. Hope, and O. Wieben, "4D flow MRI," *J Magn Reson Imaging,* vol. 36, no. 5, pp. 1015-36, Nov 2012.

[23] P. A. Gowland *et al.*, "In vivo perfusion measurements in the human placenta using echo planar imaging at 0.5 T," (in English), *Magnetic Resonance in Medicine,* vol. 40, no. 3, pp. 467-473, Sep 1998.

[24] X. Shao *et al.*, "Measuring human placental blood flow with multidelay 3D GRASE pseudocontinuous arterial spin labeling at 3T," *J Magn Reson Imaging,* Nov 14 2017.

[25] A. J. Pappano and W. G. Wier, *Cardiovascular Physiology*, 11th ed. Philadelphia: Elsevier, 2019.

[26] J. R. Levick, *An Introduction to Cardiovascular Physiology*, 5th ed. London: Hodder Arnold, 2010.

[27] M. Ragosta, *Textbook of Clinical Hemodynamics*, 2nd ed. Philadelphia, PA: Elsevier, Inc., 2018.

[28] W. W. Nichols, M. F. O'Rourke, and C. Vlachopoulos, *McDonald's blood flow in arteries: theoretical, experimental and clinical principles*, 6th ed. London: CRC Press, 2011.

[29] K. Sagawa, R. K. Lie, and J. Schaefer, "Translation of Otto Frank's paper "Die Grundform des Arteriellen Pulses" Zeitschrift fur Biologie 37: 483-526 (1899)," *J Mol Cell Cardiol,* vol. 22, no. 3, pp. 253-4, Mar 1990.

[30] N. Westerhof, J. W. Lankhaar, and B. E. Westerhof, "The arterial Windkessel," *Med Biol Eng Comput,* vol. 47, no. 2, pp. 131-41, Feb 2009.

[31] J. A. Chirinos, "Large Artery Stiffness, Microvascular Function, and Cardiovascular Risk," *Circ Cardiovasc Imaging,* vol. 9, no. 12, Dec 2016.

[32] T. R. Everett, A. A. Mahendru, C. M. McEniery, I. B. Wilkinson, and C. C. Lees, "Raised uterine artery impedance is associated with increased maternal arterial stiffness in the late second trimester," *Placenta,* vol. 33, no. 7, pp. 572-7, Jul 2012.

[33] C. Kaihura, M. D. Savvidou, J. M. Anderson, C. M. McEniery, and K. H. Nicolaides, "Maternal arterial stiffness in pregnancies affected by preeclampsia," *Am J Physiol Heart Circ Physiol,* vol. 297, no. 2, pp. H759-64, Aug 2009.

[34] M. D. Savvidou, C. Kaihura, J. M. Anderson, and K. H. Nicolaides, "Maternal arterial stiffness in women who subsequently develop pre-eclampsia," *PLoS One,* vol. 6, no. 5, p. e18703, May 3 2011.

[35] P. Dyverfeldt, T. Ebbers, and T. Lanne, "Pulse wave velocity with 4D flow MRI: systematic differences and age-related regional vascular stiffness," *Magn Reson Imaging,* vol. 32, no. 10, pp. 1266-71, Dec 2014.

[36] E. S. H. Ibrahim, K. R. Johnson, A. B. Miller, J. M. Shaffer, and R. D. White, "Measuring aortic pulse wave velocity using high-field cardiovascular magnetic resonance: comparison of techniques," (in English), *Journal of Cardiovascular Magnetic Resonance,* vol. 12, May 11 2010.

[37] M. C. Langham, C. Li, and F. W. Wehrli, "Non-triggered quantification of central and peripheral pulse-wave velocity," (in English), *Journal of Cardiovascular Magnetic Resonance,* vol. 13, Dec 21 2011.

[38] S. H. Moon *et al.*, "Increased pulse wave velocity and augmentation index after isometric handgrip exercise in patients with coronary artery disease," *Clin Hypertens,* vol. 21, p. 5, 2015.

[39] G. Styczynski *et al.*, "Echocardiographic Assessment of Aortic Pulse-Wave Velocity: Validation against Invasive Pressure Measurements," *J Am Soc Echocardiogr,* vol. 29, no. 11, pp. 1109-1116, Nov 2016.

[40] E. R. Gozna, A. E. Marble, A. Shaw, and J. G. Holland, "Age-related changes in the mechanics of the aorta and pulmonary artery of man," *J Appl Physiol,* vol. 36, no. 4, pp. 407-11, Apr 1974.

[41] R. Fähræus and T. Lindqvist, "The viscosity of the blood in narrow capillary tubes," *American Journal of Physiology,* vol. 96, pp. 562-568, 1931.

[42] M. B. Landon *et al.*, *Gabbe's Obstetrics: Normal and Problem Pregnancies*, 8th ed. Philadelphia, PA: Elsevier, 2021.

[43] R. Resnik, C. Lockwood, T. R. Moore, M. F. Greene, J. A. Copel, and R. M. Silver, *Creasy and Resnik's Maternal-Fetal Medicine: Principles and Practice*, 8th ed. Philadelphia: Elsevier, Inc., 2019.

[44] S. C. Robson, S. Hunter, R. J. Boys, and W. Dunlop, "Serial study of factors influencing changes in cardiac output during human pregnancy," *Am J Physiol,* vol. 256, no. 4 Pt 2, pp. H1060-5, Apr 1989.

[45] M. Nanna and K. Stergiopoulos, "Pregnancy complicated by valvular heart disease: an update," *J Am Heart Assoc,* vol. 3, no. 3, p. e000712, Jun 5 2014.

[46] G. Osol and L. G. Moore, "Maternal uterine vascular remodeling during pregnancy," *Microcirculation,* vol. 21, no. 1, pp. 38-47, Jan 2014.

[47] S. Chandra, A. K. Tripathi, S. Mishra, M. Amzarul, and A. K. Vaish, "Physiological changes in hematological parameters during pregnancy," *Indian J Hematol Blood Transfus,* vol. 28, no. 3, pp. 144-6, Sep 2012.

[48] A. Huisman *et al.*, "Whole blood viscosity during normal pregnancy," *Br J Obstet Gynaecol,* vol. 94, no. 12, pp. 1143-9, Dec 1987.

[49] F. Burbank, "Hemodynamic Changes in the Uterus and its Blood Vessels in Pregnancy," in *A Comprehensive Textbook of Postpartum Hemorrhage: An Essential Clinical Reference for Effective Management*, S. Arulkumara, M. Karoshi, L. G. Keith, A. B. Lalonde, and C. B-Lynch, Eds. 2nd ed. London, UK: Sapiens Publishing, 2012, pp. 177-184.

[50] Y. Wang and S. Zhao, *Vascular Biology of the Placenta* (Vascular Biology of the Placenta). San Rafael (CA), 2010.

[51] R. A. Lobo, D. A. Gershenson, G. M. Lentz, and F. A. Valea, *Comprehensive Gynecology*, 7th ed. Philadelphia: Elsevier, Inc., 2017.

[52] G. J. Burton, A. L. Watson, J. Hempstock, J. N. Skepper, and E. Jauniaux, "Uterine glands provide histiotrophic nutrition for the human fetus during the first trimester of pregnancy," *J Clin Endocrinol Metab,* vol. 87, no. 6, pp. 2954-9, Jun 2002.

[53] G. J. Burton, A. W. Woods, E. Jauniaux, and J. C. Kingdom, "Rheological and physiological consequences of conversion of the maternal spiral arteries for uteroplacental blood flow during human pregnancy," (in English), *Placenta,* vol. 30, no. 6, pp. 473-82, Jun 2009.

[54] K. Benirschke, "The Placenta: Structure and Function," *NeoReviews,* vol. 5, no. 6, pp. e252-e261, 2004.

[55] S. Hauguel, J. C. Challier, L. Cedard, and G. Olive, "Metabolism of the human placenta perfused in vitro: glucose transfer and utilization, O2 consumption, lactate and ammonia production," *Pediatr Res,* vol. 17, no. 9, pp. 729-32, Sep 1983.

[56] R. Sood, J. L. Zehnder, M. L. Druzin, and P. O. Brown, "Gene expression patterns in human placenta," *Proc Natl Acad Sci U S A,* vol. 103, no. 14, pp. 5478-83, Apr 4 2006.

[57] F. Burbank, Fibroids, Menstruation, Childbirth, and Evolution: The Fascinating Story of Uterine Blood Vessels. Tuscon, AZ: Wheatmark, 2009.

[58] L. S. Cox and C. Redman, "The role of cellular senescence in ageing of the placenta," *Placenta,* vol. 52, pp. 139-145, Apr 2017.

[59] A. Chait, A. Moltz, and J. H. Nelson, Jr., "The collateral arterial circulation in the pelvis. An angiographic study," *Am J Roentgenol Radium Ther Nucl Med,* vol. 102, no. 2, pp. 392-400, Feb 1968.

[60] G. Osol and M. Mandala, "Maternal uterine vascular remodeling during pregnancy," *Physiology (Bethesda),* vol. 24, pp. 58-71, Feb 2009.

[61] M. Walker, C. Windrim, E. Wright, and K. Levytska. (2018, Apr. 1, 2020). *Placenta Clinic*. Available: http://womensandinfantshealth.ca/fetal-medicine/placenta/

[62] G. Osol and M. Cipolla, "Pregnancy-induced changes in the three-dimensional mechanical properties of pressurized rat uteroplacental (radial) arteries," *Am J Obstet Gynecol,* vol. 168, no. 1 Pt 1, pp. 268-74, Jan 1993.

[63] J. C. Konje, P. Kaufmann, S. C. Bell, and D. J. Taylor, "A longitudinal study of quantitative uterine blood flow with the use of color power angiography in appropriate for gestational age pregnancies," *Am J Obstet Gynecol,* vol. 185, no. 3, pp. 608-13, Sep 2001.

[64] F. P. Hadlock, R. B. Harrist, and J. Martinez-Poyer, "In utero analysis of fetal growth: a sonographic weight standard," *Radiology,* vol. 181, no. 1, pp. 129-33, Oct 1991.

[65] D. M. Eckman *et al.*, "Pregnancy increases myometrial artery myogenic tone via NOS- or COX-independent mechanisms," *Am J Physiol Regul Integr Comp Physiol,* vol. 303, no. 4, pp. R368-75, Aug 15 2012.

[66] P. Y. Robillard, G. Dekker, G. Chaouat, M. Scioscia, S. Iacobelli, and T. C. Hulsey, "Historical evolution of ideas on eclampsia/preeclampsia: A proposed optimistic view of preeclampsia," *J Reprod Immunol,* vol. 123, pp. 72-77, Sep 2017.

[67] M. J. Bell, "A historical overview of preeclampsia-eclampsia," *J Obstet Gynecol Neonatal Nurs,* vol. 39, no. 5, pp. 510-8, Sep-Oct 2010.

[68] J. A. Pritchard and P. C. MacDonald, *William's Obstetrics*. New York: Appleton-Century-Crofts, 1976.

[69] C. W. Redman and I. L. Sargent, "The pathogenesis of pre-eclampsia," *Gynecol Obstet Fertil,* vol. 29, no. 7-8, pp. 518-22, Jul-Aug 2001.

[70] J. M. Roberts, R. N. Taylor, T. J. Musci, G. M. Rodgers, C. A. Hubel, and M. K. McLaughlin, "Preeclampsia: an endothelial cell disorder," *Am J Obstet Gynecol,* vol. 161, no. 5, pp. 1200-4, Nov 1989.

[71] G. D. Ernst *et al.*, "C-reactive protein levels in early pregnancy, fetal growth patterns, and the risk for neonatal complications: the Generation R Study," *Am J Obstet Gynecol,* vol. 205, no. 2, pp. 132 e1-12, Aug 2011.

[72] E. Kalafat and B. Thilaganathan, "Cardiovascular origins of preeclampsia," *Curr Opin Obstet Gynecol,* vol. 29, no. 6, pp. 383-389, Sep 28 2017.

[73] B. Thilaganathan and E. Kalafat, "Cardiovascular System in Preeclampsia and Beyond," *Hypertension,* vol. 73, no. 3, pp. 522-531, Mar 2019.

[74] M. Kovo, L. Schreiber, A. Ben-Haroush, E. Gold, A. Golan, and J. Bar, "The placental component in early-onset and late-onset preeclampsia in relation to fetal growth restriction," *Prenat Diagn,* vol. 32, no. 7, pp. 632-7, Jul 2012.

[75] W. Mifsud and N. J. Sebire, "Placental pathology in early-onset and late-onset fetal growth restriction," *Fetal Diagn Ther,* vol. 36, no. 2, pp. 117-28, 2014.

[76] T. H. Hung, T. T. Hsieh, and S. F. Chen, "Risk of abnormal fetal growth in women with early- and late-onset preeclampsia," *Pregnancy Hypertens,* vol. 12, pp. 201-206, Apr 2018.

[77] S. Rasmussen, L. M. Irgens, and J. Espinoza, "Maternal obesity and excess of fetal growth in pre-eclampsia," *BJOG,* vol. 121, no. 11, pp. 1351-7, Oct 2014.

[78] "ACOG Practice Bulletin No. 202: Gestational Hypertension and Preeclampsia," *Obstet Gynecol,* vol. 133, no. 1, pp. e1-e25, 2019.

[79] P. J. Williams and F. Broughton Pipkin, "The genetics of pre-eclampsia and other hypertensive disorders of pregnancy," *Best Pract Res Clin Obstet Gynaecol,* vol. 25, no. 4, pp. 405-17, Aug 2011.

[80] (2019, September 17, 2019). *Signs & Symptoms: Preeclampsia Foundation*. Available: https://www.preeclampsia.org/health-information/sign-symptoms

[81] M. L. LeFevre and U. S. P. S. T. Force, "Low-dose aspirin use for the prevention of morbidity and mortality from preeclampsia: U.S. Preventive Services Task Force recommendation statement," *Ann Intern Med,* vol. 161, no. 11, pp. 819-26, Dec 2 2014.

[82] N. R. Blue *et al.*, "Effect of ibuprofen vs acetaminophen on postpartum hypertension in preeclampsia with severe features: a double-masked, randomized controlled trial," *Am J Obstet Gynecol,* vol. 218, no. 6, pp. 616 e1-616 e8, Jun 2018.

[83] O. A. Viteri *et al.*, "Association of Nonsteroidal Antiinflammatory Drugs and Postpartum Hypertension in Women With Preeclampsia With Severe Features," *Obstet Gynecol,* vol. 130, no. 4, pp. 830-835, Oct 2017.

[84] S. M. Grandi *et al.*, "Hypertensive Disorders in Pregnancy and the Risk of Subsequent Cardiovascular Disease," *Paediatr Perinat Epidemiol,* vol. 31, no. 5, pp. 412-421, Sep 2017.

[85] X. Xiong, N. N. Demianczuk, L. D. Saunders, F. L. Wang, and W. D. Fraser, "Impact of preeclampsia and gestational hypertension on birth weight by gestational age," *Am J Epidemiol,* vol. 155, no. 3, pp. 203-9, Feb 1 2002.

[86] E. F. Davis *et al.*, "Cardiovascular risk factors in children and young adults born to preeclamptic pregnancies: a systematic review," *Pediatrics,* vol. 129, no. 6, pp. e1552-61, Jun 2012.

[87] V. S. Jammalamadaga and P. Abraham, "Spectrum of Factors Triggering Endothelial Dysfunction in PIH," *J Clin Diagn Res,* vol. 10, no. 12, pp. BC14-BC17, Dec 2016.

[88] S. C. Cushen and S. Goulopoulou, "New Models of Pregnancy-Associated Hypertension," *Am J Hypertens,* vol. 30, no. 11, pp. 1053-1062, Nov 1 2017.

[89] E. A. Phipps, R. Thadhani, T. Benzing, and S. A. Karumanchi, "Pre-eclampsia: pathogenesis, novel diagnostics and therapies," *Nat Rev Nephrol,* vol. 15, no. 5, pp. 275-289, May 2019.

[90] E. M. George, "New approaches for managing preeclampsia: clues from clinical and basic research," *Clin Ther,* vol. 36, no. 12, pp. 1873-1881, Dec 1 2014.

[91] J. S. Pellerito and J. F. Polak, *Introoduction to Vascular Ultrasonography*, 7th ed. Philadelphia: Elsevier, 2020.

[92] K. Nicolaides, G. Rizzo, K. Hecher, and R. Ximenes, Doppler in Obstetrics: Fetal Medicine, 2002. [Online]. Available: https://fetalmedicine.org/var/uploads/Doppler-in-Obstetrics.pdf.

[93] S. Bly and M. C. Van Den Hof, "Obstetric Ultrasound Biological Effects and Safety," *SOGC Clinical Practice Guidelines,* vol. 160, pp. 572-575, 2005.

[94] "AIUM Practice Parameter for the Performance of Limited Obstetric Ultrasound Examinations by Advanced Clinical Providers," *J Ultrasound Med,* vol. 37, pp. 1587-1596, 2018.

[95] R. S. Moorthy, "Transvaginal Sonography," *Med J Armed Forces India,* vol. 56, no. 3, pp. 181-183, Jul 2000.

[96] A. Bhide *et al.*, "ISUOG practice guidelines: use of Doppler ultrasonography in obstetrics," *Ultrasound Obstet Gynecol,* vol. 41, no. 2, pp. 233-39, Feb 2013.

[97] P. A. Iaizzo, Ed. *Handbook of Cardiac Anatomy, Physiology, and Devices*, Third ed. Switzerland: Springer International Publishing, 2015.

[98] P. Gupta, S. Lyons, and S. Hedgre, "Ultrasound imaging of the arterial system," *Cardiovasc Diagn Ther,* vol. 9, no. Suppl 1, pp. S2-S13, 2019.

[99] J. D. Fraser and D. R. Anderson, "Venous protocols, techniques, and interpretations of the upper and lower extremities," *Radiol Clin North Am,* vol. 42, no. 2, pp. 279-96, Mar 2004.

[100] C. J. Marrocco *et al.*, "Intravascular Ultrasound," *Semin Vasc Surg,* vol. 25, pp. 144-152, 2012.

[101] S. Sonoda, K. Hibi, H. Okura, K. Fujii, Y. Honda, and Y. Kobayashi, "Current clinical use of intravascular ultrasound imaging to guide percutaneous coronary interventions," *Cardiovasc Interv Ther,* vol. 35, no. 1, pp. 30-36, Jan 2020.

[102] E. Wali and S. Nathan, "What Is the Clinical Utility of Intravascular Ultrasound?," *Curr Cardiol Rep,* vol. 20, no. 11, p. 122, Sep 28 2018.

[103] B. S. Hertzberg and W. D. Middleton, *Ultrasound: The Requisites*, 3rd. ed. Philadelphia: Elsevier, 2016.

[104] A. M. Kennedy and P. J. Woodward, "A Radiologist's Guide to the Performance and Interpretation of Obstetric Doppler US," *Radiographics,* vol. 39, no. 3, pp. 893-910, May-Jun 2019.

[105] F. P. Hadlock, R. B. Harrist, R. S. Sharman, R. L. Deter, and S. K. Park, "Estimation of fetal weight with the use of head, body, and femur measurements--a prospective study," *Am J Obstet Gynecol,* vol. 151, no. 3, pp. 333-7, Feb 01 1985.

[106] S. G. Kim, "Quantification of relative cerebral blood flow change by flow-sensitive alternating inversion recovery (FAIR) technique: application to functional mapping," *Magn Reson Med,* vol. 34, no. 3, pp. 293-301, Sep 1995.

[107] R. B. Buxton, L. R. Frank, E. C. Wong, B. Siewert, S. Warach, and R. R. Edelman, "A general kinetic model for quantitative perfusion imaging with arterial spin labeling," *Magn Reson Med,* vol. 40, no. 3, pp. 383-96, Sep 1998.

[108] M. A. Bernstein, *Handbook of MRI Pulse Sequences*. New York: Elsevier Academic Press, 2004, p. 1041.

[109] E. M. Haacke, R. W. Brown, M. R. Thompson, and R. Venkatesan, *Magnetic Resonance Imaging: Physical Principles and Sequence Design*. New York: John Wiley & Sons, Inc., 1999, p. 914.

[110] M. A. Bernstein, A. Shimakawa, and N. J. Pelc, "Minimizing TE in moment-nulled or flow-encoded two- and three-dimensional gradient-echo imaging," *J Magn Reson Imaging,* vol. 2, no. 5, pp. 583-8, Sep-Oct 1992.

[111] J. A. Detre, H. Rao, D. J. Wang, Y. F. Chen, and Z. Wang, "Applications of arterial spin labeled MRI in the brain," *J Magn Reson Imaging,* vol. 35, no. 5, pp. 1026-37, May 2012.

[112] J. A. Chalela, D. C. Alsop, J. B. Gonzalez-Atavales, J. A. Maldjian, S. E. Kasner, and J. A. Detre, "Magnetic resonance perfusion imaging in acute ischemic stroke using continuous arterial spin labeling," *Stroke,* vol. 31, no. 3, pp. 680-7, Mar 2000.

[113] R. L. Wolf *et al.*, "Grading of CNS neoplasms using continuous arterial spin labeled perfusion MR imaging at 3 Tesla," *J Magn Reson Imaging,* vol. 22, no. 4, pp. 475-82, Oct 2005.

[114] D. C. Alsop, J. A. Detre, and M. Grossman, "Assessment of cerebral blood flow in Alzheimer's disease by spin-labeled magnetic resonance imaging," *Ann Neurol,* vol. 47, no. 1, pp. 93-100, Jan 2000.

[115] I. R. Olson, H. Rao, K. S. Moore, J. Wang, J. A. Detre, and G. K. Aguirre, "Using perfusion fMRI to measure continuous changes in neural activity with learning," *Brain Cogn,* vol. 60, no. 3, pp. 262-71, Apr 2006.

[116] J. Wang *et al.*, "Perfusion functional MRI reveals cerebral blood flow pattern under psychological stress," *Proc Natl Acad Sci U S A,* vol. 102, no. 49, pp. 17804-9, Dec 6 2005.

[117] J. Lotz, C. Meier, A. Leppert, and M. Galanski, "Cardiovascular flow measurement with phase-contrast MR imaging: basic facts and implementation," *Radiographics,* vol. 22, no. 3, pp. 651-71, May-Jun 2002.

[118] G. Masselli, "MRI of Fetal and Maternal Diseases in Pregnancy." Switzerland: Springer International Publishing, 2016, p.^pp. Pages.

[119] I. Derwig *et al.*, "Association of placental perfusion, as assessed by magnetic resonance imaging and uterine artery Doppler ultrasound, and its relationship to pregnancy outcome," *Placenta,* vol. 34, no. 10, pp. 885-91, Oct 2013.

[120] R. Avni, M. Neeman, and J. R. Garbow, "Functional MRI of the placenta--From rodents to humans," *Placenta,* vol. 36, no. 6, pp. 615-22, Jun 2015.

[121] R. Avni, T. Raz, I. E. Biton, V. Kalchenko, J. R. Garbow, and M. Neeman, "Unique in utero identification of fetuses in multifetal mouse pregnancies by placental bidirectional arterial spin labeling MRI," *Magn Reson Med,* vol. 68, no. 2, pp. 560-70, Aug 2012.

[122] K. D. Ludwig *et al.*, "Perfusion MRI of the Placenta: Preliminary Results using ASL FAIR and Ferumoxytol DCE MRI in the Rhesus Macaque," in *Proc. Intl. Soc. Mag. Reson. Med. 25th Annual Meeting*, Honolulu, HI, 2017.

[123] J. Hutter *et al.*, "Perfusion and apparent oxygenation in the human placenta (PERFOX)," *Magn Reson Med,* vol. 83, no. 2, pp. 549-560, Feb 2020.

[124] D. Sussman *et al.*, "Uterine artery and umbilical vein blood flow are unaffected by moderate habitual physical activity during pregnancy," *Prenat Diagn,* vol. 39, no. 11, pp. 976-985, Oct 2019.

[125] J. A. Macdonald *et al.*, "Uteroplacental and Fetal 4D Flow MRI in the Pregnant Rhesus Macaque," *J Magn Reson Imaging,* vol. 49, no. 2, pp. 534-545, Feb 2019.

[126] J. G. Ray, M. J. Vermeulen, A. Bharatha, W. J. Montanera, and A. L. Park, "Association Between MRI Exposure During Pregnancy and Fetal and Childhood Outcomes," (in English), *Jama-Journal of the American Medical Association,* vol. 316, no. 9, pp. 952-961, Sep 6 2016.

[127] J. T. Little and C. A. Bookwalter, "Magnetic Resonance Safety: Pregnancy and Lactation," *Magn Reson Imaging Clin N Am,* vol. 28, no. 4, pp. 509-516, Nov 2020.

[128] R. W. Redline, "Classification of placental lesions," *Am J Obstet Gynecol,* vol. 213, no. 4 Suppl, pp. S21-8, Oct 2015.

[129] C. J. Roth *et al.*, "Dynamic modeling of uteroplacental blood flow in IUGR indicates vortices and elevated pressure in the intervillous space - a pilot study," (in English), *Scientific Reports,* Article vol. 7, p. 11, Jan 2017, Art. no. 40771.

[130] K. L. Deurloo, M. D. Spreeuwenberg, A. C. Bolte, and J. M. Van Vugt, "Color Doppler ultrasound of spiral artery blood flow for prediction of hypertensive disorders and intra uterine growth restriction: a longitudinal study," *Prenat Diagn,* vol. 27, no. 11, pp. 1011-6, Nov 2007.

[131] R. Bhoil *et al.*, "Color Doppler ultrasound of spiral artery blood flow in mid first trimester (4-8 weeks) in cases of threatened abortion and in normal pregnancies," *J Ultrason,* vol. 19, no. 79, pp. 255-260, Dec 2019.

[132] P. Gowland, "Placental MRI," *Semin Fetal Neonatal Med,* vol. 10, no. 5, pp. 485-90, Oct 2005.

[133] E. Hwuang *et al.*, "Background-suppressed pulsed arterial spin labeling of placental perfusion at 1.5T," in *Proc. Int. Soc. of Mag. Res. Med. 26th Annual Meeting*, Paris, France, 2018.

[134] E. Hwuang, N. Schwartz, W. R. Witschey, J. A. Detre, and D. Tisdall, "Pattern Analysis of Placental Blood Flow Distribution using ASL MRI," in *Proc. Int. Soc. of Mag. Res. Med. 27th Annual Meeting*, Montreal, Canada, 2019.

[135] B. B. Avants, N. J. Tustison, G. Song, P. A. Cook, A. Klein, and J. C. Gee, "A reproducible evaluation of ANTs similarity metric performance in brain image registration," *Neuroimage,* vol. 54, no. 3, pp. 2033-44, Feb 1 2011.

[136] X. Zhang *et al.*, "In vivo blood T(1) measurements at 1.5 T, 3 T, and 7 T," *Magn Reson Med,* vol. 70, no. 4, pp. 1082-6, Oct 2013.

[137] B. J. Trudinger, W. B. Giles, and C. M. Cook, "Flow velocity waveforms in the maternal uteroplacental and fetal umbilical placental circulations," *Am J Obstet Gynecol,* vol. 152, no. 2, pp. 155-63, May 15 1985.

[138] H. Schulman, "The clinical implications of Doppler ultrasound analysis of the uterine and umbilical arteries," *Am J Obstet Gynecol,* vol. 156, no. 4, pp. 889-93, Apr 1987.

[139] T. R. Everett and C. C. Lees, "Beyond the placental bed: placental and systemic determinants of the uterine artery Doppler waveform," *Placenta,* vol. 33, no. 11, pp. 893-901, Nov 2012.

[140] O. Gomez *et al.*, "Reference ranges for uterine artery mean pulsatility index at 11-41 weeks of gestation," (in English), *Ultrasound Obstet Gynecol,* vol. 32, no. 2, pp. 128-132, Aug 2008.

[141] A. Weichert, A. Hagen, M. Tchirikov, I. B. Fuchs, W. Henrich, and M. Entezami, "Reference Curve for the Mean Uterine Artery Pulsatility Index in Singleton Pregnancies," *Geburtshilfe Frauenheilkd,* vol. 77, no. 5, pp. 516-523, May 2017.

[142] A. McKelvey, K. Pateman, I. Balchin, D. M. Peebles, C. H. Rodeck, and A. L. David, "Total uterine artery blood volume flow rate in nulliparous women is associated with birth weight and gestational age at delivery," *Ultrasound Obstet Gynecol,* vol. 49, no. 1, pp. 54-60, Jan 2017.

[143] M. Markl, P. J. Kilner, and T. Ebbers, "Comprehensive 4D velocity mapping of the heart and great vessels by cardiovascular magnetic resonance," *J Cardiovasc Magn Reson,* vol. 13, p. 7, Jan 14 2011.

[144] P. Dyverfeldt *et al.*, "4D flow cardiovascular magnetic resonance consensus statement," *J Cardiovasc Magn Reson,* vol. 17, p. 72, Aug 10 2015.

[145] B. Jung, P. Ullmann, M. Honal, S. Bauer, J. Hennig, and M. Markl, "Parallel MRI with extended and averaged GRAPPA kernels (PEAK-GRAPPA): optimized spatiotemporal dynamic imaging," *J Magn Reson Imaging,* vol. 28, no. 5, pp. 1226-32, Nov 2008.

[146] M. A. Bernstein *et al.*, "Concomitant gradient terms in phase contrast MR: analysis and correction," *Magn Reson Med,* vol. 39, no. 2, pp. 300-8, Feb 1998.

[147] A. F. Stalder, M. F. Russe, A. Frydrychowicz, J. Bock, J. Hennig, and M. Markl, "Quantitative 2D and 3D phase contrast MRI: optimized analysis of blood flow and vessel wall parameters," *Magn Reson Med,* vol. 60, no. 5, pp. 1218-31, Nov 2008.

[148] J. Bock, B. W. Kreher, J. Hennig, and M. Markl, "Optimized pre-processing of time-resolved 2D and 3D Phase Contrast MRI data," in *Proc. Intl. Soc. Mag. Reson. Med. 15*, Berlin, Germany, 2007.

[149] J. Bock *et al.*, "4D phase contrast MRI at 3 T: effect of standard and blood-pool contrast agents on SNR, PC-MRA, and blood flow visualization," *Magn Reson Med,* vol. 63, no. 2, pp. 330-8, Feb 2010.

[150] E. Hwuang *et al.*, "Assessment of uterine artery geometry and hemodynamics in human pregnancy with 4d flow mri and its correlation with doppler ultrasound," *J Magn Reson Imaging,* vol. 49, no. 1, pp. 59-68, Nov 3 2018.

[151] H. Y. Kim, "Statistical notes for clinical researchers: Evaluation of measurement error 2: Dahlberg's error, Bland-Altman method, and Kappa coefficient," *Restor Dent Endod,* vol. 38, no. 3, pp. 182-5, Aug 2013.

[152] Y. Wang and X. Huang, "Sepsis after uterine artery embolization-assisted termination of pregnancy with complete placenta previa: A case report," *J Int Med Res,* p. 300060517723257, Jan 01 2017.

[153] Z. O. Amarin, P. Z. Amarin, Ed. *Approaches to Hysterectomy*. InTech, 2015.

[154] J. A. Pates, M. R. Hatab, D. D. McIntire, F. G. Cunningham, and D. M. Twickler, "Determining uterine blood flow in pregnancy with magnetic resonance imaging," *Magn Reson Imaging,* vol. 28, no. 4, pp. 507-10, May 2010.

[155] S. K. Palmer, S. Zamudio, C. Coffin, S. Parker, E. Stamm, and L. G. Moore, "Quantitative estimation of human uterine artery blood flow and pelvic blood flow redistribution in pregnancy," *Obstet Gynecol,* vol. 80, no. 6, pp. 1000-6, Dec 1992.

[156] D. Kienzl *et al.*, "Risk of inferior vena cava compression syndrome during fetal MRI in the supine position - a retrospective analysis," *J Perinat Med,* vol. 42, no. 3, pp. 301-6, May 2014.

[157] S. Rigano, E. Ferrazzi, S. Boito, G. Pennati, A. Padoan, and H. Galan, "Blood flow volume of uterine arteries in human pregnancies determined using 3D and bi-dimensional imaging, angio-Doppler, and fluid-dynamic modeling," *Placenta,* vol. 31, no. 1, pp. 37-43, Jan 2010.

[158] J. Bock *et al.*, "In vivo noninvasive 4D pressure difference mapping in the human aorta: phantom comparison and application in healthy volunteers and patients," *Magn Reson Med,* vol. 66, no. 4, pp. 1079-88, Oct 2011.

[159] A. Kolipaka *et al.*, "Quantification and comparison of 4D-flow MRI-derived wall shear stress and MRE-derived wall stiffness of the abdominal aorta," *J Magn Reson Imaging,* vol. 45, no. 3, pp. 771-778, Mar 2017.

[160] S. H. Nelson, O. S. Steinsland, Y. Wang, C. Yallampalli, Y. L. Dong, and J. M. Sanchez, "Increased nitric oxide synthase activity and expression in the human uterine artery during pregnancy," *Circ Res,* vol. 87, no. 5, pp. 406-11, Sep 01 2000.

[161] J. Copel, Y. El-Sayed, R. P. Heine, K. R. Wharton, A. C. O. Gyneco, and C. O. Practice, "Guidelines for Diagnostic Imaging During Pregnancy and Lactation," (in English), *Obstetrics and Gynecology,* vol. 130, no. 4, pp. E210-E216, Oct 2017.

[162] Y. Patenaude *et al.*, "The use of magnetic resonance imaging in the obstetric patient," *J Obstet Gynaecol Can,* vol. 36, no. 4, pp. 349-63, Apr 2014.

[163] M. R. S. Expert Panel on *et al.*, "ACR guidance document on MR safe practices: 2013," *J Magn Reson Imaging,* vol. 37, no. 3, pp. 501-30, Mar 2013.

[164] D. Bulas and A. Egloff, "Benefits and risks of MRI in pregnancy," *Semin Perinatol,* vol. 37, no. 5, pp. 301-4, Oct 2013.

[165] T. A. Jaffe, C. M. Miller, and E. M. Merkle, "Practice patterns in imaging of the pregnant patient with abdominal pain: a survey of academic centers," *AJR Am J Roentgenol,* vol. 189, no. 5, pp. 1128-34, Nov 2007.

[166] M. A. Razik, M. A. H. Farag, and M. Sheta, "Uterine and ovarian arteries blood flow during the mid luteal phase in women with unexplained infertility," (in English), *Middle East Fertility Society Journal,* vol. 20, no. 3, pp. 209-212, Sep 2015.

[167] L. W. Chien, W. S. Lee, H. K. Au, and C. R. Tzeng, "Assessment of changes in utero-ovarian arterial impedance during the peri-implantation period by Doppler sonography in women undergoing assisted reproduction," (in English), *Ultrasound in Obstetrics & Gynecology,* vol. 23, no. 5, pp. 496-500, May 2004.

[168] A. T. Papageorghiou, C. K. Yu, and K. H. Nicolaides, "The role of uterine artery Doppler in predicting adverse pregnancy outcome," *Best Pract Res Clin Obstet Gynaecol,* vol. 18, no. 3, pp. 383-96, Jun 2004.

[169] D. M. Gallo, D. Wright, C. Casanova, M. Campanero, and K. H. Nicolaides, "Competing risks model in screening for preeclampsia by maternal factors and biomarkers at 19-24 weeks' gestation," *Am J Obstet Gynecol,* vol. 214, no. 5, pp. 619 e1-619 e17, May 2016.

[170] J. Tay *et al.*, "Uterine and fetal placental Doppler indices are associated with maternal cardiovascular function," *Am J Obstet Gynecol,* vol. 220, no. 1, pp. 96 e1-96 e8, Jan 2019.

[171] J. P. Schaaps *et al.*, "Shunting the intervillous space: new concepts in human uteroplacental vascularization," *Am J Obstet Gynecol,* vol. 192, no. 1, pp. 323-32, Jan 2005.

[172] A. R. Clark, J. L. James, G. N. Stevenson, and S. L. Collins, "Understanding abnormal uterine artery Doppler waveforms: A novel computational model to explore potential causes within the utero-placental vasculature," *Placenta,* vol. 66, pp. 74-81, Jun 2018.

[173] M. Markl *et al.*, "Advanced flow MRI: emerging techniques and applications," *Clin Radiol,* vol. 71, no. 8, pp. 779-95, Aug 2016.

[174] J. Sotelo *et al.*, "3D axial and circumferential wall shear stress from 4D flow MRI data using a finite element method and a laplacian approach," *Magn Reson Med,* Oct 04 2017.

[175] J. F. Rodriguez-Palomares *et al.*, "Aortic flow patterns and wall shear stress maps by 4D-flow cardiovascular magnetic resonance in the assessment of aortic dilatation in bicuspid aortic valve disease," *J Cardiovasc Magn Reson,* vol. 20, no. 1, p. 28, Apr 26 2018.

[176] G. Reiter *et al.*, "Magnetic resonance-derived 3-dimensional blood flow patterns in the main pulmonary artery as a marker of pulmonary hypertension and a measure of elevated mean pulmonary arterial pressure," *Circ Cardiovasc Imaging,* vol. 1, no. 1, pp. 23-30, Jul 2008.

[177] T. R. Fenton, R. Nasser, M. Eliasziw, J. H. Kim, D. Bilan, and R. Sauve, "Validating the weight gain of preterm infants between the reference growth curve of the fetus and the term infant," *BMC Pediatr,* vol. 13, p. 92, Jun 11 2013.

[178] A. T. Papageorghiou, C. K. H. Yu, R. Bindra, G. Pandis, K. H. Nicolaides, and F. M. Fdn, "Multicenter screening for pre-eclampsia and fetal growth restriction by transvaginal uterine artery Doppler at 23 weeks of gestation," (in English), *Ultrasound Obstet Gynecol,* vol. 18, no. 5, pp. 441-449, Nov 2001.

[179] A. Familiari, A. Bhide, M. Morlando, C. Scala, A. Khalil, and B. Thilaganathan, "Mid-pregnancy fetal biometry, uterine artery Doppler indices and maternal demographic characteristics: role in prediction of small-for-gestational-age birth," *Acta Obstet Gynecol Scand,* vol. 95, no. 2, pp. 238-44, Feb 2016.

[180] L. C. Poon, C. Lesmes, D. M. Gallo, R. Akolekar, and K. H. Nicolaides, "Prediction of small-for-gestational-age neonates: screening by biophysical and biochemical markers at 19-24 weeks," *Ultrasound Obstet Gynecol,* vol. 46, no. 4, pp. 437-45, Oct 2015.

[181] H. Liang, A. Vartun, K. Flo, C. Widnes, and G. Acharya, "Maternal cardiac function, uterine artery hemodynamics and natriuretic peptides at 22-24 weeks of gestation and subsequent development of hypertensive disorders of pregnancy," *Acta Obstet Gynecol Scand,* vol. 98, no. 4, pp. 507-514, Apr 2019.

[182] V. A. Browne *et al.*, "High-end arteriolar resistance limits uterine artery blood flow and restricts fetal growth in preeclampsia and gestational hypertension at high altitude," *Am J Physiol Regul Integr Comp Physiol,* vol. 300, no. 5, pp. R1221-9, May 2011.

[183] S. A. Hale, A. Schonberg, G. J. Badger, and I. M. Bernstein, "Relationship between prepregnancy and early pregnancy uterine blood flow and resistance index," *Reprod Sci,* vol. 16, no. 11, pp. 1091-6, Nov 2009.

[184] K. Harrington, R. G. Carpenter, C. Goldfrad, and S. Campbell, "Transvaginal Doppler ultrasound of the uteroplacental circulation in the early prediction of pre-eclampsia and intrauterine growth retardation," *Br J Obstet Gynaecol,* vol. 104, no. 6, pp. 674-81, Jun 1997.

[185] E. Ferrazzi, S. Rigano, A. Padoan, S. Boito, G. Pennati, and H. L. Galan, "Uterine artery blood flow volume in pregnant women with an abnormal pulsatility index of the uterine arteries delivering normal or intrauterine growth restricted newborns," *Placenta,* vol. 32, no. 7, pp. 487-92, Jul 2011.

[186] J. C. Konje, E. S. Howarth, P. Kaufmann, and D. J. Taylor, "Longitudinal quantification of uterine artery blood volume flow changes during gestation in pregnancies complicated by intrauterine growth restriction," *Br J Obstet Gynaecol,* vol. 110, no. 3, pp. 301-5, Mar 2003.

[187] R. P. Dickey and J. F. Hower, "Ultrasonographic features of uterine blood flow during the first 16 weeks of pregnancy," *Hum Reprod,* vol. 10, no. 9, pp. 2448-52, Sep 1995.

[188] S. Bower, S. Vyas, S. Campbell, and K. H. Nicolaides, "Color Doppler imaging of the uterine artery in pregnancy: normal ranges of impedance to blood flow, mean velocity and volume of flow," *Ultrasound Obstet Gynecol,* vol. 2, no. 4, pp. 261-5, Jul 1 1992.

[189] K. Flo, T. Wilsgaard, A. Vartun, and G. Acharya, "A longitudinal study of the relationship between maternal cardiac output measured by impedance cardiography and uterine artery blood flow in the second half of pregnancy," *Br J Obstet Gynaecol,* vol. 117, no. 7, pp. 837-44, Jun 2010.

[190] L. Boussel *et al.*, "Phase-contrast magnetic resonance imaging measurements in intracranial aneurysms in vivo of flow patterns, velocity fields, and wall shear stress: comparison with computational fluid dynamics," *Magn Reson Med,* vol. 61, no. 2, pp. 409-17, Feb 2009.

[191] S. Schnell, C. Wu, and S. A. Ansari, "Four-dimensional MRI flow examinations in cerebral and extracerebral vessels - ready for clinical routine?," *Curr Opin Neurol,* vol. 29, no. 4, pp. 419-28, Aug 2016.

[192] E. Adali, M. Kurdoglu, F. Adali, N. Cim, R. Yildizhan, and A. Kolusari, "The relationship between brachial artery flow-mediated dilatation, high sensitivity C-reactive protein, and uterine artery doppler velocimetry in women with pre-eclampsia," *J Clin Ultrasound,* vol. 39, no. 4, pp. 191-7, May 2011.

[193] H. Perry, H. Lehmann, E. Mantovani, B. Thilaganathan, and A. Khalil, "Correlation between central and uterine hemodynamics in hypertensive disorders of pregnancy," *Ultrasound Obstet Gynecol,* vol. 54, pp. 58-63, 2019.

[194] D. M. Folk, "Hypertensive Disorders of Pregnancy: Overview and Current Recommendations," *J Midwifery Womens Health,* May 15 2018.

[195] T. Gu *et al.*, "PC VIPR: a high-speed 3D phase-contrast method for flow quantification and high-resolution angiography," *AJNR Am J Neuroradiol,* vol. 26, no. 4, pp. 743-9, Apr 2005.

[196] A. Roldan-Alzate, C. J. Francois, O. Wieben, and S. B. Reeder, "Emerging Applications of Abdominal 4D Flow MRI," *AJR Am J Roentgenol,* vol. 207, no. 1, pp. 58-66, Jul 2016.

[197] J. Carson, L. Warrander, E. Johnstone, and R. van Loon, "Personalising cardiovascular network models in pregnancy: A two-tiered parameter estimation approach," *Int J Numer Method Biomed Eng,* p. e3267, Dec 4 2019.

[198] S. S. Ong, P. N. Baker, T. M. Mayhew, and W. R. Dunn, "Remodeling of myometrial radial arteries in preeclampsia," *Am J Obstet Gynecol,* vol. 192, no. 2, pp. 572-9, Feb 2005.

[199] E. Hwuang, M. Vidorreta, N. Schwartz, J. A. Detre, D. J. Licht, and W. R. Witschey, "Assessment of uterine artery hemodynamics in normal pregnancy with 4D Flow MRI," in *Proc. Intl. Soc. Mag. Reson. Med. 25*, Honolulu, HI, 2017, 2017.

[200] J. C. Konje, E. S. Howarth, P. Kaufmann, and D. J. Taylor, "Longitudinal quantification of uterine artery blood volume flow changes during gestation in pregnancies complicated by intrauterine growth restriction," *BJOG,* vol. 110, no. 3, pp. 301-5, Mar 2003.

[201] K. K. Griendling, E. O. Fuller, and R. H. Cox, "Pregnancy-induced changes in sheep uterine and carotid arteries," *Am J Physiol,* vol. 248, no. 5 Pt 2, pp. H658-65, May 1985.

[202] Y. Yinon *et al.*, "Vascular dysfunction in women with a history of preeclampsia and intrauterine growth restriction: insights into future vascular risk," *Circulation,* vol. 122, no. 18, pp. 1846-53, Nov 2 2010.

[203] O. Paez *et al.*, "Parallel decrease in arterial distensibility and in endothelium-dependent dilatation in young women with a history of pre-eclampsia," *Clin Exp Hypertens,* vol. 31, no. 7, pp. 544-52, Oct 2009.

[204] W. R. Milnor, *Hemodynamics*. Baltimore: Williams & Wilkins, 1982.

[205] H. Dyvorne *et al.*, "Abdominal 4D flow MR imaging in a breath hold: combination of spiral sampling and dynamic compressed sensing for highly accelerated acquisition," *Radiology,* vol. 275, no. 1, pp. 245-54, Apr 2015.

[206] M. Zamir, D. M. Nelson, and Y. Ginosar, "Geometric and hemodynamic characterization of uterine spiral arteries: The concept of resistance reserve," *Placenta,* vol. 68, pp. 59-64, Aug 2018.

[207] T. Ruesink, R. Medero, D. Rutkowski, and A. Roldan-Alzate, "In Vitro Validation of 4D Flow MRI for Local Pulse Wave Velocity Estimation," *Cardiovasc Eng Technol,* vol. 9, no. 4, pp. 674-687, Dec 2018.